DEVELOPMENT OF POLYPHOSPHOESTER-BASED POLYMERIC NANOPARTICLES AS DELIVERY CARRIERS FOR SILVER-BASED ANTIMICROBIAL AGENTS FOR TREATMENT OF INFECTIOUS DISEASES

A Dissertation

by

YOUNG HOON LIM

Submitted to the Office of Graduate and Professional Studies of
Texas A&M University
in partial fulfillment of the requirements for the degree of

DOCTOR OF PHILOSOPHY

Chair of Committee,	Karen L. Wooley
Committee Members,	Donald J. Darensbourg
	Marcetta Y. Darensbourg
	Zhengdong Cheng
Head of Department,	François P. Gabbaï

August 2015

Major Subject: Chemistry

ABSTRACT

The development of well-defined polymeric nanoparticles (NPs) as delivery carriers for antimicrobials targeting human infectious diseases requires rational design of the polymer template, an efficient synthetic approach and fundamental understanding of the developed NPs, *e.g.*, drug loading/release, particle stability, and other characteristics.

In order to develop potentially fully biodegradable, biocompatible polymeric NPs with the capability to deliver silver-based antimicrobials, a series of anionic degradable NPs (dNPs) were prepared from block copolymers having polyphosphoester (PPE) and poly(L-lactide) block segments, designed specifically for silver loading into the hydrophilic shell and/or the hydrophobic core. With the use of three different types of silver-based antimicrobials – silver acetate (AgOAc) or one of two silver carbene complexes (SCCs), comparative studies of the selection of proper dNP templates for silver-loading and release were undertaken. Then, the comprehensive degradation studies, including evaluation of hydrolytic or enzymatic degradability and identification of the degradation products, were performed for the fundamental understanding of the developed dNPs as potential delivery carriers for silver-based antimicrobials. Finally, *in vitro* antimicrobial efficacy of the selected Ag-dNPs was compared with that of inherent silver compounds against 10 contemporary epidemic strains of *Staphylococcus aureus* and eight uropathogenic strains of *Escherichia coli.*

Organocatalyzed ring-opening polymerization (ROP) of ethylene glycol vinyl ether-containing cyclic phosphotriester monomer, as an initial fundamental study toward

unique degradable, functional polymer materials, was described. After demonstrating the well-controlled homopolymerization of the monomer with predetermined molecular weights and narrow molecular weight distributions, the resulting vinyl ether-functionalized PPE scaffold was conjugated with hydroxyl- or thiol-containing model small molecules *via* three different types of conjugation chemistries – thiol–ene "click" reaction, acetalization, or thio–acetalization reaction – revealing efficient routes for postpolymerization modifications of functional polymers. Furthermore, amphiphilic diblock copolymers containing the ethylene glycol vinyl ether-functionalized PPE as a hydrophobic block segment, also prepared by ROP, afforded well-defined micelles that showed a pH-dependent hydrolytic core degradability of both backbone and side chains in aqueous solutions. The degradation products, as identified by mass spectrometry, were found to be nontoxic toward two standard cell lines: RAW 264.7 mouse macrophages and OVCAR-3 human ovarian adenocarcinoma cells.

DEDICATION

This work is dedicated to my God and family.

ACKNOWLEDGEMENTS

I would like to thank my advisor, Dr. Karen L. Wooley for her great support, guidance, and encouragement during my graduate study at Texas A&M University. Without her advices, this work could not have been accomplished. Her detail-oriented research attitude, passion for science and warm-heartedness as a mentor has been exemplary to me as a role-model. It was my honor to be in her group at Texas A&M University and to have her as my advisor.

Special recognition must also be given to my research committee members, Dr. Donald J. Darensbourg, Dr. Marcetta Y. Darensbourg, and Dr. Zhengdong Cheng for their inspirational suggestions and support throughout the course of this research. I also appreciate Dr. Jamie C. Grunlan for his generous attendance on my defense as a substitute committee member for Dr. Zhengdong Cheng.

I also want to extend my gratitude to my collaborators, Dr. David A. Hunstad and Ms. Kristin M. Tiemann at Washington University in St. Louis, Dr. Wiley J. Youngs and Mr. Patrick O. Wagers at University of Akron, and Dr. Carolyn L. Cannon, Mr. Justin A. Smolen and Dr. Parth N. Shah at Texas A&M University.

Thanks also go to my colleagues in the Wooley group, former and present, in no particular order: Dr. Mahmoud Elsabahy, Dr. Jeffery Raymond, Dr. Soon-Mi Lim, Mr. Alexander Lonnecker, Mr. Andy Moutray, Ms. Casey McDonald, Mr. Gyu Seong Heo, Dr. Guorong Sun, Dr. Yannick Borguet, Dr. Marco Giles, Dr. Ashlee Jahnke, Dr. Lu Su, Mr. Jingwei Fan, Ms. Simcha Felder, Ms. Jeniree Flores, Mr. Xun He, Ms. Samantha

Kristufek, Mr. Eric Leonhardt, Mr. Richen Li, Ms. Lauren Link, Ms. Adriana Pavia-Sanders, Ms. Kellie Seetho, Ms. Jennifer Summerhill, Dr. Ang Li, Mr. Timothy Tsao, Mr. Kevin Wacker, Mr. Peter Wang, Mr. Fuwu Zhang, Mr. Sangho Cho, Dr. Amandine Noel, Dr. Tiffany P. Gustafson, Dr. Jiong Zou, Dr. Koichiro Mikami, Dr. Kevin Pollack, Dr. Sandani Samarajeewa, Dr. Shiyi Zhang, Dr. Rita Shrestha, and Dr. Philip Imbesi.

I also would like to acknowledge the department faculty and staff, especially, Dr. Yohannes H. Rezenom for the kind advice in the experiment of mass-spectrometry and Dr. Hansoo Kim for the generous help in the measurement of transmission electron microscopy at Texas A&M University.

I would like to thank my family for their love, encouragement, and support in many ways.

Finally, I gratefully acknowledge financial support from the National Heart Lung and Blood Institute as a Program of Excellence in Nanotechnology and from the National Institute of Diabetes and Digestive and Kidney Diseases. The Welch Foundation is gratefully acknowledged for support through the W. T. Doherty-Welch Chair in Chemistry.

TABLE OF CONTENTS

Page

ABSTRACT ii

DEDICATION iv

ACKNOWLEDGEMENTS v

TABLE OF CONTENTS vii

LIST OF FIGURES ix

LIST OF TABLES xv

CHAPTER I INTRODUCTION AND LITERATURE REVIEW 1

1.1. Background and Motivation 1
1.2. Organocatalyzed Ring-Opening Polymerization 2
1.3. Polymer-Based Nanomedicine for Treatment of Lung Infections 3
1.4. Challenges in the Treatment of Lung Infections Using Polymeric Nanoparticles as Delivery Carriers 4
1.5. Scope of this Dissertation 5

CHAPTER II CONSTRUCTION OF A REACTIVE DIBLOCK COPOLYMER, POLYPHOSPHOESTER-*BLOCK*-POLY(L-LACTIDE), AS A VERSATILE FRAMEWORK FOR FUNCTIONAL MATERIALS THAT ARE CAPABLE OF FULL DEGRADATION AND NANOSCOPIC ASSEMBLY FORMATION 9

2.1. Introduction 9
2.2. Results and Discussions 12
2.3. Experimental Section 21
2.4. Conclusions 29

CHAPTER III PREPARATION AND *IN VITRO* ANTIMICROBIAL ACTIVITY OF SILVER-BEARING DEGRADABLE POLYMERIC NANOPARTICLES OF POLYPHOSPHOESTER-*BLOCK*-POLY(L-LACTIDE) 30

3.1. Introduction 30
3.2. Results and Discussions 34
3.3. Experimental Section 65
3.4. Conclusions 82

CHAPTER IV DEVELOPMENT OF A VINYL ETHER-FUNCTIONALIZED POLYPHOSPHOESTER AS A TEMPLATE FOR MULTIPLE POSTPOLYMERIZATION CONJUGATION CHEMISTRIES AND STUDY OF CORE DEGRADABLE POLYMERIC NANOPARTICLES 84

4.1. Introduction 84
4.2. Results and Discussions 88
4.3. Experimental Section 121
4.4. Conclusions 135

CHAPTER V CONCLUSIONS 137

REFERENCES 141

LIST OF FIGURES

Page

Figure 1.1. Organocatalysts used for ROP cyclic esters. 3

Figure 1.2. Representative research description in Chapter II. 6

Figure 1.3. Representative research description in Chapter III. 7

Figure 1.4. Representative research description in Chapter IV. 8

Figure 2.1. Synthetic route for the preparation of alkyne-functionalized $PBYP_{49}$-*b*-$PLLA_{44}$, 2, by one pot-sequential ROP, followed by post-polymerization modifications *via* thiol-yne "click"-reactions using either 3-mercaptopropionic acid or 2-aminoethanethiol to prepare $aPPE_{49}$-*b*-$PLLA_{44}$, 3, and $cPPE_{49}$-*b*-$PLLA_{44}$, 4, respectively, and finally, schematic illustration of the assembly of 3 and 4 into spherical micelles by direct dissolution in water to afford anionic and cationic micelles, 5 and 6, respectively (aPPE = anionic PPE and cPPE = cationic PPE).....12

Figure 2.2. (a) Kinetic plots of M_n and M_w/M_n *vs.* monomer conversion in ROP of BYP, obtained from GPC analysis. (b) GPC traces as a function of polymerization time. (c) Pseudo-first-order kinetic plots of $\ln([M]_0/[M])$ *vs.* time, obtained from ^{31}P NMR spectroscopy data. Conditions: [BYP] = 5.7 M in CH_2Cl_2, [BYP]:[BnOH]:[DBU] = 50:1:2. 14

Figure 2.3. (a) Kinetic plots of $\ln([M]_0/[M])$ *vs.* time, obtained from ^1H NMR spectroscopy data. (b) GPC traces (DMF as eluent, 1 mL/min) as a function of polymerization time, for the chain extension of LLA to PBYP after a solution of LLA in CH_2Cl_2 was added at 7 min of homopolymerization of BYP. (c) Kinetic plots of M_n and M_w/M_n *vs.* monomer conversion, obtained from GPC analysis, during the chain extension of PBYP with PLLA *via* one-pot sequential ROPs. Conditions: [LLA] = 0.72 M in CH_2Cl_2, [LLA]:[PBYP] = 50:1. 16

Figure 2.4. ^1H- and ^{31}P-NMR spectra of 2 (a), and product polymers after thiol-yne "Click" reactions, 3 (b) and 4 (c). 19

Figure 2.5. Self-assembly results of anionic micelle 5 (a and b) and cationic micelle 6 (c and d) in MOPS buffer at pH 7.4 and acetate buffer at pH 5.0, respectively. (a) TEM image of 5: D_{av} = 18 ± 3 nm, after counting more than 150 nanoparticles. (b) DLS results of 5: $D_{h(intensity)}$ = 41 ± 14 nm,

$D_{h(volume)}$ = 31 ± 10 nm, and $D_{h(number)}$ = 25 ± 6 nm. (c) TEM image of 6: D_{av} = 16 ± 2 nm, after counting more than 150 nanoparticles. (d) DLS results of 6: $D_{h(intensity)}$ = 125 ± 129 nm, $D_{h(volume)}$ = 24 ± 15 nm, and $D_{h(number)}$ = 16 ± 5 nm. 20

Figure 2.6. Zeta potential values of micelles, 5 and 6, in MOPS buffer at pH 7.4 and acetate buffer at pH 5.0. The average values and their standard deviations were made from six-time measurements. 21

Figure 3.1. Synthetic route for the preparation of alkyne-functionalized diblock copolymer of phosphoester and L-lactide, PPE-*b*-PLLA, 1, by one-pot sequential ROP, followed by postpolymerization modification *via* thiol-yne "Click" reaction using 3-mercaptopropionic acid to prepare anionic amphiphilic diblock copolymer, aPPE-*b*-PLLA, 2. 36

Figure 3.2. Schematic illustration of the self-assembly of 2a–2c into anionic micelles, 3a–3c, by direct dissolution in water followed by silver loading. Schematic representation of silver cation, Ag^+, (blue ball) from AgOAc and SCC22 or SCC10 (yellow ball) chelated into the corona or incorporated into the core of 3, Prepared from 2. (Note: the placements of the silver species within the dNP framework are proposed locations that have not been confirmed experimentally.) 37

Figure 3.3. Dynamic light scattering histograms. Average values from 10 measurements, with standard deviations calculated as the breadth of the distributions. Green bars: $D_{h(intensity)}$, red bars: $D_{h(volume)}$ and blue bars: $D_{h(number)}$. Top row: (a) naked 3a, (b) AgOAc-3a, (c) SCC22-3a, and (d) SCC10-3a. Middle row: (e) naked 3b, (f) AgOAc-3b, (g) SCC22-3b, and (h) SCC10-3b. Bottom row: (i) naked 3c. 38

Figure 3.4. AFM height and three-dimensional images of (a) and (b) 3a: height = *ca.* 4 nm and D_{av} = 38 ± 5 nm, (c) and (d) 3b: height = *ca.* 7 nm and D_{av} = 65 ± 11 nm, and (e) and (f) 3c: height = *ca.* 9 nm and D_{av} = 73 ± 18 nm, respectively, after counting more than 50 nanoparticles. 40

Figure 3.5. Ag-loading capacities (%) (left axis; bars) and efficiencies (%) (right axis; lines and symbols) of AgOAc-3a, AgOAc-3b, SCC22-3a, SCC22-3b, SCC10-3a or SCC10-3b with varying silver feed (*i.e.*, 10 and 40% (w/w) of AgOAc or 50 and 100% (w/w) of SCC22 and SCC10 with respect to the mass of the polymers in the NP solutions). (Average values were calculated from triplicate experiments.) 43

Figure 3.6. (a, c, and e) TEM bright-field and (b, d, and f) STEM dark-field images (drop deposited on carbon-coated copper grids with no stain) of AgOAc-3b, SCC22-3b, and SCC10-3b. 45

Figure 3.7. TEM images (drop deposited on carbon-coated copper grids and stained negatively with 1% (w/v) aqueous uranyl acetate) of (a) naked 3a, (b) naked 3b, (c) naked 3c, (d) AgOAc-3b, (e) SCC22-3b, and (f) SCC10-3b. . 46

Figure 3.8. STEM dark-field images (drop deposition on carbon-coated copper grids with no stain) and EDX spectrum profile analysis of AgOAc-3b ((a) and (b), respectively), SCC22- 3b ((c) and (d), respectively) and SCC10-3b ((e) and (f)), respectively). 48

Figure 3.9. High-resolution TEM images with elemental silver particles, found with (a) AgOAc-3b, (b) SCC22-3b, and (c) SCC10-3b, which were measured to have metallic Ag lattice spacing = 2.36 ($d_{Ag(111)}$) or 2.05 Å ($d_{Ag(200)}$). (For clarity, isolated elemental Ag^0 particles were selected to identify their lattice spacing.) 49

Figure 3.10. Release profiles of silver from dialysis cassettes containing solutions of silver compounds (AgOAc, SCC22 or SCC10) or silver-loaded 3a and 3b at 37 °C in nanopure water. (Averages were calculated from triplicate experiments.) 51

Figure 3.11. UV-vis spectra of control samples (naked 3b, AgOAc, and SCC22) and silver-loaded 3b after purification by centricon centrifugal filtration. The observance of no signals between 380–440 nm confirmed the absence of large silver particles (*ca*. >10 nm). 51

Figure 3.12. Synthetic illustration of enzymatic (left) or hydrolytic (right) degradation of 3b. 53

Figure 3.13. Study of dNP stability by using DLS. Changes in the hydrodynamic diameter (nm) of nanoparticles, 3b, at pH 5.0 (a) or pH 7.4 (b) at 37 °C over time. The average values from 10 measurements, with the standard deviations calculated as the breadth of the distributions, are shown. 54

Figure 3.14. Changes in ζ-potentials for 3b at pH 5.0 (black) or pH 7.4 (red) at 37 °C over time. 55

Figure 3.15. Changes of the ^{31}P NMR resonance of PPE backbone of 3b at t=0 (black) (a) and t = 35 days (b) at pH 7.4 at 37 °C. 55

Figure 3.16. ESI MS analysis of the degradation products of nanoparticles, 3b. Mass spectra in negative ion mode; *m/z* range of 400–2000 (a) and 50–400 (b). See Figure 3.17. for the MS/MS spectrum of j. 57

Figure 3.17. MS/MS spectrum of *m/z* 281. 58

Figure 3.18. Degradation profiles of 3b in Tris-HCl buffer (100mM, pH 7.4) at 37 °C over 36 h, in the presence of proteinase K (black) and porcine liver esterase (red) and in the absence of enzyme (control, blue). 59

Figure 3.19. Minimum inhibitory concentration (MIC, μg/mL Ag) profiles of silver-compounds (AgOAc, SCC22 and SCC10) and silver-bearing micellar nanoparticles (AgOAc-3b, SCC22-3a, SCC22-3b and SCC10-3b) against (a) eight uropathogenic strains of *E. coli* and (b) 10 contemporary epidemic strains of *S. aureus*. 61

Figure 4.1. Synthetic route for the preparation of ethylene glycol vinyl ether-functionalized cyclic phosphotriester monomer 1 and homopolymer 2 by ROP followed by postpolymerization modifications *via* three different types of conjugation chemistries: Thiol-ene "click" reaction, acetalization, or thio-acetalization reaction.....89

Figure 4.2. ^{1}H (300 MHz, $CDCl_3$, ppm) and ^{31}P (121 MHz, $CDCl_3$, ppm, inset) NMR spectra of 1. 90

Figure 4.3. (a) Kinetic plots of $\ln([M]_0/[M])$ *vs.* polymerization time (min), obtained from ^{31}P NMR spectroscopy data. (b) Kinetic plots of M_n and M_w/M_n *vs.* monomer conversion in ROP of 1, obtained from GPC analysis. (c) GPC traces as a function of elution time (min), after work-up of aliquots of the polymerization mixture by quenching with a solution of excess of benzoic acid in DCM and precipitation into diethyl ether. Conditions: [EVEP] = 5.2 M in DCM, [EVEP]:[BnOH]:[DBU] = 100:1:3. 92

Figure 4.4. ^{1}H (300 MHz, CD_2Cl_2, ppm) and ^{31}P (121 MHz, CD_2Cl_2, ppm, inset) NMR spectra of (a) 2, (b) 3, (c) 4, and (d) 5. 94

Figure 4.5. GPC traces of 2 and 3, before and after thiol-ene "click" reaction, respectively, as a function of elution time (min). 96

Figure 4.6. Synthetic route for the preparation of amphiphilic diblock copolymer 6 and schematic illustration of the assembly of 6 into micelles 7 by direct dissolution in water followed by the hydrolytic core degradation of 7. 101

Figure 4.7. (a) ^{1}H (300 MHz, CD_2Cl_2, ppm) and ^{31}P (121 MHz, CD_2Cl_2, ppm, inset) NMR spectra of 6. (b) GPC traces of macroinitiator, $mPEG_{44}$-OH, and diblock copolymer 6, $mPEG_{44}$-*b*-$PEVEP_{33}$, as a function of elution time (min).....101

Figure 4.8. ζ-Potential values of 7 in acetate buffer solutions at pH 5.0 and in MOPS buffer solutions at pH 7.4. The average values and their standard deviations, from three measurements, are shown. 104

Figure 4.9. Self-assembly results of micelle 7 in water. (a) DLS results of 7: $D_{h(intensity)}$ = 49 ± 7 nm, $D_{h(volume)}$ = 46 ± 7 nm, and $D_{h(number)}$ = 44 ± 6 nm (PDI = 0.114). (b) TEM image of 7: D_{av} = 39 ± 5 nm, after counting more than 150 nanoparticles. AFM height image (c) and three-dimensional image (d) of 7: D_{av} = 40 ± 7 nm, after counting more than 100 nanoparticles. 105

Figure 4.10. (a) Rate of the PEVEP backbone degradation of 7 at pH 5.0 (black line) or pH 7.4 (red line) at 37 °C as a function of time, as measured by a comparison of the integrals of initial to the newly appeared ^{31}P NMR resonances. Changes in the ^{31}P NMR resonance of PEVEP backbone of 7 at pH 5.0 (b) and 7.4 (c) at 37 °C over a period of time. 107

Figure 4.11. Rate of formation of acetaldehyde or disappearance of vinyl proton resonance at pH 5.0 (a) and pH 7.4 (b) and at 37 °C as a function of time, as measured by a comparison of the integrals of vinyl and acetaldehyde proton resonance. Transition of proton resonances of acetaldehyde and vinyl groups at pH 5.0 (c) or pH 7.4 (d) and at 37 °C over a period of time. 109

Figure 4.12. Study of the micelle stability by using DLS. Changes in the hydrodynamic diameter of micelles at pH 5.0 (a) or pH 7.4 (b) and at a temperature of 25 °C (black line) or 37 °C (red line) over a period of time. (c) Changes in the relative intensity of micelles in different environments, pH and temperature, over a period of time. The average values and their standard deviations, from three measurements, are shown. 112

Figure 4.13. ESI MS analysis of the degradation products of 8. Mass spectra in negative ion mode; *m/z* range of 100–2000 (a) and 50–180 (b). See Figures 4.14. and 4.15. for MS/MS spectra of f_1 and g_1. 115

Figure 4.14. MS/MS spectrum of *m/z* 309. 116

Figure 4.15. MS/MS spectrum of *m/z* 353. 116

Figure 4.16. GC MS analysis of the degradation products of 8. (a) Extracted ion chromatogram at *m/z* 62. (b) EI MS at retention time 4.74 min. 117

Figure 4.17. MALDI-TOF MS spectrum of the degradation products of 8. 118

Figure 4.18. Cytotoxicity of the parent micelles of mPEG$_{44}$-*b*-PEVEP$_{33}$ 7 (black line) and their degradation products 8 (red line) at a concentration range of 3–3000 μg/mL for 24 h in RAW 264.7 mouse macrophages (a) and OVCAR-3 human ovarian adenocarcinoma cells (b). 119

Figure 4.19. DSC traces for $mPEG_{44}$-OH, $PEVEP_{50}$, $mPEG_{44}$-*b*-$PEVEP_{33}$ and a physical mixture of $mPEG_{44}$-OH and $PEVEP_{50}$. The crash-cooling (CC) samples are those which were crash-cooled from 100 °C into liquid nitrogen before heating. (a) Trace over the region of interest (-60–60 °C) for the system, offset to increase clarity. (b) Rescaled trace (-50–60 °C) to contrast the glass transition regions for all samples. 121

LIST OF TABLES

Table 3.1. Summary of characterization data from naked nanoparticles of aPPE-*b*-PLLA, 3, as measured by TEM, DLS, AFM, and electrophoretic light scattering. 39

Table 3.2. Silver-loading capacity (%) and efficiency (%) of 3a and 3b with three different types of silver compounds (AgOAc, SCC22 and SCC10). (Average values were calculated from triplicate.)..... 44

Table 3.3. Summary of characterization data from silver-loaded 3a and 3b, as measured by TEM and DLS. 47

Table 3.4. Analysis of Ag-release kinetics from Ag-loaded 3a and 3b at 37 °C in nanopure water (conducted in triplicate). 52

Table 3.5. Average MICs (μg/mL Ag) and % improvements of silver compounds (AgOAc, SCC22 and SCC10) and silver-bearing micellar nanoparticles (AgOAc-3b, SCC22-3a, SCC22-3b, and SCC10-3b) against eight uropathogenic strains of *E. coli*. 62

Table 3.6. Average MICs (μg/mL Ag) and % MIC improvement for silver compounds (AgOAc, SCC22 and SCC10) and silver-bearing micellar nanoparticles (AgOAc-3b, SCC22-3a, SCC22-3b and SCC10-3b) against 10 contemporary epidemic strains of *S. aureus*. 62

Table 3.7. Minimum inhibitory concentrations (MICs) and statistical significance (*p*) values of parent silver compounds (AgOAc, SCC22 and SCC10) and silver-bearing micellar nanoparticles (AgOAc-3b, SCC22-3a, SCC22-3b and SCC10-3b) against 8 uropathogenic strains of *E. coli* and 10 contemporary epidemic strains of *S. aureus*. (Note: *p* values for MIC comparisons of silver-bearing micellar nanoparticles *vs.* parent silver compounds are shown.)..... 63

Table 4.1. Comparisons of Glass Transition Temperatures, T_g, of the Prepared Polymers, As Measured by Differential Scanning Calorimetry (DSC). 103

CHAPTER I

INTRODUCTION AND LITERATURE REVIEW

1.1. Background and Motivation

Serious lung infections, such as pneumonia, tuberculosis and chronic obstructive cystic fibrosis (CF)-related bacterial diseases, are increasingly difficult to treat and can be life-threatening. A number of therapeutics and/or diagnostics have been exploited for treatment and/or diagnosis of pulmonary infections. However, poor solubility of some antimicrobial agents, unfavorable pharmacokinetics, lack of selectivity for penetration into diseased tissues, advent of bacteria with multiple drug resistances[1,2] and, as a result, administration of higher-intensity antibiotic regimens pose significant obstacles to optimizing therapeutics.[3] A promising approach to alleviate these critical barriers in traditional treatment is the development of engineered nanoparticles (NPs) – *i.e.* particles in the size range 1–1000 nm – as alternative delivery carriers for a wide range of therapeutics, including drugs, antibodies, proteins, nucleic acids, and various diagnostic agents.[2,4] A wide range of types of NPs, such as dendrimers, fullerenes, metallic NPs, *etc*., have been loaded with therapeutic agents and/or imaging probes to improve pharmacokinetics and biodistribution profiles of their small-molecule cargo, aiming to achieve maximum delivery to diseased tissues while reducing the exposure of healthy tissues to the introduced materials.[5-8] Among the diverse selection of nanocarriers, NPs constructed from polymeric backbone-structured building blocks offer precise control over their architectures, surface characteristics, and supramolecular assembly.[9,10] Direct

delivery of polymeric NPs, loaded with appropriate antimicrobials and equipped with "smart" features to overcome various mucosal and cellular barriers, is a promising approach to optimally localize treatment to the site of infection with minimal systemic adverse effects or toxicity from the applied therapeutic agents.

1.2. Organocatalyzed Ring-Opening Polymerization

Synthesis of polymers with predictable molecular weight, high end group fidelity and low polydispersity has been a tremendous interest in the last decades. Conventionally, ring-opening polymerization (ROP) of cyclic esters were mediated by metals such as Al or Sn.[55, 56] However, these metal catalysts typically follow unavoidable concerns in the field of electronic and medical applications as the residual metals may affect the quality of the product. To address these issues, cyclic carbenes and bifunctional thiourea amines (1, 2) were employed as effective catalysts for cyclic esters, but the prolonged reaction time was a hurdle to surmount (Figure 1.1.).[57, 58] Recently, there has been a considerable interest in bicyclic guanidine-based organocatalysts, *e.g.* 1,5,7-triazabicyclo-[4,4,0]dec-5-ene (3, TBD) (pKa = 26.0) and 7-methyl-1,5,7-triazabicyclo-[4,4,0]dec-5-ene (4, MTBD) (pKa = 25.3) or in structurally similar amine bases, *e.g.* 1,8-diazabicyclo[5,4,0]unde-7-ene (5, DBU) (pKa = 24.3), for their controlled high activity for solution-phase ROP of cyclic esters.[59, 60]

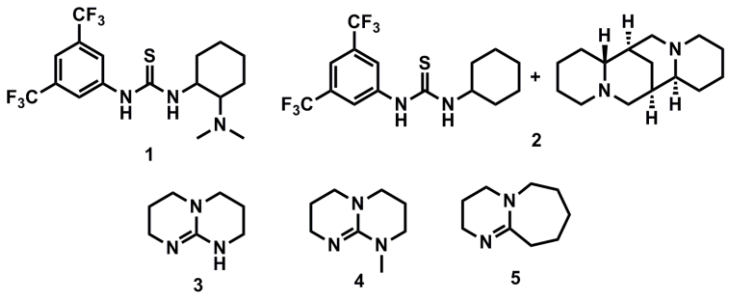

Figure 1.1. Organocatalysts used for ROP cyclic esters.

Degradable polymers such as aliphatic polyesters, polycarbonates, and polyphosphoesters have been of interest as materials for biomedical applications due to their low toxicity, biocompatibility and degradability.[14-16] Also, the synthetic versatility of cyclic esters has brought even more attention in the preparation of functional degradable polymers by ROP. As for the precise control over the physical properties and the applications of biologically-active molecules to the degradable polymer structures, however, postpolymerization modification provides a more facile means to introduce a desired functionality since not all functional groups may be compatible with the ROP process or the additional functionalities may limit the polymerization efficiency.[69] As a result, the postpolymerization processing of the polymer backbone or side chains is inevitable, and it has been studied extensively with efficient and versatile chemistries.[70-72]

1.3. Polymer-Based Nanomedicine for Treatment of Lung Infections

A myriad of antimicrobials have been developed for the treatment of lung infectious diseases,[11] yet several key barriers remain. These barriers include reduced patient compliance to the prescribed regimens in the long-term therapy, emergence of

multi-drug resistant bacteria, drug toxicity from multiple daily doses, *etc*., representing a need for optimized design of an efficient delivery platform for the lungs.[12] To address these limits in the treatment of lung infections, advances in nanomedicine hold a great promise for the delivery of therapeutic agents.[13-16] In general, incorporation of therapeutics into polymeric NPs offers precise control over particle composition, size, and structure contributing to the improved pharmacokinetics, enhanced aqueous solubility of insoluble hydrophobic drugs, stabilization of therapeutic agents against possible hydrolytic and/or enzymatic degradation, mediation of sustained and/or stimuli-responsive release of the payloads, and mimicking natural nanosystems, *e.g.* viruses, lipoproteins and proteins, for cell-specific targeted delivery with increased bioavailability, *etc.*[2,3,9,10] Specific to drug and gene delivery, several reports have highlighted the prolonged retention time and alleviated mucociliary clearance, leading to a reduction of the required dose, by employing polymeric nano-carriers in the treatment of respiratory diseases.[17] Furthermore, the feasibility of incorporation of surface-decorating moieties (such as selective cell-targeting peptides) onto polymeric NPs represents a route toward enhancement of the ratio of drug concentrations at diseased tissue to normal tissue with minimal systemic adverse effects.

1.4. Challenges in the Treatment of Lung Infections Using Polymeric Nanoparticles as Delivery Carriers

Some of the major challenges associated with pulmonary NP delivery include mucociliary clearance, steric hindrance, adhesiveness, and enzymatic activity of the mucus gel or sputum, and uptake by alveolar macrophages, *etc.*[18-21] For instance,

delivery of drugs or nucleic acids loaded within nanocarriers into the airways for treatment of CF-related bacterial infections is inefficient, ascribed mostly to the presence of sputum having a bulk viscosity *ca.* 10^5 times greater than water.[19,22,23] As a delivery carrier, destabilization of NPs can be a direct consequence of drug leakage, disassembly and/or biodegradation of the particles, detachment of surface-decorating moieties, opsonization, *etc*.[9,13] Even though the drug encapsulation-strategy into NPs has shown the superiority in targeting and sustained release, as compared to free drugs, it still suffers from rapid clearance by the mononuclear phagocytic system (MPS) upon deposition onto the lungs.[24] Furthermore, exhalation, effects of degradation products, cytotoxicity, immunogenicity, *etc*. should be also accounted for in the design and administration of polymeric NPs for treatment of respiratory diseases.[25]

1.5. Scope of this Dissertation

This dissertation is focused on the development of highly well-defined polymeric NPs demonstrating unique performance toward the effective treatment of infectious diseases, the combination of state-of-the-art polymerization chemistry, *e.g.* anionic ROP, postpolymerization, and supramolecular assembly processes.

In Chapter II, a diblock copolymer, polyphosphoester-*block*-poly(L-lactide) (PPE-*b*-PLLA), which has potential for being fully degradable and biocompatible, was synthesized by one-pot sequential ROPs (Figure 1.2.). Subsequently, photoinduced thiol-yne "click" reactions with small-molecule thiols bearing either carboxylic acid or amino groups afforded amphiphilic diblock copolymers. Finally, direct dissolution of

the two different types of amphiphilic diblock copolymers in aqueous solutions yielded well-defined spherical micelles.

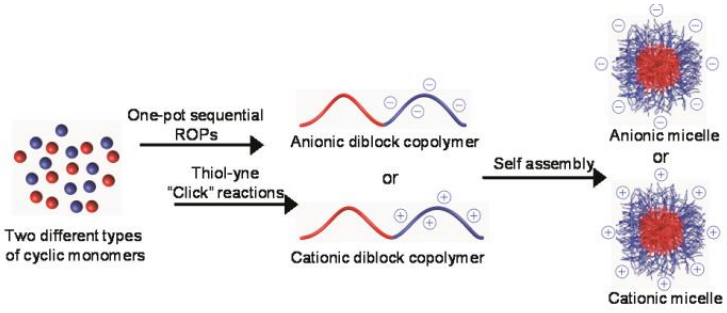

Figure 1.2. Representative research description in Chapter II.

In Chapter III, a series of anionic dNPs from block copolymers having PPE and PLLA block segments, designed specifically for silver loading into the hydrophilic shell and/or the hydrophobic core, were prepared (Figure 1.3.). With the use of three different types of silver-based antimicrobials – silver acetate (AgOAc) or one of two silver carbene complexes (SCCs), comparative studies of the selection of proper dNP templates for silver-loading and release were undertaken. Then, the comprehensive degradation studies, including evaluation of hydrolytic or enzymatic degradability and identification of the degradation products, were performed for the fundamental understanding of the developed dNPs as potential delivery carriers for silver-based antimicrobials. Finally, *in vitro* antimicrobial efficacy of the selected Ag-dNPs was compared with that of inherent silver compounds against 10 contemporary epidemic strains of *Staphylococcus aureus* and eight uropathogenic strains of *Escherichia coli*.

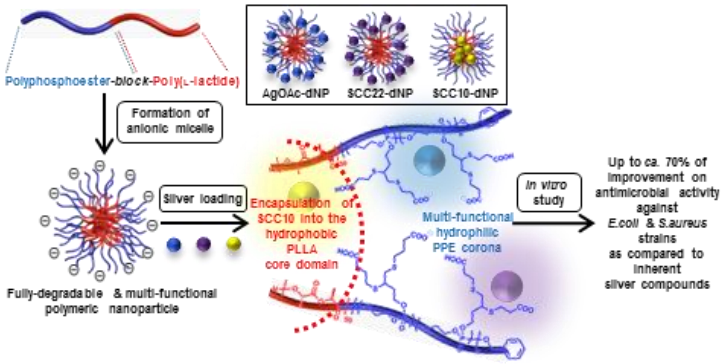

Figure 1.3. Representative research description in Chapter III.

In Chapter IV, PPE with vinyl ether side chain functionality was developed as a versatile template for postpolymerization modifications, and its degradability and biocompatibility were evaluated (Figure 1.4.). This vinyl ether-functionalized PPE scaffold was coupled with hydroxyl- or thiol-containing model small molecules *via* three different types of conjugation chemistries – thiol–ene "click" reaction, acetalization, or thio–acetalization reaction – to afford modified polymers that accommodated either stable thio-ether or hydrolytically-labile acetal or thio-acetal linkages. Amphiphilic diblock copolymers of poly(ethylene glycol) and PEVEP formed well-defined micelles with a narrow and monomodal size distribution in water. The stability of the micelles and the hydrolytic degradability of the backbone and side chains of the PEVEP block segment were evaluated, and the cytotoxicity o the parent micelles and their degradation products were assessed *in vitro*.

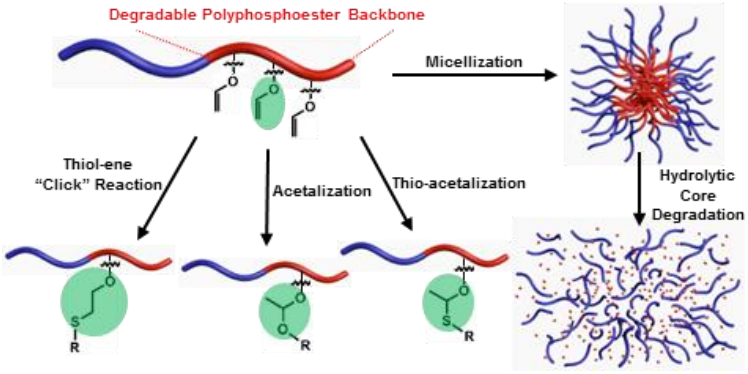

Figure 1.4. Representative research description in Chapter IV.

CHAPTER II

CONSTRUCTION OF A REACTIVE DIBLOCK COPOLYMER, POLYPHOSPHOESTER-*BLOCK*-POLY(L-LACTIDE), AS A VERSATILE FRAMEWORK FOR FUNCTIONAL MATERIALS THAT ARE CAPABLE OF FULL DEGRADATION AND NANOSCOPIC ASSEMBLY FORMATION*

2.1. Introduction

The use of hydrocarbon backbone-based polymers in the development of polymeric nanoconstructs is a well-established concept in nanomedicine, but toxicity, immunogenicity, and other side effects from long-time accumulation in the human body are often an inevitable bottleneck in the field of therapeutics, imaging, diagnostics, and drug delivery.[26] To overcome this fatal drawback, hydrolytically-degradable polymers such as polyesters and polycarbonates have been studied as potential biomaterials owing to their low toxicity, biocompatibility, and degradability.[27,28]

In spite of their great promises in nanomedicine, elaborate synthetic approaches due to difficulties experienced in controlling polymerizations, challenges in the introduction of functionalities, incompatibilities of desired functionalities with polymerization methods, and tedious workup processes often present challenges toward

*Part of this work is reprinted with permission from "Construction of a Reactive Diblock Copolymer, Polyphosphoester-*block*-Poly(L-lactide), as a Versatile Framework for Functional Materials That Are Capable of Full Degradation and Nanoscopic Assembly Formation" by Lim, Y. H., Heo, G. S., Cho, S., and Wooley, K. L., 2013, *ACS Macro Lett*., 2(9), 785–789. Copyright [2013] by the American Chemical Society.

developing well-defined, functional degradable biomaterials.[29-31] A broad range of organocatalysts have been studied extensively in ring-opening polymerizations (ROPs),[32-35] which offer controllability while avoiding potential purification issues and biological complications of the traditional metal-based catalyst systems.[36,37] Although there are exceptions,[38] the introduction of side-chain functionalities into the cyclic monomers commonly involves multistep reactions. In contrast, cyclic phospholanes offer a straightforward, single-step installation of reactive functionalities that are compatible with the ROP conditions and also provide opportunities for diverse postpolymerization modification reactions, including "click"-type reactions.[39-43] Introducing these "clickable" functionalities onto cyclic monomers is of particular interest with respect to the synthetic approach to degradable polymers, as this sequence of chemistry would not only broaden the synthetic versatility but also enable the construction and fabrication of intricate polymeric nanoparticles for pharmaceutical applications.[39,40]

"Hybrid" polymers can provide a mechanism to accommodate disparate physical, chemical, and mechanical advantages from diverse polymer segments.[44-47] Particularly, integrating heterogeneous degradable polymers into one polymeric system is expected to enhance the combinatorial effects on the development of versatile polymer frameworks, which is often limited in the case of a single-type copolymer backbone system. Among important biomedical degradable polymers, polylactide (PLA)[48-51] is an interesting building block for the construction of functional nanoscopic objects, due to its capability for hydrolytic and/or enzymatic degradation and several elegant works on the formation

of well-defined polymeric nanostructures with distinctive core–shell morphologies and higher-order complexities based on the adaptation of the intrinsic hydrophobicity and crystallinity of PLAs within amphiphilic block copolymers.[52-55] Therefore, we have combined our recent exploration into a rapid and facile construction of nanostructures derived from a biomimetic polyphosphoester[56-60]-based block copolymer system[39,40] with PLA.

The first attempt to prepare a diblock copolymer of L-lactide (LLA) and phospholane, PLLA-*b*-PPE, was made by Wang *et al.*;[61] however, it required demanding two-step polymerizations using metal catalyst, $Sn(Oct)_2$, and no functional moieties were incorporated into the polymeric system. In this report, we demonstrate the preparation of fully degradable, hybrid, functional diblock copolymers by one-pot sequential ROPs of two different kinds of cyclic monomers, phospholane and LLA, using an organocatalyst, 1,8-diazabicyclo[5,4,0]undec-7-ene (DBU). This platform was, subsequently, modified by a radical-mediated "click"-type thiol-yne reaction to endow charges and functional side-chain moieties to the polyphosphoester (PPE) segment. The obtained functionalized diblock copolymers, in turn, were demonstrated to self-assemble into well-defined spherical nanoparticles in aqueous solutions with corresponding surface charges, as characterized by transmission electron microscopy (TEM), dynamic light scattering (DLS), and zeta potential analyses.

2.2. Results and Discussions

Compared to our previous reports, in which sequential ROPs of two phospholanes were conducted at different temperatures on a Schlenk line, the ROPs of butynyl phospholane (BYP, **1**)[40] and LLA were performed in a one-pot manner in a glovebox, at ambient temperature, and with convenience in the elimination of potential introduction of water as a competitive initiator. In an initial study, homopolymer, PBYP, was prepared by employing DBU as the organocatalyst and benzyl alcohol as the initiator (Figure 2.1.). The conversion reached up to 95% with a low polydispersity index (PDI ~1.2) within 7 min in dichloromethane (CH_2Cl_2). After this initial screening reaction, kinetic studies of each sequence of the polymerizations in the glovebox were performed.

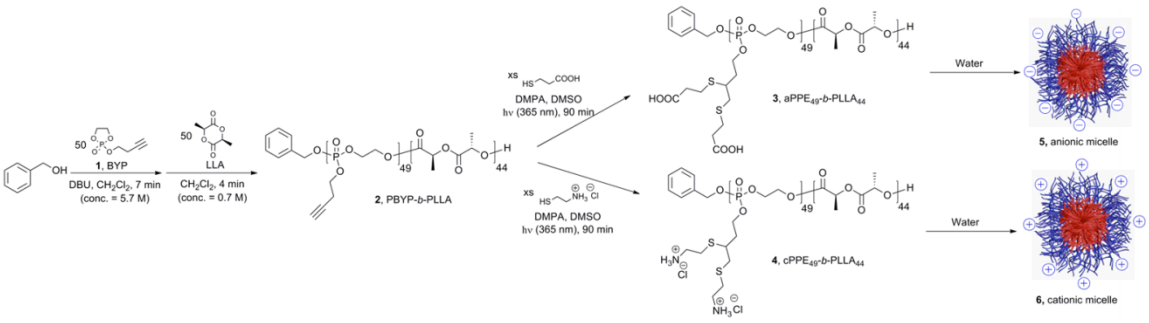

Figure 2.1. Synthetic route for the preparation of alkyne-functionalized $PBYP_{49}$-*b*-$PLLA_{44}$, 2, by one pot-sequential ROP, followed by post-polymerization modifications *via* thiol-yne "click"-reactions using either 3-mercaptopropionic acid or 2-aminoethanethiol to prepare $aPPE_{49}$-*b*-$PLLA_{44}$, 3, and $cPPE_{49}$-*b*-$PLLA_{44}$, 4, respectively, and finally, schematic illustration of the assembly of 3 and 4 into spherical micelles by direct dissolution in water to afford anionic and cationic micelles, 5 and 6, respectively (aPPE = anionic PPE and cPPE = cationic PPE).

For the kinetic studies, BYP and benzyl alcohol (molar ratio of 50:1) were mixed in CH_2Cl_2, DBU (molar ratio to initiator of 2:1) was added; and the polymerizations were monitored. After being stirred for a predetermined period of time, an aliquot of the reaction mixture was collected, quenched by addition of a solution of benzoic acid in CH_2Cl_2, and then analyzed by ^{31}P NMR spectroscopy and GPC (Figure 2.2.). While the conversions were calculated from ^{31}P NMR spectroscopy by comparing the integral ratios of two distinct peaks of monomer, **1**, at 17.34 ppm and homopolymer, PBYP, at –1.60 ppm, both the molecular weight and its distribution were determined by GPC. The GPC molecular weight values were of low accuracy because they are based on calibration with polystyrene standards; however, we believe that the molecular weight distributions are representative of the controlled nature of the polymerizations. Polymerization proceeded rapidly, in which the monomer conversion reached to 67% within the beginning 2 min. The maintenance of linearity of M_n *vs.* monomer conversion suggested a living ROP up to 95%. The PDIs were less than 1.30, and even lower PDI values (<1.20) were obtained when the monomer conversion was <95%. The increased PDI at higher monomer conversions could be attributed to adverse transesterification of the polyphosphoester backbone. Kinetic plots of $\ln([M]_0/[M])$ *vs.* time indicated pseudo-first order kinetics, which are a typical characteristic of ROP. The degrees of polymerization (DP) calculated based on ^{31}P NMR spectroscopy-determined monomer conversions agreed with those calculated from chain-end analysis by ^{1}H NMR spectroscopy, that is, by comparisons of the integrals of proton resonances of the benzyl group (7.42–7.30 ppm) of the initiated chain end to those of the PBYP backbone

(4.34–4.22 ppm) or those of the α- and β-protons on the substituents (4.22–4.08 ppm and 2.67–2.56 ppm, respectively).

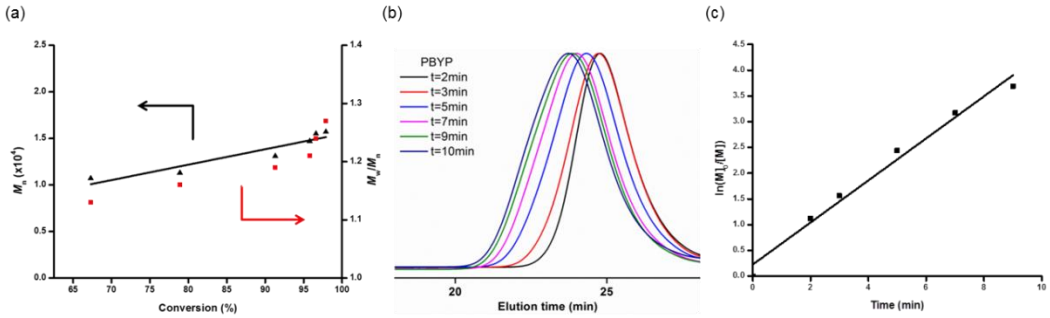

Figure 2.2. (a) Kinetic plots of M_n and M_w/M_n *vs.* monomer conversion in ROP of BYP, obtained from GPC analysis. (b) GPC traces as a function of polymerization time. (c) Pseudo-first-order kinetic plots of $\ln([M]_0/[M])$ *vs.* time, obtained from ^{31}P NMR spectroscopy data. Conditions: [BYP] = 5.7 M in CH_2Cl_2, [BYP]:[BnOH]:[DBU] = 50:1:2.

PBYP was extended with PLLA *via* a one-pot sequential polymerization method, which provides a facile strategy to prepare diblock copolymers with structural control in an atom-efficient and labor-saving approach. It is noteworthy that the ROP rate of phospholanes is strongly dependent on the monomer and organocatalyst concentrations.[40] Therefore, we speculated that manipulations of monomer concentration in solution would enable the construction of diblock copolymers, while maintaining a high efficiency of ROP of two cyclic monomers sequentially, each using DBU. For this reason, ROP of LLA was conducted after the formation of the PPE block. That is, when the concentration of BYP in the initial polymerization mixture was diluted from 5.7 to 0.28 M after consumption of 95% of BYP and further to 0.036 M and the DBU concentration was reduced from 0.23 to 0.028 M upon the addition of the second

monomer solution in CH_2Cl_2, the rate of BYP polymerization slowed to an immeasurable level, as confirmed by ^{31}P NMR spectroscopy. Therefore, addition of LLA in CH_2Cl_2 promoted an extension of the second block while preventing further growth of PBYP.

The kinetic study showed that the chain extension of PLLA was achieved within a few minutes with good control (Figure 2.3.). At 7 min of polymerization of BYP (after which a rapid increase in PDI was shown), a solution of LLA in CH_2Cl_2 was quickly added into the reaction mixture. An aliquot of the reaction solution was collected, quenched, and analyzed by ^1H NMR spectroscopy and GPC. The conversion of LLA had reached 90% with a low PDI (~1.2) after 4 min. A linearity of M_n *vs*. monomer conversion was observed during polymerization, up to 80% conversion with low PDIs (<1.20). Similar to the polymerization of BYP, the kinetic plots of $\ln([M]_0/[M])$ *vs*. time for LLA chain extension showed pseudo-first-order kinetics.

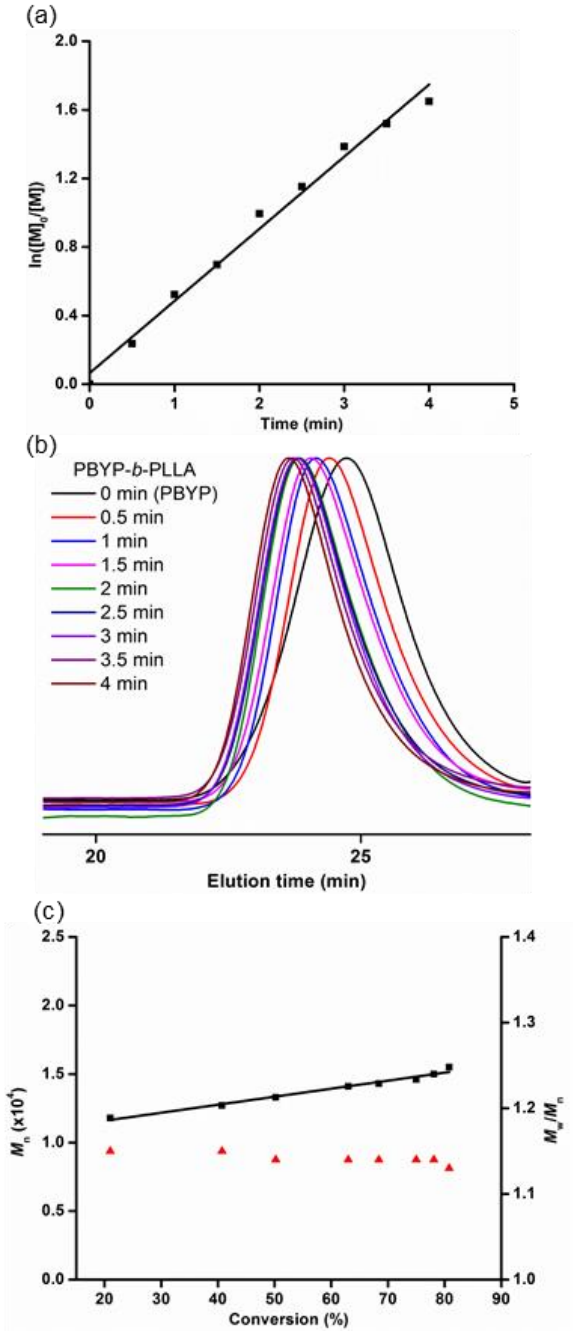

Figure 2.3. (a) Kinetic plots of $\ln([M]_0/[M])$ *vs.* time, obtained from ^{1}H NMR spectroscopy data. (b) GPC traces (DMF as eluent, 1 mL/min) as a function of polymerization time, for the chain extension of LLA to PBYP after a solution of LLA in CH_2Cl_2 was added at 7 min of homopolymerization of BYP. (c) Kinetic plots of M_n and M_w/M_n *vs.* monomer conversion, obtained from GPC analysis, during the chain extension of PBYP with PLLA *via* one-pot sequential ROPs. Conditions: [LLA] = 0.72 M in CH_2Cl_2, [LLA]:[PBYP] = 50:1.

A scaled-up production of **2** was then conducted using the same molar ratios as used for the kinetic studies, followed by precipitation in diethyl ether for purification. The DP values were determined by ^{1}H NMR and ^{31}P NMR spectroscopy end-group analysis and monomer conversion calculations, respectively. Furthermore, the integral ratios between the peak of the terminal acetylene proton (2.28–2.09 ppm) within the PBYP block and that of the methine or methyl protons on the PLLA block were consistent, which was indicative of retention of the alkyne groups. In addition, one distinct ^{31}P resonance confirmed the stability of the degradable PPE backbone during the ROP of LLA and isolation and characterization of the block copolymer. GPC analysis of the diblock copolymer showed a monomodal peak with PDI of 1.17.

To afford positive or negative charges along the backbone of one segment of the diblock copolymer, in the construction of amphiphilic block copolymers, thiol-yne "click" reactions were conducted to couple two different kinds of thiol-containing compounds onto the PPE block. The radical-mediated thiol-yne "click" chemistry is a robust and versatile method that tolerates a variety of functional groups in achieving a high degree of functionalization on alkyne groups.[62,63] Herein, this efficient click chemistry was applied to achieve double addition of small molecules at each PPE repeat unit by coupling two equivalents of thiols onto one alkyne moiety. This double conjugation of molecules onto the hydrophilic segment would maximize the number of functionalities as well as the solubility of the amphiphilic diblock copolymers in water. To confirm the integrity of the polyphosphoester and poly(L-lactide) backbones under the presence of radicals and UV irradiation, a mixture of polymer and 2,2-dimethoxy-2-

phenylacetophenone (DMPA) as a photo-initiator in dimethyl sulfoxide-d_6 (DMSO-d_6) was irradiated under UV light (365 nm, 6 W) for several hours, as a preliminary control reaction. Both ^{1}H and ^{31}P NMR spectra demonstrated that all of the functional groups and polymer backbones were intact under these conditions. Accordingly, ten molar equivalents of thiols relative to alkynes were employed in the radical reaction to avoid possible chain–chain coupling and to ensure a high coupling efficiency. 3-Mercaptopropionic acid and 2-aminoethanethiol were chosen because of their commercial availability and the potential self-assembly into anionic or cationic nanoparticles from the resulting negatively or positively charged amphiphilic block copolymers, respectively.

Figure 2.4. shows a comparison of ^{1}H and ^{31}P NMR spectra of PPE_{49}-*b*-$PLLA_{44}$ before and after thiol-yne "click" reactions. The approximately complete disappearance of the terminal acetylene proton (labeled as g in Figure 2.4.(a)), coincident with the emergence of distinguishable diastereotopic methylene protons (labeled as k in Figures 2(b) and 2(c)) confirmed the conversion of alkynyl groups into the corresponding 1,2-dithioether functional groups.

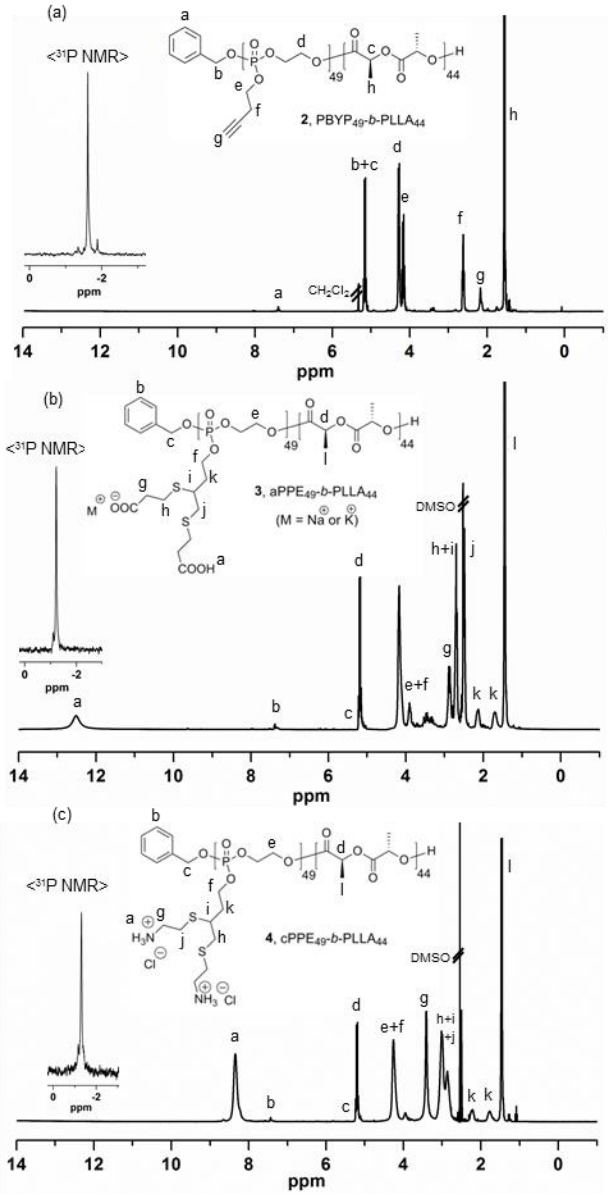

Figure 2.4. ^{1}H- and ^{31}P-NMR spectra of 2 (a), and product polymers after thiol-yne "Click" reactions, 3 (b) and 4 (c).

The self-assembly behaviors of the two amphiphilic diblock copolymers, **3** and **4**, were studied by direct dissolution in buffer solution. **3** and **4** were dissolved and stirred for 10 min in 3-(*N*-morpholino)propanesulfonic acid (MOPS) buffer solution (pH 7.4,

150 mM) and acetate buffer solution (pH 5.0, 150 mM), respectively, with polymer concentrations of 1.0 mg/mL. The morphologies of the resulting nanoparticles having different charges within their hydrophilic shells were characterized by DLS and TEM (Figure 2.5.). DLS results indicated narrow and monomodal size distributions of anionic and cationic nanoparticles. For **5**, the number-average hydrodynamic diameter was *ca.* 25 nm. The number-average hydrodynamic diameter of **6** was *ca.* 16 nm. Similarly, TEM images of **5** and **6** also showed uniform particles with average sizes of approximately 18 and 16 nm, respectively.

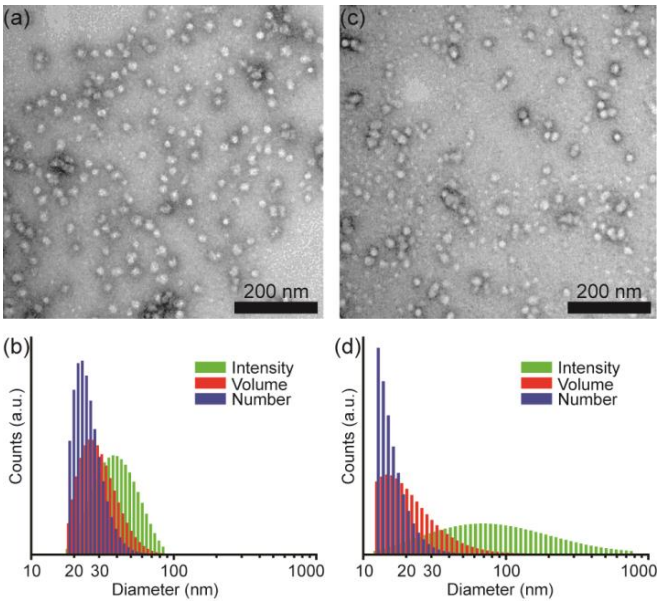

Figure 2.5. Self-assembly results of anionic micelle 5 (a and b) and cationic micelle 6 (c and d) in MOPS buffer at pH 7.4 and acetate buffer at pH 5.0, respectively. (a) TEM image of 5: D_{av} = 18 ± 3 nm, after counting more than 150 nanoparticles. (b) DLS results of 5: $D_{h(intensity)}$ = 41 ± 14 nm, $D_{h(volume)}$ = 31 ± 10 nm, and $D_{h(number)}$ = 25 ± 6 nm. (c) TEM image of 6: D_{av} = 16 ± 2 nm, after counting more than 150 nanoparticles. (d) DLS results of 6: $D_{h(intensity)}$ = 125 ± 129 nm, $D_{h(volume)}$ = 24 ± 15 nm, and $D_{h(number)}$ = 16 ± 5 nm.

The surface charge densities of **5** and **6** in buffer solutions at pH 5.0 and 7.4 were measured as zeta potential values (Figure 2.6.). As predicted, **5** were negatively charged with zeta potentials of –16.9 mV at pH 5.0 and –25.5 mV at pH 7.4, and **6** were positively charged, showing zeta potential values of +31.4 mV at pH 5.0 and +26.0 mV at pH 7.4. The distinct difference in zeta potential values demonstrated the presence of surface charges on the micelles as well as the potential utilization of functionalities for further modifications.

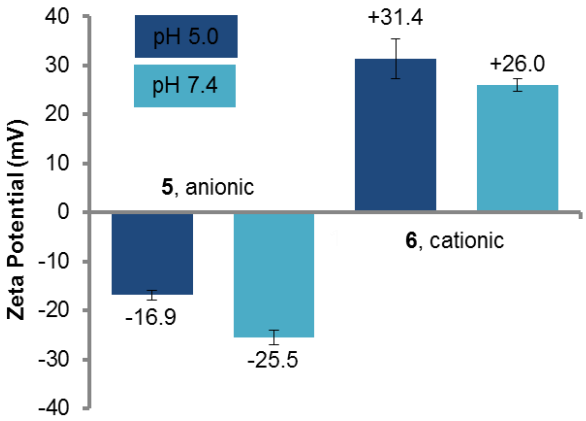

Figure 2.6. Zeta potential values of micelles, 5 and 6, in MOPS buffer at pH 7.4 and acetate buffer at pH 5.0. The average values and their standard deviations were made from six-time measurements.

2.3. Experimental Section

2.3.1. Materials

Dimethyl sulfoxide (DMSO), 3-Bytyn-1-ol, 3-mercaptopropionic acid, 2-aminoethanethiol, 2,2-dimethoxy-2-phenylacetophenone (DMPA), diethyl ether and benzoic acid were used as received from Sigma-Aldrich Co. 2-chloro-2-oxo-1,3,2-

dioxaphospholane (COP, 95%) was used as received from Thermo Fisher Scientific Inc. Benzyl alcohol and 1,8-diazabicyclo[5,4,0]undec-7-ene (DBU) were purchased from Sigma-Aldrich Co. and distilled from calcium hydride prior to use. L-lactide (98%, Alfa Aesar) was purified and dried by azeotropic distillation in toluene three times. The dried L-lactides were stored in an argon-filled glovebox. Tetrahydrofuran (THF) and dichloromethane (CH_2Cl_2) were dried through columns (J. C. Meyer Solvent Systems, Inc.). Spectra/Pro® membranes (MWCO 12–14 kDa, Spectrum Medical Industries, Inc. were used for dialysis.

2.3.2. Characterization Methods

^{1}H, ^{13}C, and ^{31}P NMR spectra were recorded on Inova 300 MHz spectrometers interfaced to a UNIX computer using VnmrJ software. Chemical shifts were referenced to solvent resonance signals.

The DMF gel permeation chromatography (GPC) was conducted on a Waters Chromatography, Inc. (Milford, MA) system equipped with an isocratic pump model 1515, a differential refractometer model 2414, and a four-column set of 5 μm Guard (50 x 7.5 mm), Styragel HR 4 5 μm DMF (300 x 7.5 mm), Styragel HR 4E 5 μm DMF (300 x 7.5 mm), and Styragel HR 2 5 μm DMF (300 x 7.5 mm). The system was equilibrated at 70 °C in pre-filtered DMF containing 0.05 M of LiBr, which served as polymer solvent and eluent (flow rate set to 1.00 mL/min). Polymer solutions were prepared at a concentration of *ca.* 5 mg/mL and an injection volume of 200 μL was used. Data collection and analysis were performed with Empower 2 v. 6.10.01.00 software (Waters,

Inc.). The system was calibrated with polystyrene standards (Polymer Laboratories, Amherst, MA) ranging from 615 to 442800 Da.

Thermogravimetric analysis (TGA) was performed under N_2 atmosphere using a Mettler-Toledo model TGA/SDTA851e, with a heating rate of 10 °C/min and cooling rate of 5 °C/min. Measurements were analyzed using Mettler-Toledo Star^e v. 7.01 software.

Glass transition temperatures (T_g) were measured by differentia scanning calorimetry (DSC) on a Mettler-Toledo DSC822® (Mettler-Toledo, Inc., Columbus, OH), with a heating rate of 10 °C/min. Measurements were analyzed using Mettler-Toledo Star^e v. 7.01 software. The T_g was taken as the midpoint of the inflection tangent, upon the third heating scan.

Dynamic light scattering (DLS) measurements were conducted using Delsa Nano C (Beckman Coulter, Inc., Fullerton, CA) equipped with a laser diode operating at 658 nm. Size measurements were made in nanopure water (n = 1.3329, η = 0.890 cP at 25 ± 1 °C). Scattered light was detected at 165° angle and analyzed using a log correlator over 70 accumulations for a 3.0 mL sample in a glass sizing cell (4.0 mL capacity). The samples in the glass sizing cell were equilibrated for 30 min before measurements were made. The photomultiplier aperture and the attenuator were automatically adjusted to obtain a photon counting rate of *ca.* 10 kcps. Calculation of the particle size distribution and distribution averages was performed using COTIN particle size distribution analysis routines. The peak averages of histograms from number distributions out of 70 accumulations were reported as the average diameters of the particles.

Transmission electron microscopy (TEM) images were collected on a JEOL 1200EX operating at 100 kV and micrographs were recorded at calibrated magnifications using a SIA-15C CCD camera. The samples as aqueous solutions (5 µL) were deposited onto carbon-coated copper grids. Excess sample was wicked off using filter paper and the grids were allowed to dry in air for 1 min. Following that, the grids were stained with 5 µL of a 2% uranyl acetate aqueous solution. Excess stain was wicked off using filter paper after 20 seconds. The sample grids were dried under vacuum overnight before analysis.

The zeta potential values of the nanoparticles were determined by Delsa Nano C particle analyzer (Beckman Coulter, Fullerton, CA) equipped with a 30 mW dual laser diode (658 nm). The zeta potential of the particles in suspension was obtained by measuring the electrophoretic movement of charged particles under an applied electric field. Scattered light was detected at a 30° angle at 25 °C. The zeta potential was measured at five regions in the flow cell and a weighted mean was calculated. These five measurements were used to correct for electroosmotic flow that was induced in the cell due to the surface charge of the cell wall. All determinations were repeated six times.

2.3.3. Synthesis of Butynyl Phospholane (BYP) Monomer

A solution of 2-chloro-2-oxo-1,3,2-dioxaphospholane (COP, 15.0 g, 105 mmol) in 50 mL of anhydrous THF was added dropwise to a stirred solution of 3-butyn-1-ol (8.12 g, 116 mmol) and triethylamine (11.7 g, 116 mmol) in 200 mL of anhydrous THF at 0 °C. The reaction mixture was allowed to stir for 11 h. The reaction mixture was

filtered and the filtrate was concentrated vial rotary evaporator. The filtrate was distilled under reduced pressure to obtain a faint yellow and viscous liquid (110–120 °C, 0.5 mmHg) with a yield of 52.3%. IR: 3330–3170, 3050–2870, 1474, 1283, 1009, 926, 835, 756 cm^{-1}. ^{1}H NMR ($CDCl_3$, ppm): δ 4.50–4.31 (m, 4H, POC*H*$_2$C*H*$_2$OP), 4.21 (dt, *J* = 9.3 Hz, *J* = 6.9 Hz, 2H, POC*H*$_2$CH$_2$C), 2.59 (ddt, *J* = 6.9 Hz, 2.7 Hz, 0.3 Hz, 2H, POCH$_2$C*H*$_2$C), 2.02 (t, *J* = 2.7 Hz, 1H, POCH$_2$CH$_2$CC*H*). ^{13}C NMR ($CDCl_3$, ppm): δ 79.21, 70.58, 66.38, 66.12, 20.78. ^{31}P NMR ($CDCl_3$, ppm): δ 17.34. +ESI MS: calculated $[M+H]^+$ for $C_6H_9O_4P$: 177.0317, found: 177.0311.

2.3.4. General Procedure of Kinetic Study of Homopolymerization of BYP via ROP

In a glovebox, a solution of BYP (0.608 g, 3.45 mmol) and benzyl alcohol (7.37 mg, 0.0682 mmol) in anhydrous CH_2Cl_2 (0.6 mL) was transferred into a 5 mL shell vial with a stir bar. DBU (20.8 mg, 0.137 mmol) was injected into the mixture solution. 0.05 mL of samples were extracted at 2, 3, 5, 7, 9 and 10 min and quenched by addition of solution of benzoic acid in CH_2Cl_2. Conversion of monomer to polymer was calculated by ^{31}P NMR spectroscopy.

2.3.5. General Procedure of Kinetic Study of Second-block (PLLA) Polymerization via ROP

In a glovebox, a solution of BYP (0.504 g, 2.86 mmol) and benzyl alcohol (6.14 mg, 0.0568 mmol) in anhydrous CH_2Cl_2 (0.5 mL) was transferred into a 20 mL vial with a stir bar. DBU (17.3 mg, 0.114 mmol) was injected into the mixture solution. After stirring for 7 min of polymerization, a solution of LLA (409 mg, 2.86 mmol) in anhydrous CH_2Cl_2 (3.5 mL) was added into the mixture solution. Then, 0.1 mL of

samples were extracted at 0.5, 1, 1.5, 2, 2.5, 3, 3.5, and 4 min and quenched by addition of solution of benzoic acid in CH_2Cl_2. Conversion of monomer, LLA, to polymer was calculated by ^{1}H NMR spectroscopy.

2.3.6. One-pot Sequential Block Copolymerization of BYP and LLA, $PBYP_{49}$-b-$PLLA_{44}$

In a glovebox, a solution of BYP (3.02 g, 17.2 mmol) and benzyl alcohol (37.0 mg, 0.340 mmol) in anhydrous CH_2Cl_2 (3.0 mL) was transferred into a vial with a stir bar. DBU (104 mg, 0.682 mmol) was injected into the mixture solution. After stirring for 7 min, a solution of LLA (2.46 g, 17.0 mmol) in anhydrous CH_2Cl_2 (21 mL) was added into the mixture solution. After 4 min, the reaction was quenched by addition of solution of benzoic acid in CH_2Cl_2. The product was precipitated in diethyl ether three times and dried overnight in vacuum. 4.9787 g (97.6% yield). GPC: M_n = 21900 g/mol, PDI = 1.17. IR: 3350–3150, 3050–2850, 1757, 1456, 1271, 1211, 1184, 1130, 1074, 1009, 970, 804 cm^{-1}. ^{1}H NMR (CD_2Cl_2, ppm): δ 7.42–7.30 (m, 5H, aromatic ring), 5.16 (broad q, *J* = 7.2 Hz, 100H, ArC*H*$_2$OP and OCC*H*(O)CH$_3$), 4.34–4.22 (b, 196H, POC*H*$_2$C*H*$_2$O), 4.22–4.08 (b, 98H, POC*H*$_2$CH$_2$CCH), 2.67–2.56 (b, 98H, POCH$_2$C*H*$_2$CCH), 2.28-2.09 (b, 49H, OCH$_2$CH$_2$CC*H*), 1.55 (broad d, *J* = 7.2 Hz, 264H, C*H*$_3$CH(O)CO). ^{13}C NMR (CD_2Cl_2, ppm): δ 170.02, 130.07, 129.16, 128.57, 80.28, 71.00, 69.53, 67.00, 66.27, 21.06, 17.02. ^{31}P NMR (CD_2Cl_2, ppm): δ -1.60. DSC: (T_g) = -33.23 °C. TGA in N_2: 190-290 °C, 40% mass loss; 290–370 °C, 42% mass loss; 12% mass remaining above 370 °C.

2.3.7. Thiol-yne "Click" Reaction of PBYP Block of $PBYP_{49}$-b-$PLLA_{44}$ with 3-Mercaptopropionic Acid

A solution of block copolymer, $PBYP_{49}$-*b*-$PLLA_{44}$ (149 mg, 0.00990 mmol), 3-mercaptopropionic acid (524 mg, 4.93 mmol), and 2,2-dimethoxy-2-phenylacetophenone (215 mg, 0.840 mmol) in 7.5 mL of dimethyl sulfoxide was irradiated under UV irradiation (365 nm, 6 W) for 90 min while stirring. The reaction mixture was purified by precipitated in diethyl ether three times, dialyzed in nanopure water and freeze-dried overnight to give a white solid. (189 mg, 75.1% yield). IR: 3675–2760, 2700–2430, 1757, 1715, 1452, 1408, 1385, 1184, 1130, 1086, 1016, 982, 802, 754 cm^{-1}. ^{1}H NMR (DMSO, ppm): δ 13.2–11.9 (b, $SCH_2CH_2C(O)O\mathit{H}$), 7.44–7.26 (m, 5H, aromatic ring), 5.46 (d, *J* = 6.9 Hz, 2H, $OC\mathit{H_2}Ar$), 5.20 (broad q, *J* = 7.2 Hz, 88H, $OCC\mathit{H}(O)CH_3$), 4.35–3.80 (b, 294H, $POC\mathit{H_2}C\mathit{H_2}O$ and $POC\mathit{H_2}CH_2CH$), 3.00–2.80 (b, 196H, $SCH_2C\mathit{H_2}COOH$), 2.80–2.62 (b, 245H, $SC\mathit{H_2}CH_2COOH$ and $SC\mathit{H}(CH_2)CH_2CH_2$), 2.60–2.50 (b, 98H, $SC\mathit{H_2}CHS$), 2.25–2.05 and 1.85–1.57 (b, 98H, $POCH_2C\mathit{H_2}CH$), 1.46 (broad d, *J* = 7.2 Hz, 264H, $OCCH(O)C\mathit{H_3}$). ^{13}C NMR (DMSO, ppm): δ 173.05, 172.19, 169.27, 68.72, 66.25, 65.34, 44.05, 42.91, 41.67, 38.19, 37.54, 34.73, 34.18, 33.53, 29.71, 27.18, 26.09, 25.22, 16.53. ^{31}P NMR (DMSO, ppm): δ -1.19. DSC: (T_g) = 6.34 °C. TGA in N_2: 105–190 °C, 13% mass loss; 190–280 °C, 40% mass loss; 280–350 °C, 25% mass loss; 22% mass remaining above 350 °C.

2.3.8. Thiol-yne "Click" Reaction of PBYP Block of $PBYP_{49}$-b-$PLLA_{44}$ with 2-Aminoethanethiol

A solution of block copolymer, $PBYP_{49}$-*b*-$PLLA_{44}$ (150 mg, 0.0995 mmol), 2-aminoethanethiol (0.554 g, 4.88 mmol), and 2,2-Dimethoxy-2-phenylacetophenone (250 mg, 0.975 mmol) in 7.5 mL of dimethyl sulfoxide was irradiated under UV irradiation (365 nm, 6 W) for 90 min. The reaction mixture was purified by precipitated in diethyl ether four times, dialyzed in nanopure water at pH 3 and freeze-dried overnight to give a white solid. (220 mg, 83.8% yield). IR: 3600–3300, 3250–2470, 1755, 1604, 1454, 1250, 1184, 1084, 1013, 806, 754 cm^{-1}. ^{1}H NMR (DMSO, ppm): δ 8.60–7.95 (b, $SCH_2CH_2NH_3^+$), 7.46–7.42 (m, 5H, aromatic ring), 5.46 (d, *J* = 6.9, 2H, OCH_2Ar), 5.20 (broad q, *J* = 7.2 Hz, 88H, $OCCH(O)CH_3$), 4.40–3.85 (b, 294H, $POCH_2CH_2O$ and $POCH_2CH_2CH$), 3.45–3.33 (b, 196H, $SCH_2CH_2NH_3^+$), 3.20–2.75 (b, 343H, $SCH_2CHSCH_2CH_2NH_3^+$), 2.30–2.15 and 1.90–1.66 (b, 98H, $POCH_2CH_2CHS$), 1.46 (broad d, *J* = 7.2 Hz, 264H, $OCCH(O)CH_3$). ^{13}C NMR (DMSO, ppm): δ 169.21, 164.54, 68.69, 66.45, 65.16, 41.36, 36.96, 33.91, 33.39, 28.64, 26.79, 16.49. ^{31}P NMR (DMSO, ppm): δ -1.26. DSC: (T_g) = -7.49 °C. TGA in N_2: 190–350 °C, 74% mass loss; 26% mass remaining above 350 °C.

2.3.9. General Procedure for Self-assembly of Functional Diblock Copolymers

The functional anionic and cationic diblock copolymers (1.0 mg) were suspended into MOPS buffer (150 mM) at pH 7.4 and acetate buffer (150 mM) at pH 5.0.

2.4. Conclusions

In conclusion, a versatile platform for the construction of spherical micelles with different surface charges and functionalities based on fully degradable, hybrid diblock copolymer, PPE-*b*-PLLA, was developed. First, well-defined (PDI <1.2) diblock copolymers of alkyne-functional phospholanes and L-lactides were prepared by conducting rapid and facile one-pot sequential ROPs using an organocatalyst, DBU. The kinetic study of each block polymerization demonstrated an excellent controllability during ROP. Subsequently, photoinitiated, radical-mediated thiol-yne "click" chemistry was employed to convert the parental hydrophobic diblock copolymer into amphiphilic diblock polymers with different side-chain functionalities. Finally, the direct dissolution of the amphiphilic diblock copolymers in water promoted the formation of well-defined spherical nanoparticle assemblies with distinct negative and positive surface charges and uniform size distributions, as characterized by TEM, DLS, and zeta potential analyses. The fundamental understanding of degradability of these diblock copolymers and the application of nanoparticles in nanomedicine are currently under investigations.

CHAPTER III

PREPARATION AND *IN VITRO* ANTIMICROBIAL ACTIVITY OF SILVER-BEARING DEGRADABLE POLYMERIC NANOPARTICLES OF POLYPHOSPHOESTER-*BLOCK*-POLY(L-LACTIDE)*

3.1. Introduction

A slate of traditional antimicrobial agents has been employed for treatment of infectious diseases over the past decades. However, current therapeutic challenges include the rapid emergence of multidrug-resistant organisms, *e.g.*, Gram-positive pathogens, Gram-negative enteric bacteria, and *Mycobacterium tuberculosis*, and suboptimal pharmacokinetics and pharmacodynamics, *e.g.*, poor water solubility or lack of desired tissue distribution after systemic delivery.[1,2,64-66] Available strategies to address these barriers are limited, usually requiring administration of more frequent or higher doses of available, traditional agents, which in turn promotes end-organ toxicities and adverse effects.[3] Therefore, it is imperative to identify and develop new modalities of antimicrobial treatment to circumvent these challenges; current themes include

* Part of this work is reprinted with permission from "Preparation and *in Vitro* Antimicrobial Activity of Silver-bearing Nanoparticles of Degradable Diblock Copolymer, Polyphosphoester-*block*-Poly(L-lactide)" by Lim, Y. H., Tiemann, K., Heo, G. S., Wagers, P. O., Rezenom, Y. H., Zhang, S., Zhang, F., Youngs, Y. J., Hunstad, D. A., and Wooley, K. L., 2015, *ACS Nano*, 9 (2), 1995–2008. Copyright [2015] by the American Chemical Society.

candidate antivirulence therapies that will not engender bacterial resistance, as well as targeted delivery of antimicrobials to sites of infection in order to limit systemic effects.

Silver has been used as an antimicrobial agent since ancient times, due to its broad spectrum of activity against bacterial and fungal pathogens and relatively low toxicity to human tissues. Additionally, despite its widespread topical use, *e.g.*, in wound dressings and burn ointments, instances of bacterial resistance to the biocidal activity of silver are rare.[67-72] Significant efforts have been made to elucidate the antimicrobial activity of silver by employing various silver formulations, *e.g.*, polyamidoamine dendrimer-based silver complexes and nanocomposites by Balogh *et al.*;[73] two-component composites of cationic polymer, poly(4-vinyl-*N*-hexylpyridinium bromide), and silver bromide nanoparticles by Sen *et al.*;[74] hybrids of silver nanoparticles with polyethylenimine-based hyperbranched polymers by Mecking *et al.*,[75] *etc*.

Given the potential of these systems, our group has been developing silver-based antimicrobial delivery from two different perspectives: (1) improving the stability of the active moiety (silver cation, Ag^+), within an organometallic complex and (2) optimizing delivery of silver compounds to sites of epithelial infection by exploiting various nanoparticle templates. Youngs *et al*. designed a library of *N*-heterocyclic silver carbene complexes (SCCs), which improved the stability of Ag^+ to light and aqueous solution, allowed for the direct administration of silver-compounds *via* nebulization, and demonstrated the antimicrobial activity of Ag^+ against contemporary Gram-positive and Gram-negative pathogens.[76-84] In parallel, Cannon and Youngs *et al.* demonstrated

sustained silver release and potent *in vitro* and *in vivo* antimicrobial efficacy of SCC10-bearing L-tyrosine polyphosphate nanoparticles (LTP NPs) against the cystic fibrosis pathogen *Pseudomonas aeruginosa*.[85] Meanwhile, benefiting from polymeric backbone-structured building blocks with precisely controlled architectures, surface characteristics and supramolecular assembly,[9,10] Cannon, Youngs, and Wooley *et al.* highlighted the preparation of smaller particle size and the introduction of functionalities for attachment of targeting moieties by utilizing multifunctional shell cross-linked knedel-like polymeric nanoparticles (SCK NPs) of poly(acrylic acid)-*block*-polystyrene (PAA-*b*-PS).[86,87] However, in spite of promising *in vitro* data and *in vivo* therapeutic outcomes after treatment with SCK NPs bearing silver-based antimicrobials in prior studies, translational concerns remained regarding *in vivo* fate, clearance, accumulation and possible toxicity, immunogenicity and other side effects that may be elicited by the hydrocarbon backbone-based, nondegradable NPs while in mammalian hosts and persistent in the environment.[88]

To address this limitation, we have developed biocompatible and multifunctional polymeric nanoconstructs derived from biodegradable precursors, *e.g.*, polyphosphoesters, polycarbonates, polyesters, polypeptides, *etc*. for potential application in biomedical settings.[36,89-93] We have employed a combination of state-of-the-art polymerization chemistries, "click"-type postpolymerization chemical modification and supramolecular assembly with respect to the construction of complex and functional polymeric materials. This sequential chemical approach allows for synthetic versatility and fabrication of intricate polymeric nanoparticles for diverse

pharmaceutical applications.[39,94-99] To capture this combinatorial concept, we recently demonstrated the rapid and facile synthesis of amphiphilic diblock copolymers, composed of phosphoester backbones and both carboxylate and 1,2-dithioether side chain functionalities for interactions with silver.[100] Micellar assemblies comprised of these block copolymers were shown to address the issues of weak silver binding and nondegradability, however, they raised alternative concerns in having phosphoric acid and ethylene glycol as two of the degradation products. Therefore, in this current work, the hydrophobic portion of the polyphosphoester backbone is replaced by poly(L-lactide), a well-known and broadly applicable polymer that is derived from the natural product lactic acid. Amphiphilic block copolymers containing phosphoester repeat units that carry carboxylate and 1,2-dithioether functionalities along the hydrophilic segment and L-lactide repeat units along the hydrophobic segment were prepared by an efficient a one-pot sequential ring-opening polymerization followed by thiol-yne "click" reactions.[94] Subsequently, this "hybrid" polymer construct facilitated the formation of well-defined polymeric nanostructures with distinctive core-shell morphology and capable of high loading capacities for several antimicrobial silver species.

To develop potentially fully biodegradable, biocompatible polymeric NPs with the capability to deliver silver-based antimicrobials, we prepared a series of anionic dNPs from block copolymers having polyphosphoester (PPE) and poly(L-lactide) (PLLA) block segments, designed specifically for silver loading into the hydrophilic shell and/or the hydrophobic core. With the use of three different types of silver-based antimicrobials – silver acetate (AgOAc) or one of two silver carbene complexes (SCCs),

comparative studies of the selection of proper dNP templates for silver-loading and release were undertaken. Then, the comprehensive degradation studies, including evaluation of hydrolytic or enzymatic degradability and identification of the degradation products, were performed for the fundamental understanding of the developed dNPs as potential delivery carriers for silver-based antimicrobials. Finally, *in vitro* antimicrobial efficacy of the selected Ag-dNPs was compared with that of inherent silver compounds against 10 contemporary epidemic strains of *Staphylococcus aureus* and eight uropathogenic strains of *Escherichia coli.*

3.2. Results and Discussions

3.2.1. Rational Design of Polymer Structure and Compositions

In designing these polymer constructs as optimized delivery carriers, several criteria were considered, *i.e.,* degradability, biocompatibility, and functionality. Its susceptibility to hydrolytic and/or enzymatic degradation and loading of hydrophobic drugs make polylactide (PLA) popular as a building block for biomedical degradable polymers.[101,102] However, a lack of chemical functionality and intrinsic hydrophobicity limit its use as an intelligent delivery carrier itself. To overcome this limitation, we envisioned that incorporating PPE, well-known to be biodegradable and composed of fairly hydrophilic phosphotriester linkages,[56,89,103] with PLA would compensate the limitations inherent to PLA alone, while also diluting the potential side effects of phosphoric acid and ethylene glycol degradation products. Furthermore, the facile introduction of pendent side functional groups on the pentavalent phosphorus atom would maximize their potential as functional delivery carriers. For instance, in this

study, 1,2-dithioether and carboxylic acid side chain moieties would represent sites for silver cation loading, with the carboxylic acids also offering opportunities for conjugation with tissue-specific targeting peptides or proteins. Loading of hydrophilic and/or hydrophobic silver agents within the developed single particle template would be feasible. In addition, we postulated that nanoparticles with different hydrophilic chain lengths, *i.e.*, different dimensions of interaction sites for silver cations, may influence the silver-loading capacity of nanoparticles and, consequently, the therapeutic effects of silver-loaded nanoparticles against *in vitro* bacterial strains.

3.2.2. Preparation of Functional, Degradable Polymeric Nanoparticles

For the comparative study, each of three amphiphilic diblock copolymers with different hydrophilic PPE chain length, anionic polyphosphoester-*block*-poly(L-lactide) ($aPPE_n$-*b*-$PLLA_{50}$, n = 50, 90 or 210), **2**, was synthesized by one-pot sequential ring-opening polymerizations (ROP) of alkyne-functionalized cyclic phosphotriester and L-lactide followed by thiol-yne "click" reactions to introduce functionalities for interaction with Ag^+ and also to impart hydrophilicity to the PPE block segment (Figure 3.1.).[94] Well-defined structures of **1** were confirmed by gel permeation chromatography analysis, with monomodal molecular weight distributions having PDI <1.26. In addition, in all three precursor polymers, one distinct ^{31}P NMR resonance at *ca*. –1.0 ppm revealed the stability of the degradable PPE backbone during the ROPs and the work-up process of **2**.

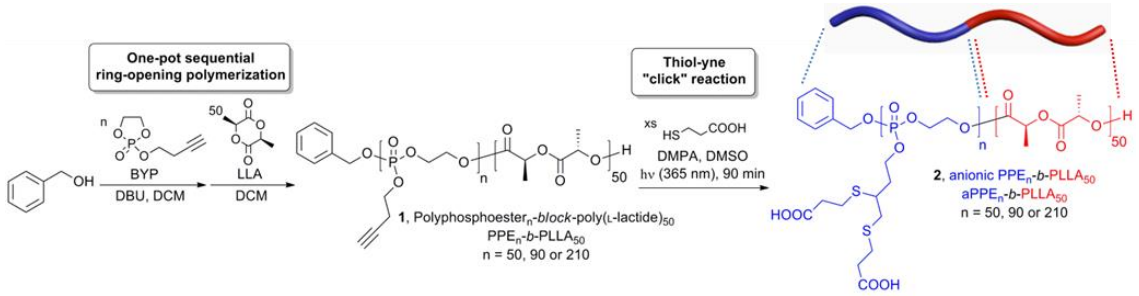

Figure 3.1. Synthetic route for the preparation of alkyne-functionalized diblock copolymer of phosphoester and L-lactide, PPE-*b*-PLLA, 1, by one-pot sequential ROP, followed by postpolymerization modification *via* thiol-yne "Click" reaction using 3-mercaptopropionic acid to prepare anionic amphiphilic diblock copolymer, aPPE-*b*-PLLA, 2.

The self-assembly behaviors of the three individual polymers of aPPE$_n$-*b*-PLLA$_{50}$, **2** (n = 50, 90 or 210 for **2a**, **2b**, or **2c**, respectively), were studied by direct dissolution in nanopure water (Figure 3.2.). The dimensions and surface charges of the resulting dNPs, **3** (n = 50, 90, or 210 for **3a**, **3b**, or **3c**, respectively), were characterized by transmission electron microscopy, dynamic light scattering (DLS), atomic force microscopy (AFM) and electrophoretic light scattering, respectively. While DLS analyses of **3a** and **3b** indicated number-average hydrodynamic diameters ($D_{h(number)}$) of 25 and 34 nm, respectively, with monomodal size distributions (PDI <0.13), **3c** featured the smallest $D_{h(number)}$ of 13 nm, with a broad distribution (PDI = 0.40) (Figure 3.3.). The inherently hydrophilic **3c** displayed higher critical micelle concentration, *ca.* 0.5 mg/mL, owing to its long hydrophilic chain, compared with *ca.* 0.2 mg/mL of **3a** and *ca.* 0.3 mg/mL of **3b**. Meanwhile, as predicted, these three different **3** micellar formulations in aqueous solutions indicated negative surface charges, having ζ-potential values of –17 to –47 mV at pH 5.0 or 7.4, as measured by electrophoretic light scattering (Table 3.1.).

Also, well-defined **3** assemblies were observed by TEM with comparable sizes and size distributions as observed by DLS (Figure 3.7.).

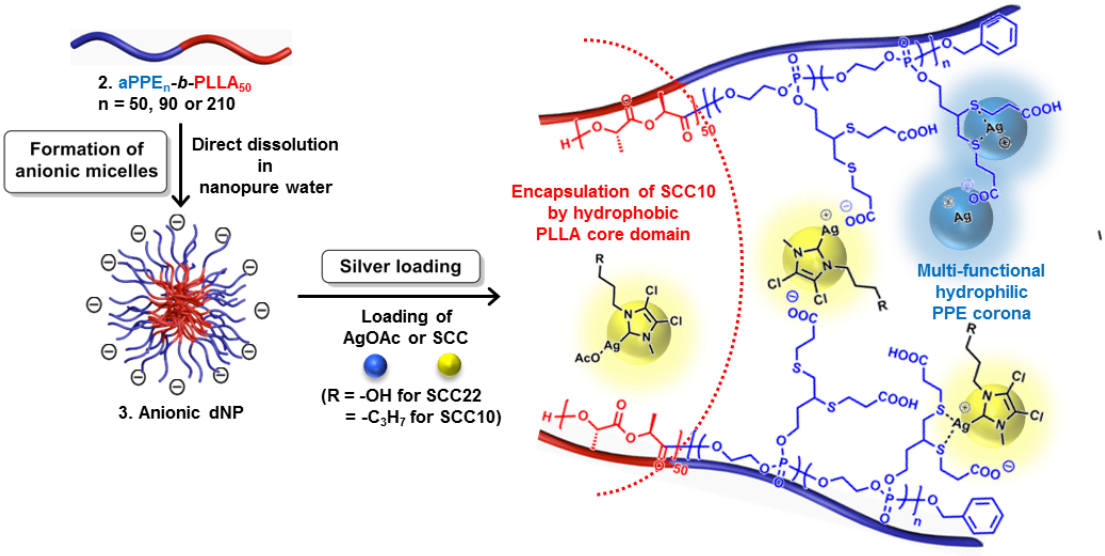

Figure 3.2. Schematic illustration of the self-assembly of 2a–2c into anionic micelles, 3a–3c, by direct dissolution in water followed by silver loading. Schematic representation of silver cation, Ag^+, (blue ball) from AgOAc and SCC22 or SCC10 (yellow ball) chelated into the corona or incorporated into the core of 3, Prepared from 2. (Note: the placements of the silver species within the dNP framework are proposed locations that have not been confirmed experimentally.)

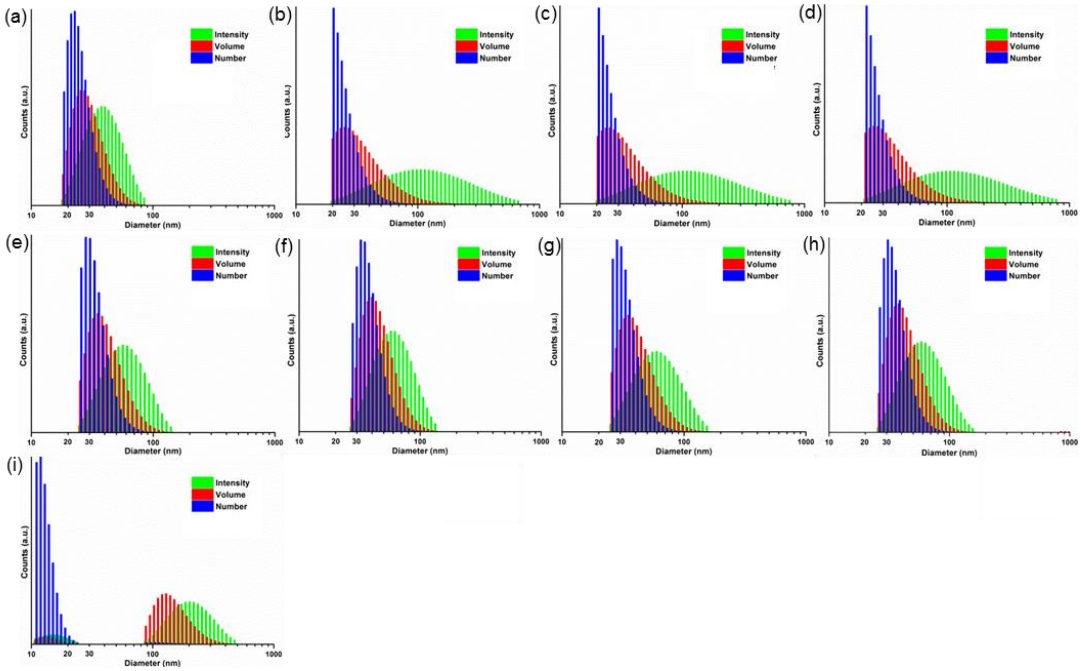

Figure 3.3. Dynamic light scattering histograms. Average values from 10 measurements, with standard deviations calculated as the breadth of the distributions. Green bars: $D_{h(intensity)}$, red bars: $D_{h(volume)}$ and blue bars: $D_{h(number)}$. Top row: (a) naked 3a, (b) AgOAc-3a, (c) SCC22-3a, and (d) SCC10-3a. Middle row: (e) naked 3b, (f) AgOAc-3b, (g) SCC22-3b, and (h) SCC10-3b. Bottom row: (i) naked 3c.

Table 3.1. Summary of characterization data from naked nanoparticles of aPPE-*b*-PLLA, 3, as measured by TEM, DLS, AFM, and electrophoretic light scattering.

Type of NPs	TEM (nm)	$D_{h(intensity)}$ (nm)	$D_{h(volume)}$ (nm)	$D_{h(number)}$ (nm)	PDI	AFM (nm)	ζ-potential (mV)
3a	18 ± 3	41 ± 14	31 ± 10	25 ± 6	0.11	38 ± 5	-26 (pH 7.4) -17 (pH 5.0)
3b	31 ± 4	63 ± 24	43 ± 15	34 ± 9	0.13	65 ± 11	-47 (pH 7.4) -39 (pH 5.0)
3c	27 ± 6	223 ± 83	153 ± 53	13 ± 2	0.40	73 ± 18	-37 (pH 7.4) -32 (pH 5.0)

In contrast to the good agreement between hydrodynamic and dry-state diameters as measured by DLS and TEM, respectively, AFM indicated significant deformation of **3** upon deposition and drying on the mica substrate (Figure 3.4.). The range of *ca.* 4–9 nm in height and *ca.* 38–73 nm in diameter indicated flattening of **3**, which was anticipated based upon the presence of low T_g fluid-like shell components, *i.e.*, the PPE block segment and some degree of mixing of the shell and core components, as supported by the observation of a single T_g value for each block copolymer sample. Further quantitative analysis by AFM is complicated by the presence of substantial amounts of polymer debris and agglomerations of **3** across the substrate, which is also indicative of the fluidity of the nanoparticle assemblies.

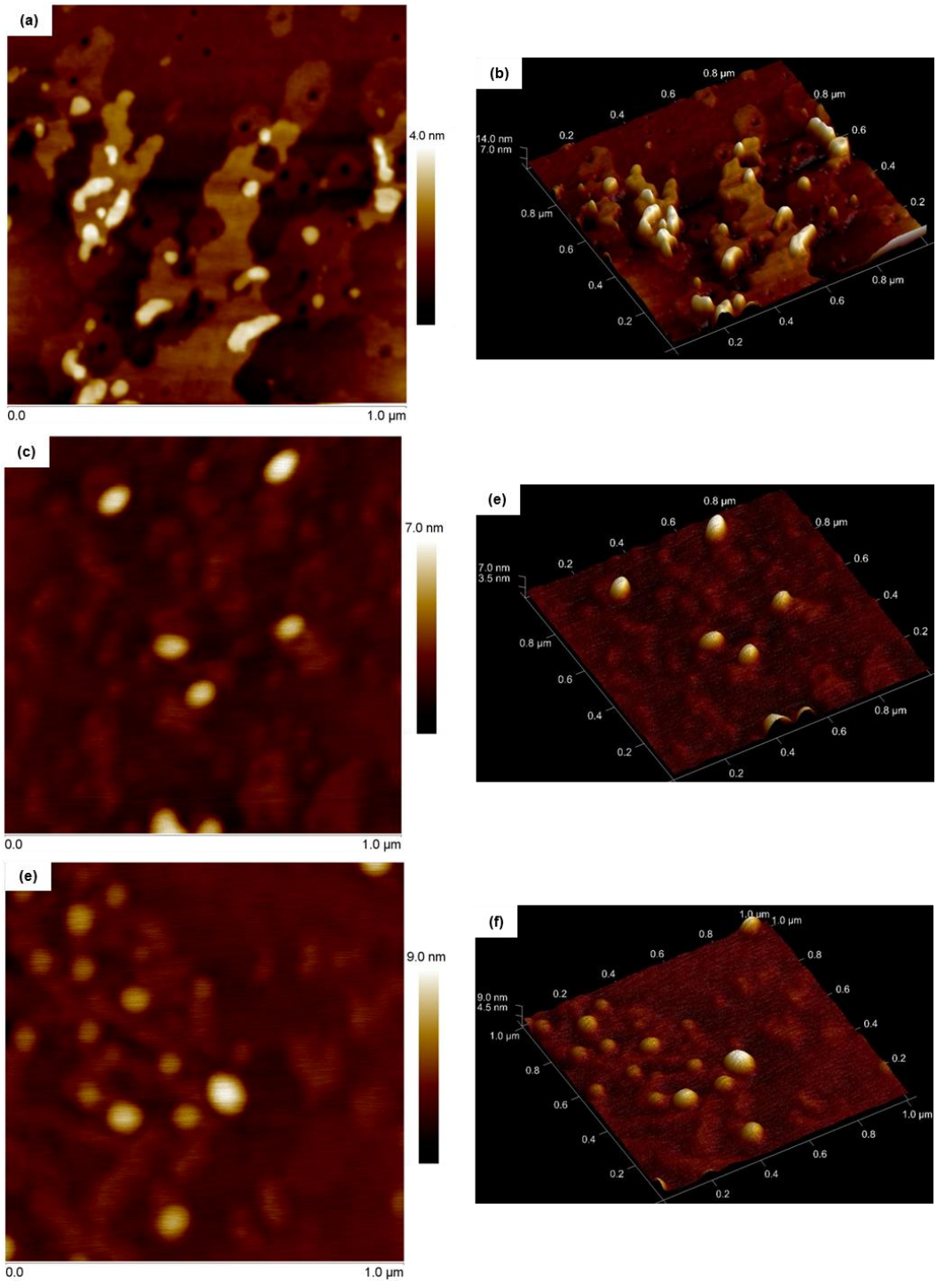

Figure 3.4. AFM height and three-dimensional images of (a) and (b) 3a: height = *ca.* 4 nm and D_{av} = 38 ± 5 nm, (c) and (d) 3b: height = *ca.* 7 nm and D_{av} = 65 ± 11 nm, and (e) and (f) 3c: height = *ca.* 9 nm and D_{av} = 73 ± 18 nm, respectively, after counting more than 50 nanoparticles.

3.2.3. Preparation and Characterization of Silver-Loaded Degradable Polymeric Nanoparticles

We intended to load three different silver-based compounds, *i.e.*, from silver acetate (AgOAc), 1-methyl-3-(3-hydroxypropyl)-4,5-dichloroimidazol-2-ylidene silver (I) acetate (SCC22), or 1-methyl-3-hexyl-4,5-dichloroimidazole-2-ylidene silver (I) acetate (SCC10), into **3** by three different loading mechanisms as follows: (1) electrostatic interaction with carboxylate groups within the hydrophilic corona; (2) coordination with the two sulfur atoms of the 1,2-dithioether moieties on the side chains of the PPE block segment; and (3) encapsulation by hydrophobic interactions with the hydrophobic PLLA core of the nanoparticle (Figure 3.2.). Accordingly, we hypothesized that manipulation of the hydrophilic block length of **3** would influence the degree of silver-loading capacity due to the different physical dimensions of the resulting **3a-c** assemblies. Furthermore, it was expected that the silver-loading site, *i.e.*, shell or core, might influence the release kinetics of payloads or the antimicrobial therapeutic efficacy of silvers that are loaded *via* different loading mechanisms.

The silver-loading capacities of **3a** and **3b**, selected due to their monomodal size distributions on DLS measurement, were analyzed by inductively coupled plasma-mass spectrometry (ICP-MS) using Rh as an internal standard. Due to an ill-defined morphology, **3c** was excluded from silver loading studies. Overall, the loading capacity, measured as the weight percentage of silver loaded *vs.* polymers used to form the dNPs, was dependent on the feed amount (Figure 3.5. and Table 3.2.). For instance, AgOAc-**3b** reached *ca*. 8.6 wt% of silver loading capacity at the highest feed of AgOAc (40 wt%

with respect to the mass of polymer), as compared to *ca*. 3.2 wt% at 10 wt% feed amount. Similarly, with 100 wt% feed of SCC22 or SCC10, *ca.* 11 wt% loading capacities were observed for **3b**, which were about twice higher than when loaded at 50 wt% feed amount. There was no significant correlation between hydrophilic block length and silver-loading capacity with the two water-soluble silver compounds, AgOAc and SCC22. On the basis of observations of the occurrence of precipitates or no improvement of silver loading upon feeds higher than 40 or 100 wt% of AgOAc or SCCs, respectively, and overall insignificant difference in loading % (*ca.* <5% in all cases) between **3a** and **3b** at 40 or 100 wt% of AgOAc or SCC22, respectively, those dNPs appeared to be already saturated with silver compounds regardless of the length of hydrophilic PPE block segment. Meanwhile, differences in the loading efficiencies, measured as the ratio of silver loaded into the dNPs to the amount of silver in the feed, between **3a** and **3b** were insignificant. Once the free silver compounds were washed away (Figure 3.11.), each silver-loaded micellar nanoparticle sample was lyophilizable and redispersible in nanopure water for experimental use.

As characterized by DLS and TEM, Ag-**3a** and Ag-**3b**, each loaded by AgOAc, SCC22 or SCC10, were found to be uniform nanostructures of size and shape that agreed with the naked **3a** and **3b**, respectively, indicating that the incorporation of silver compounds did not affect the dimensions and morphology of the parent micellar assemblies (Figure 3.6., Figure 3.7. and Table 3.3.). DLS analysis of Ag-**3a** and Ag-**3b** indicated $D_{h(number)}$ of *ca*. 27 and 35 nm in average, respectively, with narrow and monomodal size distributions (PDI <0.26). Also, size and size distributions of silver-

bearing micellar nanoparticles**,** as observed by TEM, were comparable to those observed by DLS.

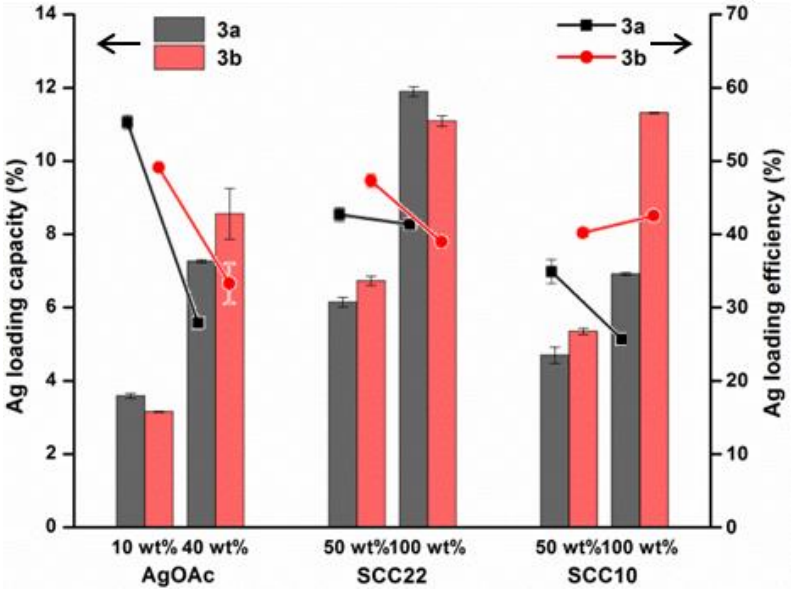

Figure 3.5. Ag-loading capacities (%) (left axis; bars) and efficiencies (%) (right axis; lines and symbols) of AgOAc-3a, AgOAc-3b, SCC22-3a, SCC22-3b, SCC10-3a or SCC10-3b with varying silver feed (*i.e.*, 10 and 40% (w/w) of AgOAc or 50 and 100% (w/w) of SCC22 and SCC10 with respect to the mass of the polymers in the NP solutions). (Average values were calculated from triplicate experiments.)

Table 3.2. Silver-loading capacity (%) and efficiency (%) of 3a and 3b with three different types of silver compounds (AgOAc, SCC22 and SCC10). (Average values were calculated from triplicate.)

		AgOAc						SCC22					SCC10				
		1 (%)	2 (%)	3 (%)	Avg.[a] (%)	Eff.[b] (%)		1 (%)	2 (%)	3 (%)	Avg. (%)	Eff. (%)	1 (%)	2 (%)	3 (%)	Avg. (%)	Eff. (%)
3a	10 wt%	3.52	3.63	3.63	3.59 ± 0.06	55.6 ± 0.95	50 wt%	6.00	6.27	6.16	6.14 ± 0.13	42.9 ± 0.94	4.45	4.88	4.77	4.70 ± 0.22	35.1 ± 1.66
	40 wt%	7.23	7.31	7.25	7.26 ± 0.04	28.1 ± 0.16	100 wt%	11.8	12.0	11.9	11.9 ± 0.13	41.6 ± 0.47	6.91	6.96	6.88	6.92 ± 0.04	25.8 ± 0.15
3b	10 wt%	3.15	3.17	3.15	3.16 ± 0.02	48.8 ± 0.23	50 wt%	6.83	6.77	6.59	6.73 ± 0.13	47.0 ± 0.88	5.41	5.39	5.25	5.35 ± 0.09	40.0 ± 0.64
	40 wt%	8.21	8.11	9.36	8.56 ± 0.69	33.1 ± 2.69	100 wt%	10.9	11.1	11.2	11.1 ± 0.14	38.8 ± 0.49	11.3	11.3	11.3	11.3 ± 0.02	42.3 ± 0.06

[a]Silver loading capacity, measured as the weight percentage of silver loaded *vs.* polymers used to form the dNPs. (The final results were obtained from triplicate.)

[b]Silver loading efficiencies, measured as the ratio of silver loaded into the dNPs to the amount of silver in the feed. (The final results were obtained from triplicate.)

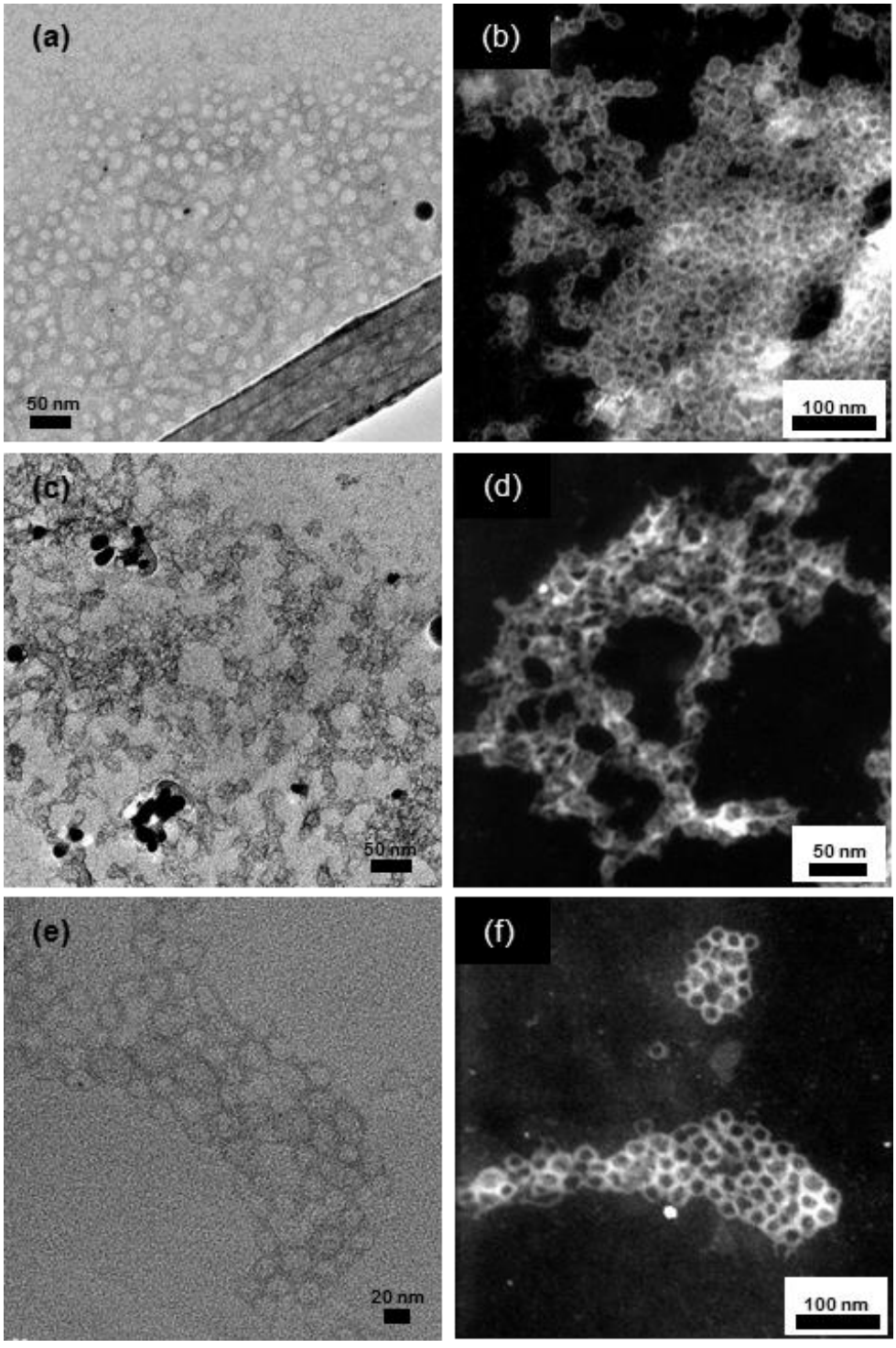

Figure 3.6. (a, c, and e) TEM bright-field and (b, d, and f) STEM dark-field images (drop deposited on carbon-coated copper grids with no stain) of AgOAc-3b, SCC22-3b, and SCC10-3b.

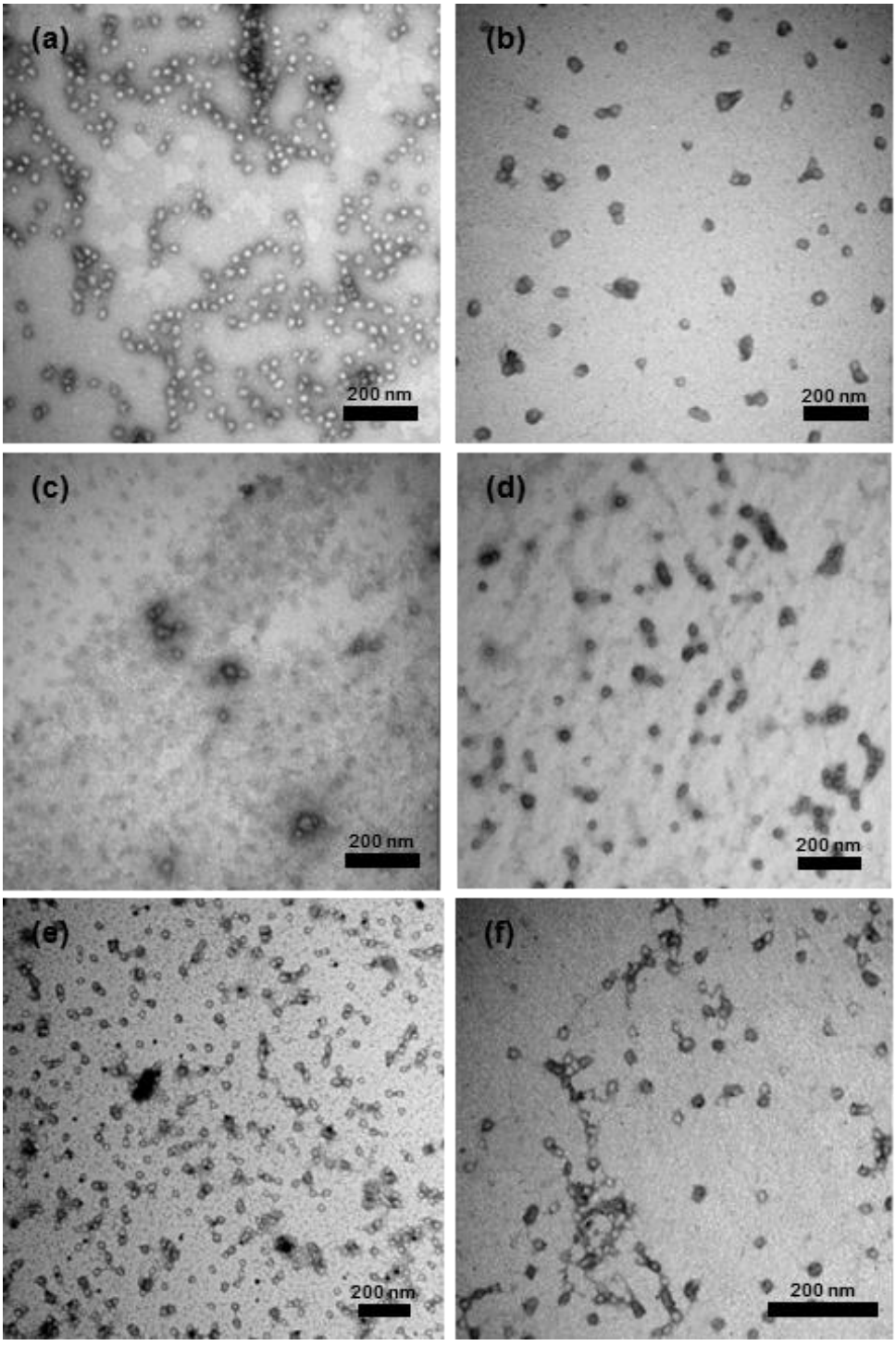

Figure 3.7. TEM images (drop deposited on carbon-coated copper grids and stained negatively with 1% (w/v) aqueous uranyl acetate) of (a) naked 3a, (b) naked 3b, (c) naked 3c, (d) AgOAc-3b, (e) SCC22-3b, and (f) SCC10-3b.

Table 3.3. Summary of characterization data from silver-loaded 3a and 3b, as measured by TEM and DLS.

Composition of NPs	TEM (nm)	$D_{h(intensity)}$ (nm)	$D_{h(volume)}$ (nm)	$D_{h(number)}$ (nm)	PDI
AgOAc-**3a**	n/a	152 ± 123	39 ± 24	26 ± 8	0.18
SCC22-**3a**	n/a	162 ± 137	39 ± 24	27 ± 8	0.23
SCC10-**3a**	n/a	166 ± 143	41 ± 24	28 ± 8	0.26
AgOAc-**3b**	27 ± 3	65 ± 22	47 ± 15	38 ± 9	0.09
SCC22-**3b**	26 ± 3	67 ± 27	43 ± 16	34 ± 9	0.11
SCC10-**3b**	24 ± 5	66 ± 26	45 ± 16	36 ± 9	0.08

In addition to the quantitative analysis of silver amounts by using ICP-MS, we made an attempt to observe contrast enhancement of Ag-**3b** by using bright-field TEM and dark-field scanning transmission electron microscopy (STEM) on unstained Ag-**3b** in order to demonstrate the presence of silver within **3b** (Figure 3.6.). The detection in the bright-field TEM images of Ag-**3b** and the dark-field STEM images of distinct illumination of silver from Ag-**3b** provided strong evidence of incorporation of silver within **3b**. It is noteworthy that these (S)TEM samples were not stained. Interestingly, hydrophobic Ag-compounds, SCC10, appeared to be located at the interface of the corona and core of **3b** in the dark-field STEM image. In each case, some elemental silver particles were detected, which may reflect reduction of Ag^{+} to Ag^{0} during the silver loading or TEM sample preparation processes. For instance, as illustrated in

Figure 3.6., Figure 3.8. and Figure 3.9., Ag^0 nanoparticles with metallic Ag lattice spacing of 2.36 nm from $d_{Ag(111)}$ and/or 2.05 nm from $d_{Ag(200)}$ were observed on the surface or inside the core of Ag-**3b**. Finally, the energy-dispersive X-ray spectroscopy (EDX) profile strongly confirmed the presence of silver atoms in the Ag-**3b** sample along with other abundant atoms such as phosphorus, sulfur, oxygen and carbon (Figure 3.8.).

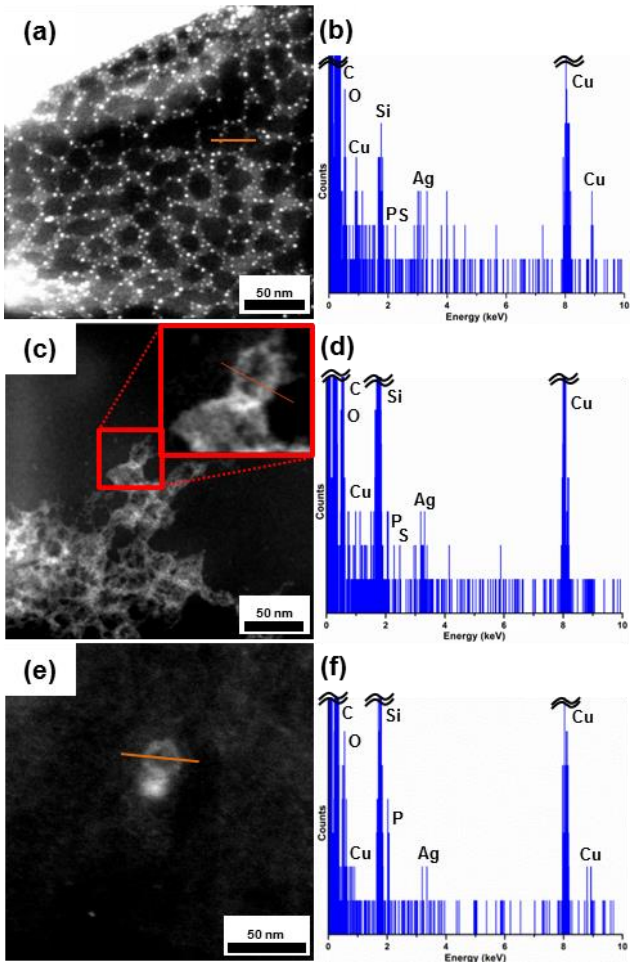

Figure 3.8. STEM dark-field images (drop deposition on carbon-coated copper grids with no stain) and EDX spectrum profile analysis of AgOAc-3b ((a) and (b), respectively), SCC22- 3b ((c) and (d), respectively) and SCC10-3b ((e) and (f)), respectively).

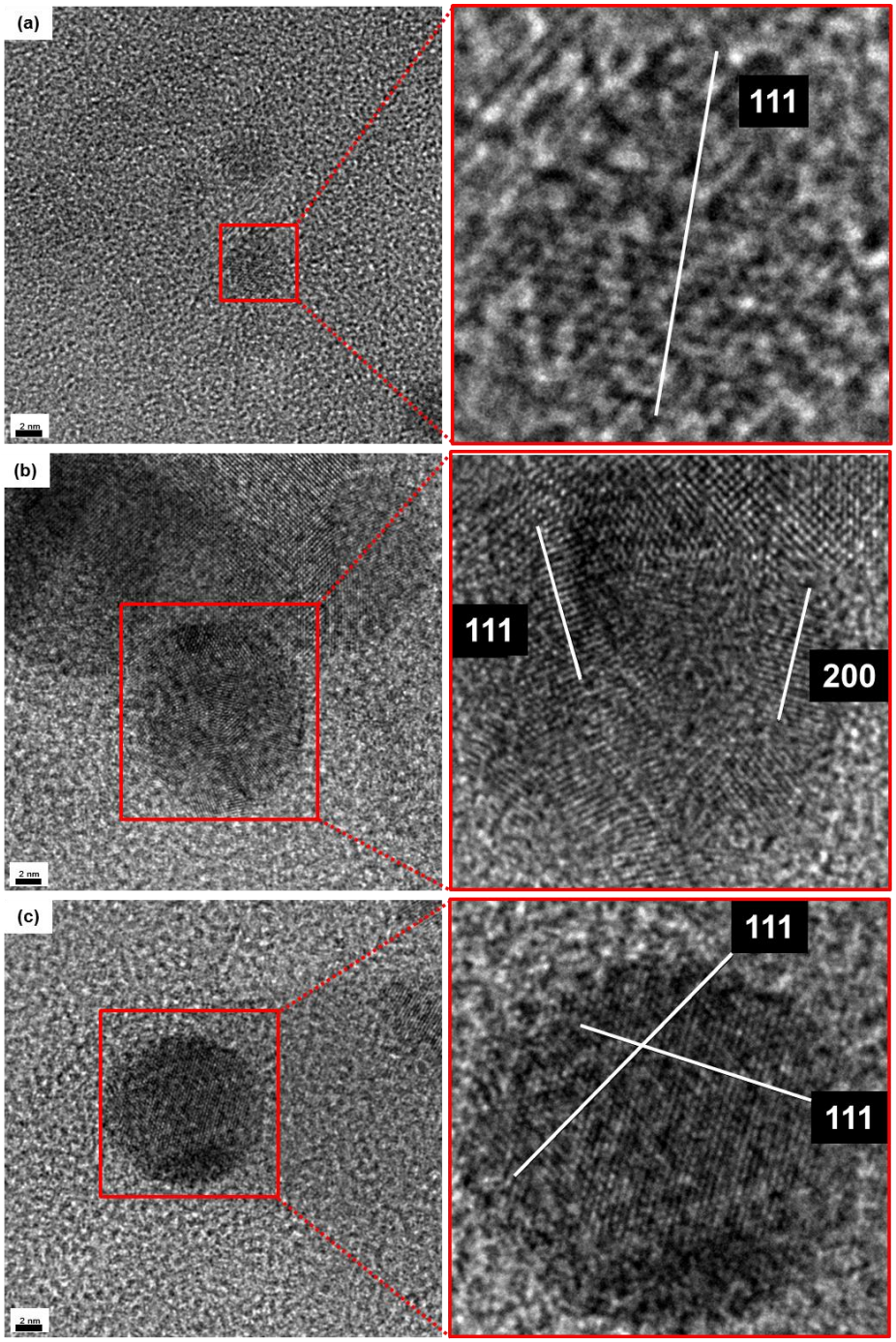

Figure 3.9. High-resolution TEM images with elemental silver particles, found with (a) AgOAc-3b, (b) SCC22-3b, and (c) SCC10-3b, which were measured to have metallic Ag lattice spacing = 2.36 ($d_{Ag(111)}$) or 2.05 Å ($d_{Ag(200)}$). (For clarity, isolated elemental Ag^0 particles were selected to identify their lattice spacing.)

3.2.4. Study of Silver-Release Kinetics

Based on the silver loading results, four representative silver-loaded micellar samples showing the highest loading capacities were selected for evaluation of release kinetics. We measured [Ag] by ICP-MS in serial samples from dialysis cassettes in nanopure water at 37 ºC (Figure 3.10. and Table 3.4.). Overall, the release kinetics of all of four formulations reached a plateau with almost complete silver release by *ca*. day 3. In control studies, rapid and nearly complete (> 99%) release of silver occurred for the silver compounds, *i.e.,* AgOAc, SCC22 or SCC10, from dialysis cassettes in nanopure water within 1 hour in the absence of dNPs, demonstrating the packaging and extended release of the silver species from the dNP constructs. Core-encapsulated SCC10 was released slightly more slowly, with time to 50% release *ca.* 5.5 h, than shell-loaded AgOAc or SCC22, *ca*. 2.5–3.5 h. Similarly, 75% release of SCC10 was achieved at *ca.* 17.5 h, slower than that of AgOAc and SCC22, *i.e.*, within *ca.* 9.5–12 h, likely due to their greater aqueous phase exposure throughout the shell and on the surface of the particle than those entrapped in the core. The fast release behavior of the present dNP-based antimicrobial system could be beneficial for direct epithelial treatment and/or prevention of ubiquitous bacterial infections, including those of the skin and urinary tract. Importantly, Ag-dNP complexes demonstrated a distinct advantage in preventing the reduction of silver, which was typically observed in aqueous solutions of the small molecule silver species within 1 day.

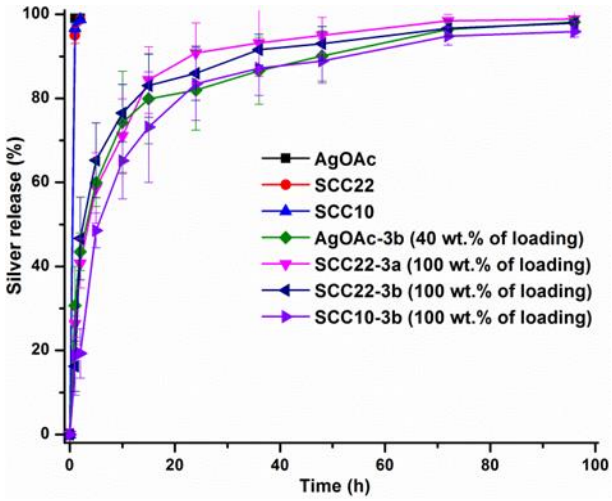

Figure 3.10. Release profiles of silver from dialysis cassettes containing solutions of silver compounds (AgOAc, SCC22 or SCC10) or silver-loaded 3a and 3b at 37 °C in nanopure water. (Averages were calculated from triplicate experiments.)

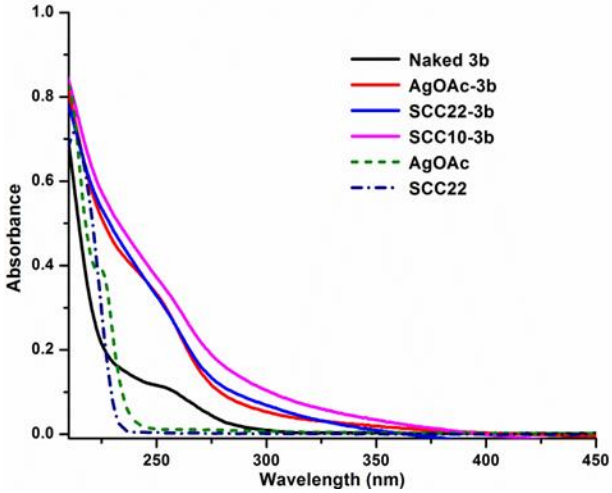

Figure 3.11. UV-vis spectra of control samples (naked 3b, AgOAc, and SCC22) and silver-loaded 3b after purification by centricon centrifugal filtration. The observance of no signals between 380–440 nm confirmed the absence of large silver particles (*ca*. >10 nm).

Table 3.4. Analysis of Ag-release kinetics from Ag-loaded 3a and 3b at 37 °C in nanopure water (conducted in triplicate).

	Ag-loading % (w/w) at t=0	Time		Maximum release %
		50% release	75% release	
SCC22-**3a** (100 wt% loading)	12.3%	3.5 h	12 h	98.9%
AgOAc-**3b** (40 wt% loading)	9.6%	3.5 h	11 h	98.2%
SCC22-**3b** (100 wt% loading)	11.6%	2.5 h	9.5 h	97.9%
SCC10-**3b** (100 wt% loading)	10.5%	5.5 h	17.5 h	95.9%

3.2.5. Degradation Studies

In this study, we assessed the stability of hydrolytically degradable nanoparticles in two different pH buffer solutions, 5.0 and 7.4, at 37 °C by monitoring the changes in hydrodynamic diameters (D_h) and surface charges of **3b** by DLS and by ζ-potential measurements, respectively (Figure 3.12.). The collected hydrolytic degradation products were then analyzed by using ^{31}P NMR spectroscopy and structurally identified by using electrospray ionization mass spectrometry (ESI MS). Furthermore,

electrostatic interaction-dependent enzymatic degradation behavior of **3b** was also investigated by using a lactate assay.

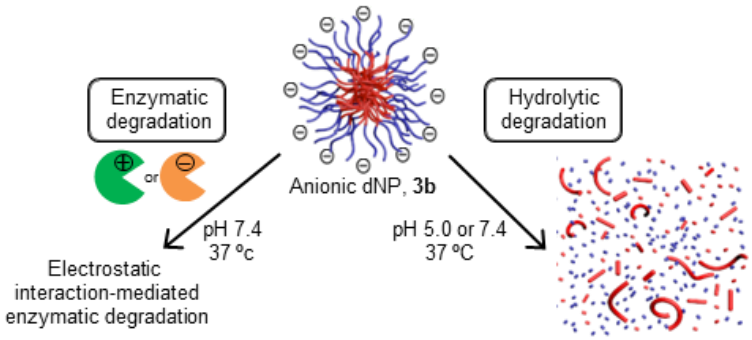

Figure 3.12. Synthetic illustration of enzymatic (left) or hydrolytic (right) degradation of 3b.

3.2.5.1. Hydrolytic Degradation of the dNP Constructs

The phosphoester linkage of PPEs or ester linkages of polylactides (PLAs) can be cleaved by spontaneous hydrolysis and/or enzymatic degradation.[95,101,104-106] We hypothesized that the faster hydrolysis of phosphoester linkages of PPE, compared with that of ester linkages of PLLA, would decrease the ratio of hydrophilicity/hydrophobicity, exposing hydrophobic surface patches and resulting in the precipitation of dNPs as the hydrolytic degradation proceeded (Figure 3.12.). Thus, aqueous buffer solutions of **3b** at pH 5.0 or 7.4 were incubated at 37 °C, and degradation profiles were assessed by measuring changes in D_h by DLS for up to 30 days (Figure 3.13.). As shown in Figure 3.13., there was an apparent decrease in D_h with time, which might be due to hydrolytic degradation of portions of the PPE shell chains. However, the degradation was complicated by macroscopic precipitation events. Overall, the dNP

assemblies in pH 5.0 and 7.4 aqueous solutions became unstable within about 2 weeks at 37 °C. In accordance with our prediction, the dNP solutions began to form visible precipitates gradually as time proceeded. After 2 weeks of incubation, a low intensity of scattered light prevented dNP detection, as measured by DLS. Meanwhile, there was no significant change in the ζ-potential values of **3b** at pH 5.0 or pH 7.4 over this time period (Figure 3.14.). Finally, in agreement with our hypothesis of backbone hydrolysis of the PPE block segment, there was a distinct shift in the ^{31}P resonance frequency from –0.02 ppm for intact **3b** to 1.01 ppm for its degradation products, *i.e.*, phosphoric acid (Figure S15).

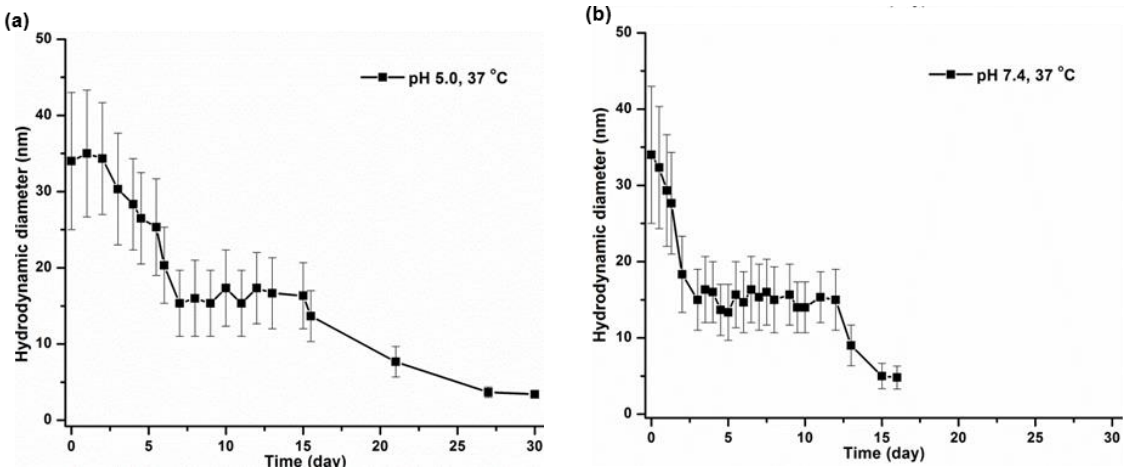

Figure 3.13. Study of dNP stability by using DLS. Changes in the hydrodynamic diameter (nm) of nanoparticles, 3b, at pH 5.0 (a) or pH 7.4 (b) at 37 °C over time. The average values from 10 measurements, with the standard deviations calculated as the breadth of the distributions, are shown.

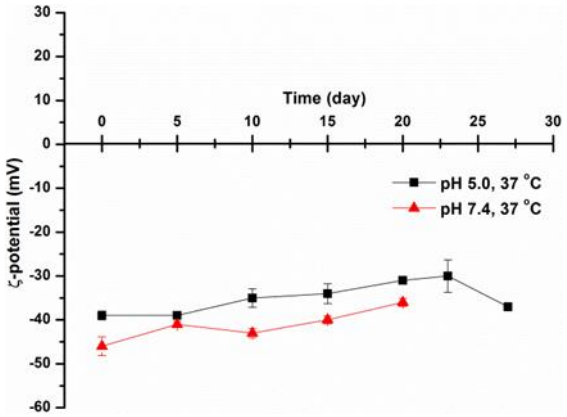

Figure 3.14. Changes in ζ-potentials for 3b at pH 5.0 (black) or pH 7.4 (red) at 37 °C over time.

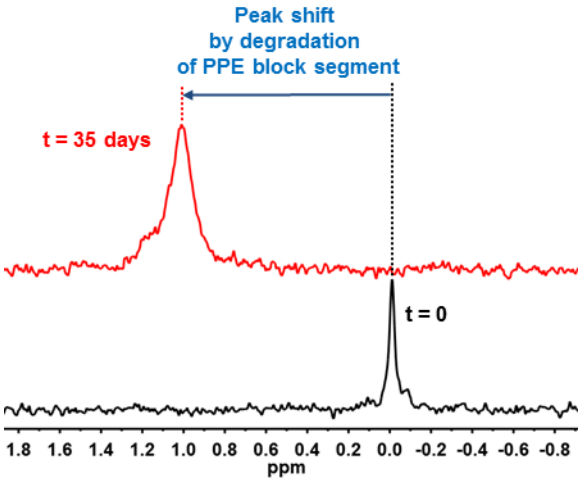

Figure 3.15. Changes of the ^{31}P NMR resonance of PPE backbone of 3b at t=0 (black) (a) and t = 35 days (b) at pH 7.4 at 37 °C.

3.2.5.2. Identification of the Degradation Products of 3b by ESI Mass Spectrometry.

Previously, we reported identification of the hydrolytic degradation products of nanoparticles of poly(ethylene glycol)-*block*-polyphosphoester, a partially degradable diblock copolymer, by ESI MS.[95] In the present study, we identified the degradation products from our fully degradable diblock copolymer system **3b** by employing the same

analytical approach. Solutions of **3b** in D_2O were incubated at 37 °C for 35 days, at which time they were not detectable by DLS and the ^{31}P resonance signal from the intact PPE backbone had disappeared in ^{31}P NMR spectra. Given our hydrolytic degradation data, we postulated that the PPE block segment primarily becomes hydrolyzed into small molecules, *i.e.,* variants of phosphoric acids along with side-chain moieties, while the more rigid ester backbone-based PLLA block segment would be converted into a mixture of oligomers and partially fragmented polymers of lactide. Indeed, in the *m/z* region below 400, the presence of derivatives of phosphoric acids (**e** in Figure 3.16.) and side chain moieties (**j** in Figure 3.16.) was confirmed by ESI MS, supporting our model of hydrolytic degradability of phosphotriester linkages of PPE. A number of unexpected molecular derivatives, generated by fragmentation during ESI MS measurements, were also identified by using tandem mass spectrometry (Figure 3.17.). Of note, ethylene glycol was not demonstrable as one of the degradation products, as it is not ionized in the electrospray instrument. In addition to the presence of the unimer and dimer of lactic acid (**a** and **f** in Figure 3.16., respectively) in the *m/z* region below 400, a series of fragments of PLLA block segments were detected, *i.e.,* oligomers and polymers with repeat units up to 26, with monomodal distribution of *m/z* at intervals of 72 Da, corresponding to a single PLLA repeat unit. No molecules were detected above *m/z* 2000 by ESI or by matrix-assisted laser desorption/ionization time-of-flight (MALDI-TOF) mass spectrometry.

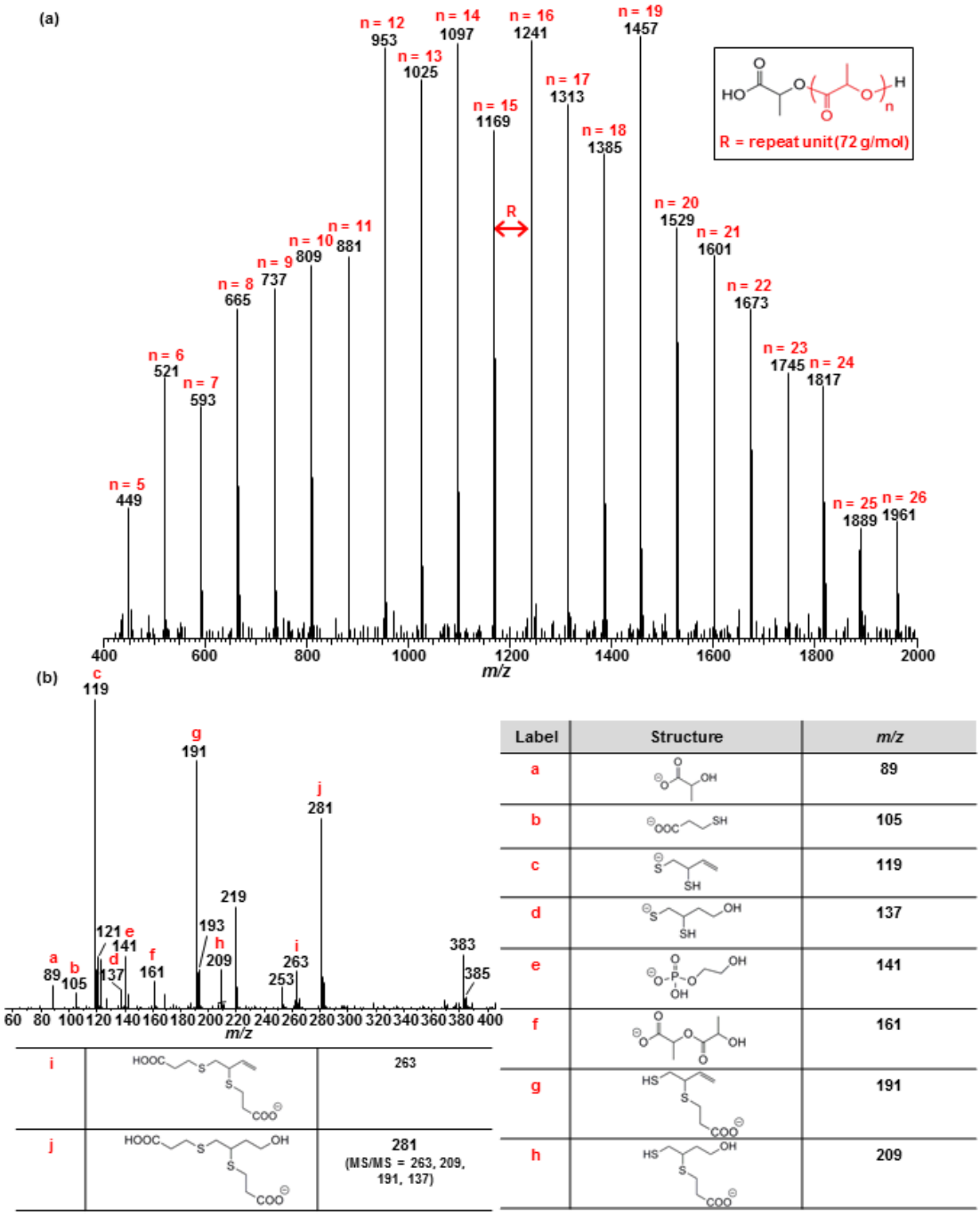

Label	Structure	*m/z*
a		89
b		105
c		119
d		137
e		141
f		161
g		191
h		209

i		263
j		281 (MS/MS = 263, 209, 191, 137)

Figure 3.16. ESI MS analysis of the degradation products of nanoparticles, 3b. Mass spectra in negative ion mode; *m/z* range of 400–2000 (a) and 50–400 (b). See Figure 3.17. for the MS/MS spectrum of j.

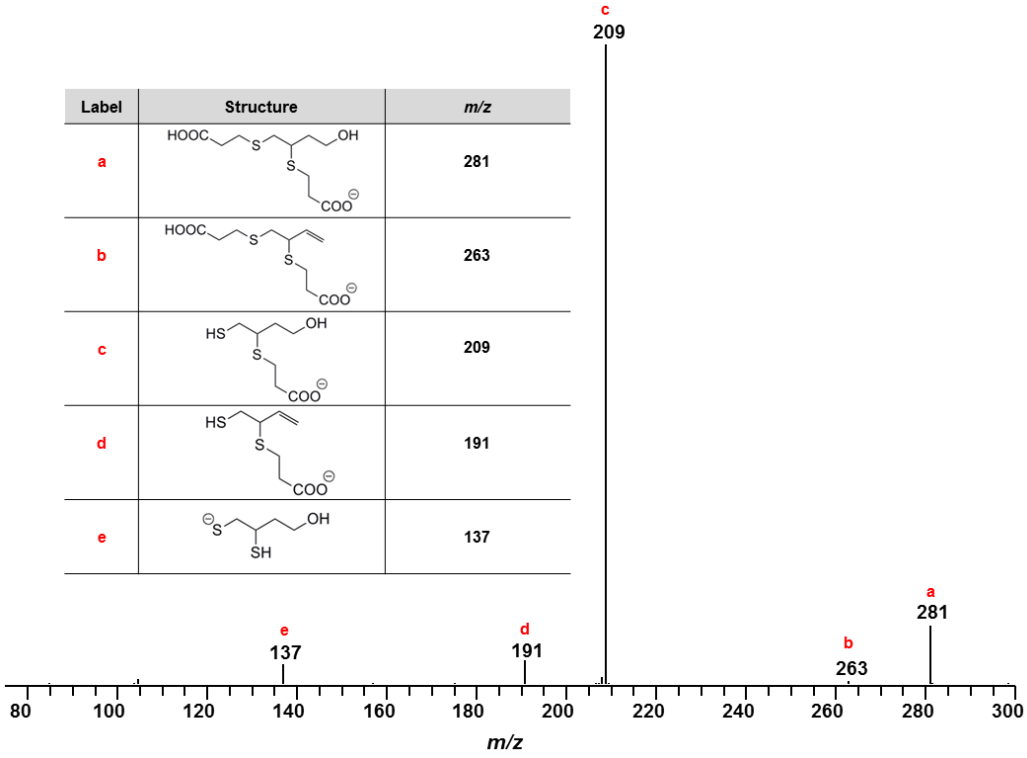

Figure 3.17. MS/MS spectrum of *m/z* 281.

3.2.5.3 Electrostatic Interaction-Induced Enzymatic Degradation of dNP Constructs

Our group recently reported the programmed hydrolysis of polylactide-containing nanoassemblies by electrostatic interaction-mediated enzymatic degradation behavior.[107] As the present constructs feature similar chemical composition, *i.e.*, a PLLA block segment, and physical features (anionic surface charge), we measured the electrostatic interaction-dependent enzymatic degradation rates of **3b** upon the addition of two model enzymes possessing positive and negative charges at physiological pH, *i.e.*, proteinase K (PK) with an isoelectric point (pI) *ca.* 8.9 and porcine liver esterase (PLE) with pI *ca*. 4.8, which can catalyze hydrolysis of poly(lactic acid). Consistent with our prior observations, treatment with PK yielded *ca.* 40% release of lactic acid,

compared with *ca.* 4% release by porcine liver esterase (Figure 3.18.). The accelerated production of lactic acid, reflecting degradation of the PLLA block segments, was attributed to attractive electrostatic interactions between oppositely–charged **3b** and PK. In contrast, the limited enzymatic activity of PLE toward **3b** was likely due to the repulsive electrostatic interaction between the two similarly charged objects, and also due to the lower activity of PLE *vs*. PK.

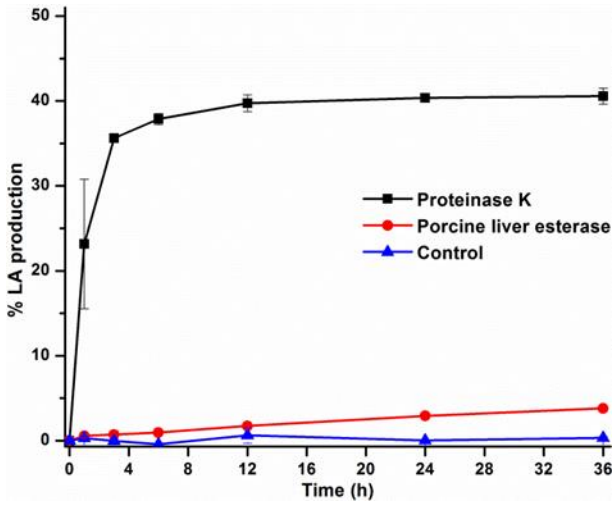

Figure 3.18. Degradation profiles of 3b in Tris-HCl buffer (100mM, pH 7.4) at 37 °C over 36 h, in the presence of proteinase K (black) and porcine liver esterase (red) and in the absence of enzyme (control, blue).

3.2.6. In Vitro Antimicrobial Activity of Ag-dNPs

It is well–known that a polymeric nanoparticle matrix may enhance the therapeutic efficacy of active agents by improving drug delivery features such as solubility, encapsulation, *etc*.[9] Thus, we evaluated the *in vitro* antimicrobial activities of silver compounds and silver-loaded micelles (**3a** or **3b**) by determining the minimal inhibitory concentrations (MICs) in Mueller-Hinton (MH) broth against eight

uropathogenic strains of *E. coli* and 10 contemporary strains of *S. aureus*. Silver compounds alone and silver-loaded **3** were tested in duplicate or triplicate wells of a 96-well plate and repeated on 3–6 separate days. When loading **3b** with each of the three silver species, AgOAc at 40 wt% loading, SCC22 at 100 wt% loading and SCC10 at 100 wt% loading, comparisons were expected to be made as to the nature of the silver components with a common polymer micelle nanoparticle, each at their highest loading levels. In addition, a fourth sample, having SCC22 loaded at 100 wt% into micelle **3a**, allowed for comparisons of the polymer nanoparticle with the same silver species. Aggregate results of multiple experiments comprised 9–15 trials of each sample with each bacterial strain. Overall, the MICs (expressed and compared as μg/mL Ag) of the silver compounds and silver-loaded nanoparticle constructs for *S. aureus* were higher than those for *E. coli*, but remained physiologically relevant (1–5 μg/mL) (Figure 3.19., Table 3.5., Table 3.6., and Table 3.7.). Among the three silver compounds alone, AgOAc displayed the most potent antimicrobial activity against both bacterial species; the average MIC values of AgOAc were 1.89 μg/mL for *E. coli* and 2.84 μg/mL for *S. aureus*, compared with 3.3 and 3.98 μg/mL of SCC22 and 3.78 and 4.03 μg/mL of SCC10, respectively (p value of AgOAc < 0.00001 relative to that of SCC22 or SCC10 for both *E. coli* and *S. aureus*; Table 3.7.). Interestingly, we observed significant improvement of antimicrobial activity of the SCCs upon nanoparticle packaging, *i.e., ca.* 50 and 70% lower MICs for SCC22-**3** and SCC10-**3** *vs*. SCC22 and SCC10, respectively (p values for mean MIC of SCC22-**3a**, SCC22-**3b** or SCC10-**3b** < 0.00001 relative to those of SCC22 or SCC10 for both *E. coli* and *S. aureus*). However, similar

improvement was not observed when packaging AgOAc into **3b**. Although we do not yet fully understand the mechanism, Ag^+ in a carbene complex appeared to be more efficacious with the micellar carrier system than was Ag^+ in a salt format. We previously reported a similar phenomenon.[87] We speculate that the nanoparticle-mediated delivery system provided protection to the SCC complexes and may have facilitated delivery of the silver species locally through nonspecific association of the nanoparticles with the bacterial cells. Of note, naked **3,** with no silver loading and applied at equivalent polymer concentrations, did not display antimicrobial activity nor toxicity to cultured mammalian cells. Taken together, these Ag-dNPs exhibited antimicrobial activities superior to small silver compounds, which supports the potential of using the developed degradable nanoparticles as an antimicrobial delivery system.

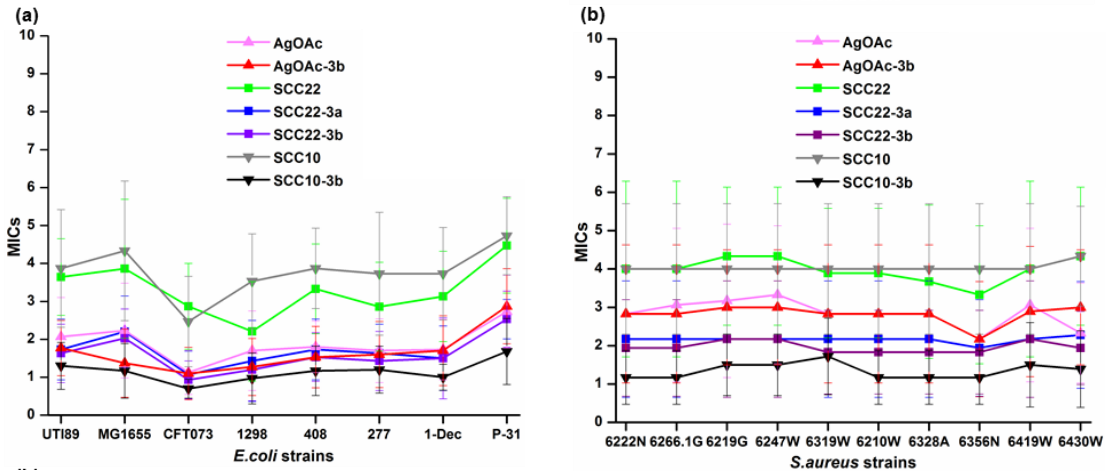

Figure 3.19. Minimum inhibitory concentration (MIC, μg/mL Ag) profiles of silver-compounds (AgOAc, SCC22 and SCC10) and silver-bearing micellar nanoparticles (AgOAc-3b, SCC22-3a, SCC22-3b and SCC10-3b) against (a) eight uropathogenic strains of *E. coli* and (b) 10 contemporary epidemic strains of *S. aureus*.

Table 3.5. Average MICs (μg/mL Ag) and % improvements of silver compounds .(AgOAc, SCC22 and SCC10) and silver-bearing micellar nanoparticles (AgOAc-3b, SCC22-3a, SCC22-3b, and SCC10-3b) against eight uropathogenic strains of *E. coli*.

	AgOAc	**SCC22**		**SCC10**
Avg. MIC	1.89	3.3		3.78
	AgOAc-3b	**SCC22-3a**	**SCC22-3b**	**SCC10-3b**
Avg. MIC	1.65	1.73	1.6	1.15
% Improvement	13%	48%	52%	70%

Table 3.6. Average MICs (μg/mL Ag) and % MIC improvement for silver compounds (AgOAc, SCC22 and SCC10) and silver-bearing micellar nanoparticles (AgOAc-3b, SCC22-3a, SCC22-3b and SCC10-3b) against 10 contemporary epidemic strains of *S. aureus*.

	AgOAc	**SCC22**		**SCC10**
Avg. MIC	2.84	3.98		4.03
	AgOAc-3b	**SCC22-3a**	**SCC22-3b**	**SCC10-3b**
Avg. MIC	2.82	2.16	1.97	1.34
% Improvement	1%	46%	51%	67%

Table 3.7. Minimum inhibitory concentrations (MICs) and statistical significance (*p*) values of parent silver compounds (AgOAc, SCC22 and SCC10) and silver-bearing micellar nanoparticles (AgOAc-3b, SCC22-3a, SCC22-3b and SCC10-3b) against 8 uropathogenic strains of *E. coli* and 10 contemporary epidemic strains of *S. aureus*. (Note: *p* values for MIC comparisons of silver-bearing micellar nanoparticles *vs.* parent silver compounds are shown.)

E. coli	**SCC22**	**SCC22-3a**	***p* vs SCC22**	**SCC22-3b**	***p* vs SCC22**	**AgOAc**	**AgOAc-3b**	***p* vs AgOAc**	**SCC10**	**SCC10-3b**	***p* vs SCC10**
UTI89	3.64±1.01	1.73±0.8	<0.001	1.63±0.77	<0.001	2.07±1.03	1.77±0.73	0.3658	3.87±1.55	1.3±0.62	< 0.001
MG1655	3.86±1.83	2.2±0.94	<0.005	2.03±0.77	<0.001	2.23±1.25	1.37±0.9	0.0378	4.33±1.84	1.17±0.72	< 0.001
CFT073	2.87±1.13	1.07±0.62	<0.001	0.93±0.5	<0.001	1.13±0.58	1.1±0.69	0.8869	2.47±1.19	0.7±0.25	< 0.001
1298	2.21±1.31	1.43±1.07	<0.089	1.2±0.82	<0.018	1.7±1.05	1.27±0.75	0.2042	3.53±1.25	0.97±0.67	< 0.001
408	3.33±1.18	1.73±0.8	<0.001	1.53±0.64	<0.001	1.8±0.68	1.53±0.81	0.3368	3.87±1.06	1.17±0.65	< 0.001
277	2.86±1.17	1.63±0.77	<0.002	1.43±0.78	<0.001	1.7±0.84	1.6±0.87	0.7513	3.73±1.62	1.2±0.62	< 0.001
1-Dec	3.13±1.19	1.5±0.85	<0.001	1.5±1.07	<0.001	1.73±0.8	1.7±0.92	0.9165	3.73±1.22	1±0.34	< 0.001
P-31	4.47±1.25	2.53±0.52	<0.001	2.53±0.74	<0.001	2.73±0.96	2.87±0.99	0.7111	4.73±1.03	1.68±0.87	< 0.001
mean	3.3	1.73		1.6		1.89	1.65		3.78	1.15	

14–15 wells

Table 3.7. Continued.

S. aureus	SCC22	SCC22-3a	*p* vs SCC22	SCC22-3b	*p* vs SCC22	AgOAc	AgOAc-3b	*p* vs AgOAc	SCC10	SCC10-3b	*p* vs SCC10
6222N	4±2.29	2.17±1.52	<0.063	1.94±1.26	0.031	2.83±1.8	2.83±1.8	1	4±1.7	1.17±0.7	< 0.001
6266.1G	4±2.29	2.17±1.52	<0.063	1.94±1.26	0.031	3.06±2	2.83±1.8	0.802	4±1.7	1.17±0.7	< 0.0
6219G	4.33±1.8	2.17±1.52	<0.014	2.17±1.52	0.014	3.17±2	3±1.5	0.8463	4±1.7	1.5±0.8	0.001
6247W	4.33±1.8	2.17±1.52	<0.014	2.17±1.52	0.014	3.33±1.8	3±1.5	0.6755	4±1.7	1.5±0.8	0.001
6319W	3.89±1.69	2.17±1.52	<0.037	1.83±1.09	0.007	2.83±1.8	2.83±1.8	1	4±1.7	1.72±1	0.004
6210W	3.89±1.69	2.17±1.52	<0.037	1.83±1.09	0.007	2.83±1.8	2.83±1.8	1	4±1.7	1.17±0.7	< 0.001
6328A	3.67±2	2.17±1.52	<0.092	1.83±1.09	0.028	2.83±1.8	2.83±1.8	1	4±1.7	1.17±0.7	< 0.001
6356N	3.33±1.8	1.94±1.26	<0.076	1.83±1.09	0.048	2.17±1.5	2.17±1.5	1	4±1.7	1.17±0.7	<0.00±1
6419W	4±2.29	2.17±1.52	<0.063	2.17±1.52	0.063	3.06±2	2.89±1.7	0.8486	4±1.7	1.5±1.1	0.002
6430W	4.33±1.8	2.28±1.39	<0.016	1.94±0.95	0.003	2.33±1.3	3±1.5	0.3322	4.33±1.3	1.39±1	< 0.001
mean	3.98	2.16		1.97		2.84	2.82		4.03	1.34	

9 wells

3.3. Experimental Section

3.3.1. Materials

Ammonium acetate, benzoic acid, 3-butyn-1-ol, dimethyl sulfoxide (DMSO), 2,2-dimethoxy-2-phenylacetophenone, 3-mercaptopropionic acid, 3-(*N*-morpholino)propanesulfonic acid (MOPS), porcine liver esterase (PLE) (activity = 154 U mg^{-1}, concentration = 35.6 mg of protein mL^{-1}), proteinase K (PK) (activity = 1362 U mL^{-1}, concentration = 36 mg of protein mL^{-1}), silver acetate (AgOAc) and triethylamine (TEA) were used as received from Sigma-Aldrich Company. 2-Chloro-2-oxo-1,3,2-dioxaphospholane (COP, 95%) was used as received from Thermo Fisher Scientific Inc. L-Lactide (LLA) (98%, Alfa Aesar) was purified and dried by azeotropic distillation in toluene three times. Benzyl alcohol and 1,8-diazabicyclo[5.4.0]undec-7-ene (DBU) were purchased from Sigma-Aldrich Company, and they were distilled from calcium hydride. The dried benzyl alcohol, DBU and LLA were stored in an argon-filled glovebox until use. Tetrahydrofuran (THF) and dichloromethane (DCM) were dried through columns (J. C. Meyer Solvent Systems, Inc.). 1-Methyl-3-(3-hydroxypropyl)-4,5-dichloroimidazol-2-ylidene silver (I) acetate (silver carbene complex 22, SCC22) and 1-methyl-3-hexyl-4,5-dichloroimidazole-2-ylidene silver (I) acetate (silver carbene complex 10, SCC10) were synthesized as previously reported.[108,109] Spectra/Pro membranes (MWCO 12–14 kDa, Spectrum Medical Industries, Inc., Laguna Hills, CA) were used for dialysis. The cell culture 96-well flat bottom plates were purchased from Corning Costar Co. Amicon ultra centrifugal filter devices (100 kDa MWCO) were purchased from Millipore Corp (Bedford, MA). Nanopure water (18 MΩ·cm) was

acquired by means of a Milli-Q water filtration system (Millipore Crop., Bedford, MA). The lactate colorimetric assay kit (ab65331) was purchased from Abcam. Dialysis cassettes (Slide-A-Lyzer, 10 kDa MWCO) were purchased from Pierce Biotechnology, Rockford, IL.

3.3.2. Characterization Methods

^{1}H, ^{13}C, and ^{31}P NMR spectra were recorded on Inova 300 MHz spectrometers interfaced to UNIX computers using VnmrJ software. Chemical shifts were referenced to solvent resonance signals. For ^{31}P NMR spectroscopy, phosphoric acid (85 wt% in H_2O) at 0 ppm was used as an external standard. IR spectra were recorded on an IR Prestige 21 system (Shimadzu Corp., Japan) and analyzed using the IRsolution software.

Size exclusion chromatography (SEC) measurements were performed on a Waters Chromatography, Inc. (Milford, MA) system equipped with an isocratic pump model 1515, a differential refractometer model 2414, and a four-column set of 5 μm Guard (50 × 7.5 mm), Styragel HR 4 5 μm DMF (300 × 7.5 mm), Styragel HR 4E 5 μm DMF (300 × 7.5 mm) and Styragel HR 2 5 μm DMF (300 × 7.5 mm). Polymer solutions were prepared at a concentration of about 3–5 mg/mL and an injection volume of 200 μL was used. Data collection and analysis were performed with Empower 2 v. 6.10.01.00 software (Waters, Inc.). The system was equilibrated at 70 °C in pre-filtered DMF containing 0.05 M of LiBr, which served as polymer solvent and eluent (flow rate set to 1.00 mL/min). The system was calibrated with polystyrene standards (Polymer Laboratories, Amherst, MA) ranging from 615 to 442800 Da.

Glass transition temperatures were measured by differential scanning calorimetry (DSC) on a Mettler-Toledo DSC822 (Mettler-Toledo, Inc., Columbus, OH), with a heating rate of 10 °C/min. Measurements were analyzed by using Mettler-Toledo Star^e v. 7.01 software. The T_g was taken as the midpoint of the inflection tangent, upon the third heating scan. Thermogravimetric analysis (TGA) was performed under N_2 atmosphere using a Mettler-Toledo model TGA/SDTA851e, with a heating rate of 10 °C/min and cooling rate of 10 °C/min. Measurements were analyzed by using Mettler-Toledo Star^e v. 7.01 software.

Dynamic light scattering (DLS) measurements were conducted using Delsa Nano C (Beckman Coulter, Inc., Fullerton, CA) equipped with a laser diode operating at 658 nm. Size measurements were made in nanopure water (n = 1.3329, η = 0.890 cP at 25 ± 1°C). Scattered light was detected at 165° angle and analyzed using a log correlator over 70 accumulations for a 3.0 mL sample in a glass sizing cell (4.0 mL capacity). The samples in the glass sizing cell were equilibrated for 30 min before measurements were made. The photomultiplier aperture and the attenuator were automatically adjusted to obtain a photon counting rate of *ca.* 10 kcps. Calculation of the particle size distribution and distribution averages was performed using CONTIN particle size distribution analysis routines. The peak averages of histograms from number distributions out of 70 accumulations were reported as the average diameters of the particles.

The ζ-potential values of the nanoparticles were determined by Delsa Nano C particle analyzer (Beckman Coulter, Fullerton, CA) equipped with a 30 mW dual laser diode (658 nm). The ζ-potential values of the particles in suspension were obtained by

measuring the electrophoretic movement of charged particles under an applied electric field. Scattered light was detected at a 30° angle at 25 °C. The ζ-potential was measured at five regions in the flow cell and a weighted mean was calculated. These five measurements were used to correct for electroosmotic flow that was induced in the cell due to the surface charge of the cell wall. All determinations were repeated three times.

Transmission electron microscopy (TEM) images were collected on a JEOL 1200EX, operating at 100 kV or a FEI Tecnai G2 F20 FE-TEM, operating at a voltage of 200 kV. High-resolution scanning transmission electron (STEM) microscopy was conducted on a FEI Tecnai G2 F20 FE-TEM coupled with energy-dispersive X-ray (EDX), operating at a voltage of 200 kV. The samples, as aqueous solution (5 μL, polymer concentration at 0.25–3.75 mg/mL), was deposited onto carbon-coated copper grids. After 1 min of deposition, the excess sample was quickly wicked off by using filter paper, and the grids were allowed to dry in the air for 10 min. Then, the grids were negatively stained with 5 μL of a 2% aqueous solution of uranyl acetate. The excess stain was wicked off using filter paper after 20 seconds. The sample grids were dried under vacuum at room temperature overnight before analysis.

Atomic force microscopy (AFM) was performed using a Multimode 8 system (Bruker) with an SA Fluid+ silicon probe (k 0.7 N/150 kHz, Bruker). For AFM preparation, nanoparticles were dissolved in nanopure water at 0.1 mg/mL, and 20 μL of the sample was spin coated onto a glass coverslip. All AFM samples were stored at

room temperature in a vacuum desiccator until use. AFM images were assessed with Nanoscope Analysis (Bruker).

Electrospray ionization (ESI) in negative ion mode was carried on a quadruple ion trap mass spectrometer (LCQ-DECA, ThermoFinnigan, San Jose, CA). The sample was directly infused at 6 μL/min of flow rate. The spray voltage was set at –4.5 kV. Sheath gas and auxiliary gas flow rates were 50 and 10 arbitrary units, respectively. Transfer capillary temperature was held at 250 °C. MS/MS experiments were performed on the same instrument at a relative collision energy of 30−32%. Xcalibur 2.0 software package (ThermoFinnigan) was used for data acquisition and processing.

Matrix-assisted laser desorption ionization (MALDI) experiments were performed on a Voyager DE-STR mass spectrometer (Applied Biosystems, Foster City, CA) under optimized conditions in positive linear mode. Ions were generated by a pulsed nitrogen laser at 337 nm and accelerated through 25 kV and 100 laser shots were used per spectrum. *Trans*-2-[3-(4-*t*-Butyl-phenyl)-2-methyl-2-propenylidene] malononitrile (DCTB) and potassium trifluoroacetate (KTFA) were used as a matrix and cationization reagent, respectively. The sample, KTFA, and matrix were prepared at concentration of 1, 10, and 20 mg/mL respectively. The sample solution was mixed with the matrix and KTFA at a volume ratio of 1:5:1. About 0.5 μL of this mixture was deposited on a stainless steel sample holder. After being allowed to air dry, the sample was analyzed using MALDI-TOF MS.

Ultraviolet–visible spectroscopy (UV–vis) absorption measurements were made using a UV-2550 system (Shimadzu Corp.). Measurements were performed in nanopure water in quartz cuvettes with path lengths of 1 cm.

Critical micelle concentration (CMC) values were determined by pyrene fluorescence measurements that were conducted on a RF-5301PC spectrofluorophotometer system (Shimadzu Corp., Kyoto, Japan) and analyzed using Panorama Fluorescence v. 2.1 software. Fluorescence emission spectra ranging from 360 to 450 nm of the sample solutions were recorded using an excitation wavelength of 334 nm at room temperature. Each measurement was repeated in triplicate.

Inductively coupled plasma-mass spectrometry (ICP-MS) was performed on a PerkinElmer SCIEX ICP mass spectrometer ELAN DRC II, equipped with high-speed quadrupole, dynamic reaction cell (DRC) and axial field technology (AFT) to completely eliminate polyatomic interferences, using 1% HNO_3 as the matrix and rhodium (Rh) as the internal standard.

Analysis of lactic acid by the colorimetric assay was made on a SpectraMax M5 microplate reader.

3.3.3. Synthesis of Monomer, 2-(But-3-yn-1-yloxy)-2-oxo-1,3,2-dioxaphospholane (BYP)

A solution of COP (14.9936 g, 105 mmol) in 50 mL of anhydrous THF was added dropwise to a stirred solution of 3-butyn-1-ol (8.1270 g, 116 mmol) and TEA (17 mL, 12 g, 120 mmol) in 200 mL of anhydrous THF at 4 °C. The reaction mixture was allowed to stir for 11 h at 4 °C and then for 30 min at room temperature. The precipitate

was filtered off, and the filtrate was concentrated under reduced pressure. The filtrate was distilled under reduced pressure to obtain a faint yellow and viscous liquid (110–120 °C, 0.5 mmHg) with a yield of 52.3%, 9.67 g, IR: 3330–3170, 3050–2870, 1474, 1283, 1009, 926, 835, 756 cm^{-1}. ^{1}H NMR ($CDCl_3$, ppm): δ 4.50–4.31 (m, 4H, POC*H*$_2$C*H*$_2$OP), 4.21 (dt, *J* = 9.3 Hz, *J* = 6.9 Hz, 2H, POC*H*$_2$CH$_2$C), 2.59 (ddt, *J* = 6.9 Hz, 2.4 Hz, 0.3 Hz, 2H, POCH$_2$C*H*$_2$C), 2.02 (t, *J* = 2.7 Hz, 1H, POCH$_2$CH$_2$CC*H*). ^{13}C NMR ($CDCl_3$, ppm): δ 79.21, 70.58, 66.34 (d, *J* = 23.7 Hz), 66.14 (d, *J* = 10.2 Hz), 20.82 (d, *J* = 25.5 Hz). ^{31}P NMR ($CDCl_3$, ppm): δ 18.02. +ESI MS: calculated $[M+H]^+$ for $C_6H_9O_4P$: 177.0317, found: 177.0311.

3.3.4. Synthesis of Diblock Copolymer, Poly(butynyl phosphotriester)$_{50}$-block-Poly(L-lactide)$_{50}$ (PPE$_{50}$-b-PLLA$_{50}$)

In a glovebox, a solution of BYP (3.0226 g, 17.2 mmol) and benzyl alcohol (35.3 µL, 37.0 mg, 0.340 mmol) in anhydrous DCM (3.0 mL) was transferred into a vial with a stir bar. DBU (102 µL, 104 mg, 0.682 mmol) was added *via* pipet into the mixture solution. After the mixture stirred for 7 min, a solution of LLA (2.4615 g, 17.1 mmol) in anhydrous DCM (21 mL) was quickly added into the mixture solution. After 4 min, the reaction was quenched by addition of a solution of benzoic acid in DCM (excess). The product was precipitated in diethyl ether (3×) and dried overnight under vacuum to afford the diblock copolymer product as a tacky white solid (4.9787 g, 91% yield). GPC: M_n = 21800 g/mol, PDI = 1.17. IR: 3350–3150, 3050–2850, 1757, 1456, 1271, 1211, 1184, 1130, 1074, 1009, 970, 804 cm^{-1}. ^{1}H NMR (CD_2Cl_2, ppm): δ 7.44–7.32 (m, 5H, aromatic ring), 5.16 (broad q, *J* = 7.2 Hz, 102H, ArC*H*$_2$OP and OCC*H*(O)CH$_3$),

4.40–4.22 (b, 200H, POCH_2CH_2O), 4.22–4.08 (b, 100H, POCH_2CH$_2$CCH), 2.67–2.54 (b, 100H, POCH$_2$CH_2CCH), 2.28–2.09 (b, 50H, OCH$_2$CH$_2$CC*H*), 1.55 (broad d, *J* = 7.2 Hz, 300H, CH_3CH(O)CO). ^{13}C NMR (CD_2Cl_2, ppm): δ 170.02, 130.07, 129.16, 128.57, 80.28, 71.00, 69.53, 67.00, 66.27, 21.06, 17.02. ^{31}P NMR (CD_2Cl_2, ppm): δ –1.02. DSC: T_g = -33 °C. TGA in N_2: 190-290 °C, 40% mass loss; 290–370 °C, 42% mass loss; 12% mass remaining above 370 °C.

3.3.5. Synthesis of Diblock Copolymer, Poly(butynyl phosphotriester)$_{90}$-block-Poly(L-lactide)$_{50}$ (PPE$_{90}$-b-PLLA$_{50}$)

In a glovebox, a solution of BYP (2.0014 g, 11.4 mmol) and benzyl alcohol (11.8 µL, 12.3 mg, 0.114 mmol) in anhydrous DCM (2.0 mL) was transferred into a vial with a stir bar. DBU (34 µL, 34.6 mg, 0.228 mmol) was added *via* pipet into the mixture solution. After the mixture stirred for 8 min, a solution of LLA (1.6434 g, 11.4 mmol) in anhydrous DCM (14.2 mL) was quickly added *via* pipet into the reaction mixture. After 4.5 min, the reaction was quenched by addition of a solution of benzoic acid in DCM (excess). The product was precipitated in diethyl ether (3×) and dried overnight under vacuum to afford the diblock copolymer product as a tacky white solid (2.0574 g, 78% yield). GPC: M_n = 22400 g/mol, PDI = 1.25. IR: 3350–3150, 3050–2850, 1757, 1454, 1383, 1360, 1271, 1211, 1186, 1130, 1072, 1011, 970, 860, 802, 752 cm^{-1}. ^{1}H NMR (CD_2Cl_2, ppm): δ 7.44–7.32 (m, 5H, aromatic ring), 5.17 (broad q, *J* = 7.2 Hz, 102H, ArCH_2OP and OCC*H*(O)CH$_3$), 4.38–4.22 (b, 360H, POCH_2CH_2O), 4.22–4.10 (b, 180H, POCH_2CH$_2$CCH), 2.68–2.53 (b, 180H, POCH$_2$CH_2CCH), 2.24–2.07 (b, 90H, OCH$_2$CH$_2$CC*H*), 1.56 (broad d, *J* = 7.2 Hz, 300H, CH_3CH(O)CO). ^{13}C NMR (CD_2Cl_2,

ppm): δ 170.02, 129.16, 128.57, 80.28, 71.00, 69.52, 67.00, 66.26, 21.06, 17.02. ^{31}P NMR (CD_2Cl_2, ppm): δ –1.02. DSC: T_g = -29 °C. TGA in N_2: 275 °C, 35 % mass loss; 350 °C, 32 % mass loss; 32 % mass remaining above 350 °C.

3.3.6. Synthesis of Diblock Copolymer, Poly(butynyl phosphotriester)$_{210}$-block-Poly(L-lactide)$_{50}$ (PPE$_{210}$-b-PLLA$_{50}$)

In a glovebox, a solution of BYP (1.9973 g, 11.3 mmol) and benzyl alcohol (3.9 µL, 4.1 mg, 0.038 mmol) in anhydrous DCM (2.3 mL) was transferred into a vial with a stir bar. DBU (17 µL, 17 mg, 0.11 mmol) was added *via* pipet into the reaction mixture. After the mixture stirred for 30 min, a solution of LLA (0.5451 g, 3.78 mmol) in anhydrous DCM (3.4106 mL) was quickly added *via* pipet into the reaction mixture. After 4.5 min, the reaction was quenched by addition of a solution of benzoic acid in DCM (excess). The product was precipitated in diethyl ether (3×) and dried overnight under vacuum to afford the diblock copolymer product as a tacky white solid (1.3689 g, 82% yield). GPC: M_n = 45600 g/mol, PDI = 1.26. IR: 3325–3125, 3025–2825, 1757, 1454, 1383, 1267, 1188, 1128, 1072, 1009, 972, 847, 804, 735 cm^{-1}. ^{1}H NMR (CD_2Cl_2, ppm): δ 7.44–7.32 (m, 5H, aromatic ring), 5.16 (broad q, J = 7.2 Hz, 102H, ArCH_2OP and OCC*H*(O)CH_3), 4.38–4.22 (b, 840H, POCH_2CH_2O), 4.22–4.10 (b, 420H, PO$CH_2$$CH_2$CCH), 2.68–2.53 (b, 420H, PO$CH_2$$CH_2$CCH), 2.24–2.07 (b, 210H, OCH_2CH_2CC*H*), 1.56 (broad d, J = 7.2 Hz, 300H, CH_3CH(O)CO). ^{13}C NMR (CD_2Cl_2, ppm): δ 170.02, 129.15, 128.57, 80.27, 70.99, 69.52, 67.01, 66.26, 21.05, 17.01. ^{31}P NMR (CD_2Cl_2, ppm): δ –1.03. DSC: T_g = -42 °C. TGA in N_2: 275 °C, 45 % mass loss; 360 °C, 20 % mass loss; 360 °C, 35 % mass remaining above 360 °C.

3.3.7. Thiol-yne "Click" Reaction of Alkyne Side Chain Moieties of PPE Block of PPE_{50}-b-$PLLA_{50}$ with 3-Mercaptopropionic Acid, 2a

A solution of PPE_{50}-*b*-$PLLA_{50}$ (0.1493 g, 0.00990 mmol), 3-mercaptopropionic acid (0.430 mL, 4.93 mmol) and 2,2-dimethoxy-2-phenylacetophenone (0.2153 g, 0.840 mmol) in 7.5 mL of DMSO was irradiated under UV irradiation (365 nm, 6 W) for 60 min while stirring. Purification included precipitation in diethyl ether (3×), followed by dialysis in nanopure water, and isolation of the product by freeze-drying overnight to give a tacky white solid (0.1892 mg, 75 % yield). IR: 3675–2760, 2700–2430, 1757, 1715, 1452, 1408, 1385, 1184, 1130, 1086, 1016, 982, 802, 754 cm^{-1}. ^{1}H NMR (DMSO-d_6, ppm): δ 13.2–11.9 (b, $SCH_2CH_2C(O)O\mathit{H}$), 7.44–7.26 (m, 5H, aromatic ring), 5.46 (d, *J* = 7.2 Hz, 2H, $ArC\mathit{H_2}O$), 5.20 (broad q, *J* = 7.2 Hz, 100H, $OCC\mathit{H}(O)CH_3$), 4.50–3.80 (b, 300H, $POC\mathit{H_2}C\mathit{H_2}O$ and $POC\mathit{H_2}CH_2CH$), 3.00–2.81 (b, 200H, $SCH_2C\mathit{H_2}COOH$), 2.80–2.62 (b, 250H, $SC\mathit{H_2}CH_2COOH$ and $SC\mathit{H}(CH_2)CH_2CH_2$), 2.60–2.50 (b, 100H, $SC\mathit{H_2}CHS$), 2.25–2.05 and 1.85–1.57 (b, 100H, $POCH_2C\mathit{H_2}CH$), 1.46 (broad d, *J* = 7.2 Hz, 300H, $OCCH(O)C\mathit{H_3}$). ^{13}C NMR (DMSO, ppm): δ 173.05, 172.19, 169.27, 68.72, 66.25, 65.34, 44.05, 42.91, 41.67, 38.19, 37.54, 34.73, 34.18, 33.53, 29.71, 27.18, 26.09, 25.22, 16.53. ^{31}P NMR (DMSO, ppm): δ –0.03. DSC: T_g = 6 °C. TGA in N_2: 105–190 °C, 13% mass loss; 190–280 °C, 40% mass loss; 280–350 °C, 25% mass loss; 22% mass remaining above 350 °C.

3.3.8. Thiol-yne "Click" Reaction of Alkyne Side Chain Moieties of PPE Block of PPE_{90}-b-$PLLA_{50}$ with 3-Mercaptopropionic Acid, 2b

A solution of PPE_{90}-*b*-$PLLA_{50}$ (0.1014 mg, 0.00437 mmol), 3-mercaptopropionic acid (0.34 mL, 3.90 mmol) and 2,2-dimethoxy-2-phenylacetophenone (0.1975 g, 0.771 mmol) in 7.5 mL of DMSO was irradiated under UV irradiation (365 nm, 6 W) for 60 min while stirring. Purification included precipitation in diethyl ether (3×), followed by dialysis in nanopure water, and isolation of the product by freeze-drying overnight to give a tacky white solid (0.1512 mg, 82 % yield). IR: 3375–2775, 2715–2400, 1713, 1404, 1180, 1130, 1074, 1020, 955, 799 cm^{-1}. ^{1}H NMR (DMSO, ppm): δ 13.2–12.2 (b, $SCH_2CH_2C(O)O\mathit{H}$), 7.45–7.30 (m, 5H, aromatic ring), 5.20 (broad q, *J* = 7.2 Hz, 100H, $OCC\mathit{H}(O)CH_3$), 4.35–3.70 (b, 540H, $POC\mathit{H_2}C\mathit{H_2}O$ and $POC\mathit{H_2}CH_2CH$), 3.00–2.80 (b, 360H, $SCH_2C\mathit{H_2}COOH$), 2.80–2.64 (b, 450H, $SC\mathit{H_2}CH_2COOH$ and $SC\mathit{H}(CH_2)CH_2CH_2$), 2.58–2.42 (b, 180H, $SC\mathit{H_2}CHS$), 2.25–2.05 and 1.85–1.60 (b, 180H, $POCH_2C\mathit{H_2}CH$), 1.46 (broad d, *J* = 7.2 Hz, 300H, $OCCH(O)C\mathit{H_3}$). ^{13}C NMR (DMSO, ppm): δ 172.86, 172.13, 169.21, 68.68, 64.56, 47.13, 46.80, 44.02, 42.92, 36.79, 34.82, 34.16, 29.27, 26.14, 16.49. ^{31}P NMR (DMSO, ppm): δ –0.02. DSC: T_g = 5 °C. TGA in N_2: 250 °C, 48 % mass loss; 365 °C, 28 % mass loss; 24 % mass remaining above 365 °C.

3.3.9. Thiol-yne "Click" Reaction of Alkyne Side Chain Moieties of PPE Block of PPE_{210}-b-$PLLA_{50}$ with 3-Mercaptopropionic Acid, 2c

A solution of PPE_{210}-*b*-$PLLA_{50}$ (0.1983 mg, 0.00448 mmol), 3-mercaptopropionic acid (0.83 g, 9.52 mmol) and 2,2-dimethoxy-2-phenylacetophenone

(0.4769 g, 1.86 mmol) in 9 mL of DMSO was irradiated under UV irradiation (365 nm, 6 W) for 60 min while stirring. Purification included precipitation in diethyl ether (3×), followed by dialysis in nanopure water, and isolation of the product by freeze-drying overnight to give a tacky white solid (0.3452 g, 86.0 % yield). IR: 3675–2775, 2775–2350, 1713, 1404, 1182, 1130, 1020, 974, 953, 799 cm^{-1}. ^{1}H NMR (DMSO, ppm): δ 13.6–12.2 (b, $SCH_2CH_2C(O)O\mathit{H}$), 7.45–7.30 (m, 5H, aromatic ring), 5.20 (broad q, J = 7.2 Hz, 100H, $OCC\mathit{H}(O)CH_3$), 4.30–3.65 (b, 1260H, $POC\mathit{H_2}C\mathit{H_2}O$ and $POC\mathit{H_2}CH_2CH$), 3.00–2.78 (b, 840H, $SCH_2C\mathit{H_2}COOH$), 2.78–2.65 (b, 1050H, $SC\mathit{H_2}CH_2COOH$ and $SC\mathit{H}(CH_2)CH_2CH_2$), 2.60–2.40 (b, 420H, $SC\mathit{H_2}CHS$), 2.30–2.08 and 1.85–1.55 (b, 420H, $POCH_2C\mathit{H_2}CH$), 1.46 (broad d, J = 6.9 Hz, 300H, $OCCH(O)C\mathit{H_3}$. ^{13}C NMR (DMSO, ppm): δ 172.87, 172.16, 169.21, 164.52, 68.68, 47.19, 46.80, 44.02, 42.96, 36.85, 34.91, 34.17, 29.28, 26.29, 16.48. ^{31}P NMR (DMSO, ppm): δ -0.02. DSC: T_g = -10 °C. TGA in N_2: 260 °C, 53 % mass loss; 350 °C, 14 % mass loss; 33 % mass remaining above 350 °C.

3.3.10. General Procedure for Self-Assembly of Amphiphilic Diblock Copolymers, Anionic Polyphosphoester-block-Poly(L-lactide) (aPPE-b-PLLA), 2

A total of 1.0 mg of **2** was suspended in nanopure water (for TEM and AFM analyses), MOPS buffer (50 mM, pH 7.4) or ammonium acetate buffer (50 mM, pH 5.0) (for DLS and ζ-potential measurements) in a vial, and the mixture was stirred for 30 min at room temperature prior to sample preparation.

3.3.11. Determination of Critical Micelle Concentrations (CMCs) for 2 To Afford Micelles 3 in Nanopure Water

The CMCs for **2a**, **2b** or **2c** in nanopure water were determined using pyrene as the fluorescent probe following the protocol in literature.[110] A total volume of 0.75 mL of sample solution was prepared by mixing **2** in nanopure water (ranging from *ca.* 0.01–3.5 mg/mL) with a pyrene aqueous stock solution (0.250 mL, 6.0×10^{-7} mol/L). All the sample solutions were then stored at room temperature for 1 followed by storage at 4 ºC overnight to equilibrate the pyrene and the micelles. The fluorescence measurement was conducted at room temperature, in which the pyrene was excited at 334 nm and its emission spectrum was recorded at 373 and 384 nm, corresponding to the first and third vibrational peaks, respectively. All measurements were repeated in triplicate and the ratios of intensities of the first (*I*I) and third (*I*III) peaks were plotted against the concentrations of **3** in the sample solutions. The CMC was taken as the intersection of the tangent to the curve at the inflection with tangent through the points at lower polymer concentration.

3.3.12. General Procedure for the Preparation of AgOAc-Loaded Degradable Polymeric Nanoparticles (AgOAc-3)

A solution of AgOAc (4 mg/mL in nanopure water) was added dropwise to a solution of **2** (1.5 mL, polymer concentration = 5 mg/mL). The solution was shielded from light and allowed to stir overnight at room temperature. Then, the solution was washed thoroughly with nanopure water (>4 cycles) to remove free small silver-compounds by using a centrifugal filter device (100 kDa MWCO). The absence of free

Ag^+ from the mixture solution was confirmed by observing no occurrence of precipitates (AgCl) upon adding a saturated solution of sodium chloride to the filtrate. The resulting solution of AgOAc-**3** was reconstituted to a final volume of 2 mL, and silver concentration was measured by ICP-MS. Aliquots of the solution of AgOAc-**3** were used for UV–vis, TEM and DLS measurements.

3.3.13. General Procedure for the Preparation of SCC22-Loaded Degradable Polymeric Nanoparticles (SCC22-3)

A solution of SCC22 (10 mg/mL in nanopure water) was added dropwise to the solution of **2** (1.5 mL, polymer concentration = 5 mg/mL). The solution was shielded from light and allowed to stir overnight at room temperature. Then, the solution was washed thoroughly with nanopure water (>4 cycles) to remove free small silver-compounds by using a centrifugal filter device (100 kDa MWCO). The absence of free Ag^+ from the mixture solution was confirmed by observing no occurrence of precipitates (AgCl) upon adding a saturated solution of sodium chloride to the filtrate. The resulting solution of SCC22-**3** was reconstituted to a final volume of 2 mL, and silver concentration was measured by ICP-MS. Aliquots of the solution of SCC22-**3** were used for UV–vis, TEM and DLS measurements.

3.3.14. General Procedure for the Preparation of SCC10-Loaded Degradable Polymeric Nanoparticles (SCC10-3)

A solution of SCC10 (10 mg/mL in $CHCl_3$) was added dropwise to a solution of **2** (1.5 mL, polymer concentration = 5 mg/mL). The solution was shielded from light and allowed to stir vigorously to form a water/$CHCl_3$ emulsion overnight at room

temperature. After evaporation of the organic solvent overnight, the solution was washed thoroughly with nanopure water (>4 cycles) to remove free small silver-compounds by using a centrifugal filter device (100 kDa MWCO). The absence of free Ag^+ from the mixture solution was confirmed by observing no occurrence of precipitates (AgCl) upon adding a saturated solution of sodium chloride into the filtrate. The resulting solution of SCC10-**3** was reconstituted to a final volume of 2 mL, and silver concentration was measured by ICP-MS. Aliquots of the solution of SCC10-**3** were used for UV–vis, TEM and DLS measurements.

3.3.15. General Procedure for Study of Silver Release Kinetics of Silver Compounds (AgOAc, SCC22 or SCC10) and Ag-3 (Loaded by AgOAc, SCC22, or SCC10)

Into a presoaked dialysis cassette (Slide-A-Lyzer, 10 kDa MWCO, Pierce Biotechnology, Rockford, IL) was transferred a solution of silver compounds or Ag-**3** (3 mL) was transferred. The dialysis cassette was incubated in nanopure water at 37 °C for 5 days. For SCC10, it was dissolved in THF, and the solution was transferred into the dialysis cassette. Aliquots (*ca*. 0.1 mL) of solution were extracted at predetermined intervals, and the concentration of silver was measured by ICP-MS. The final results were obtained from triplicate experiments.

3.3.16. Investigation of Nanoparticle Stability in Aqueous Solution by Monitoring the Changes in Hydrodynamic Diameters of 3b, as Measured by DLS

In MOPS buffer (50 mM, pH 7.4) or ammonium acetate buffer (50 mM, pH 5.0) in a vial, **2b** was dissolved (0.5 mg/mL). The prepared solution was incubated in a

shaker at 37 °C, and hydrodynamic diameter and ζ-potential were monitored by using DLS and ζ-potential, respectively, over time.

3.3.17. Preparation and Identification of the Degradation Products of 3b

A solution of **2b** (9.2 mg) in 2 mL of nanopure water was incubated in a shaker at 37 °C until the micelles were not detectable by DLS. The solution was lyophilized into a powder, and then analyzed by ESI MS, MALDI-TOF MS, and ^{31}P NMR spectroscopy.

3.3.18. Study of Enzymatic Degradation of PLLA Block Segment of 3b Using Proteinase K (PK) and Porcine Liver Esterase (PLE)

The enzymatic degradation experiments was performed following our previous report.[107] A solution of **2b** (0.5 mL, 0.0032 mM, 0.32 mM of LLA) in 0.1 M Tris-HCl buffer at pH 7.4, containing 0.05% (w/v) NaN_3, was placed in 1.5 mL centrifugation tubes. Two stock solutions of PLE and PK were also prepared in 0.1 M Tris-HCl buffer at pH 7.4, containing 0.05% (w/v) NaN_3, to maintain similar enzymatic activities (*ca*. 1 U/μL). The solution of PLE (91 μL, 5,482 U/mL) was diluted in 409 μL of Tris-HCl buffer and the solution of PK (367 μL, 1,362 U/mL) was diluted in 133 μL of Tris-HCl buffer. For the enzyme-catalyzed hydrolysis of nanoparticles, stock solutions of enzyme (50 μL, 1 U/ μL) were added to each tube, mixed by the use of a vortex, and incubated at 37 °C, using an incubating shaker. As a control, to determine the hydrolytic degradation rates of the PLLA block segment of the samples in the absence of enzyme catalysis, 50 μL of Tris-HCl buffer was added to each solution (to maintain identical polymer concentrations as the enzyme catalyzed experiment) and incubated at 37 °C in a shaker.

The lactate assays were performed following the standard protocol of ab65331 as described below. At time points 0, 1, 6, 12, and 24 h, 50 µL of sample was withdrawn from each tube, mixed with 50 µL of lactate enzyme assay mix in a 100 µL Falcon clear well, protected from light and incubated at room temperature for 30 min to produce color, and analyzed using a plate reader for absorption at 450 nm. Each analysis was performed in triplicate, and average absorbance values with standard deviations were reported. A calibration curve of L-lactic acid was constructed by the use of serial dilutions that were produced from a standard solution of 0.1 M L-lactic acid in 0.1 M Tris-HCl buffer (calibration range: 0–10 nmol of lactate), and the production of L-lactic acid at each time point was quantified and reported as a percentage of the total theoretical L-lactic acid present in each solution at the predetermined concentrations.

3.3.19. Antibacterial Activity

Minimum inhibitory concentration (MIC) was determined by microdilution in Mueller-Hinton (MH) broth. Briefly, strains were streaked from glycerol stocks onto tryptic soy agar plates and grown overnight at 37 °C. In the following morning, colonies were suspended in MH media until $OD_{650\ nm} = 0.2$, and then incubated with shaking at 37°C until $OD_{650\ nm} = 0.4$ (~5×10^8 colony-forming units [CFU]/mL). Bacterial strains were then diluted to 2×10^5 CFU/mL in MH media and finally diluted 1:1 with compounds.

Silver-compounds were resuspended fresh on the day of the experiment in sterile water to a working concentration of 200 µg/mL silver. Each compound was then diluted in MH media to a dose between 0.5 and 12 µg/mL and diluted 1:1 with bacteria. Plates

were incubated statically overnight at 37 °C in the dark and read visually on the next day. The MIC was recorded as the lowest silver dose that did not permit bacterial growth.

Each compound was tested in duplicate or triplicate wells of a 96–well plate and repeated on 3–6 separate days. Results included 1–2 separate batches of compounds for a total of 9–15 trials of each compound with each bacterial strain. Naked **3**, *i.e.*, **3** without silver-loading, was also examined, and the sample did not display any inhibitory activity within the ranges tested.

3.4. Conclusions

In conclusion, fully degradable and functional polymeric nanoparticles as delivery carriers for silver-based antimicrobials were developed, and their *in vitro* antimicrobial efficacy and degradability were investigated. A series of nanoparticles, composed of amphiphilic diblock copolymers of phosphoester and L-lactide with varying hydrophilic chain lengths, were designed and prepared as potential delivery carriers for three different types of silver-based antimicrobials. While there was no evidence of an influence of hydrophilic chain length or loading site on the silver-loading capacity of dNPs, optimization of the feed ratio was critical to maximizing the silver loading capacity. The fast release kinetics of Ag-dNPs, typically found in the use of micelles, could be beneficial for treatment of infectious diseases, *e.g.*, lung infections *via* pulmonary inhalation administration or urinary tract infections *via* direct inoculation of therapeutics. The dNP-based antimicrobial delivery system exhibited significant improvement in *in vitro* antimicrobial activity over the parent silver compounds,

particularly with reference to the silver carbene cargo. Finally, the degradability of these NPs was demonstrated in comprehensive degradation studies, including the stability of dNPs by DLS measurement, identification of the degradation products by ESI MS, and electrostatic interaction-mediated enzymatic degradation of dNPs by lactate essays. Further studies will develop a better understanding of the fundamental interactions between bacterial cells, the dNPs and their degradation products. Moreover, conjugation of the dNPs with tissue-specific targeting proteins or peptides and determination of *in vivo* biodistribution, toxicity, and therapeutic efficacy of the Ag-dNPs against bacterial infectious diseases represent important future goals in demonstrating the translational potential of these novel nanoconstructs.

CHAPTER IV

DEVELOPMENT OF A VINYL ETHER-FUNCTIONALIZED POLYPHOSPHOESTER AS A TEMPLATE FOR MULTIPLE POSTPOLYMERIZATION CONJUGATION CHEMISTRIES AND STUDY OF CORE DEGRADABLE POLYMERIC NANOPARTICLES*

4.1. Introduction

Although ring-opening polymerizations (ROPs) provide a method to transform cyclic monomers into well-defined, functional, and degradable polymers,[36,60,90] it has been challenging, in general, with some exceptions,[111,112] to overcome difficulties that are often experienced in the attempt to introduce functional moieties within the cyclic monomer structures and with incompatibilities of these desired functionalities during the polymerizations. Alternatively, "click" chemistries such as azide–alkyne Huisgen cycloaddition,[113] Diels–Alder reaction,[114] and radical-mediated thiol–ene/yne reactions[62,115] have revolutionized polymer chemistry, allowing for efficient and reliable routes toward postpolymerization modifications in the design of complex and functional polymeric materials.[116-119]

*Part of this work is reprinted with permission from "Development of a Vinyl Ether-Functionalized Polyphosphoester as a Template for Multiple Postpolymerization Conjugation Chemistries and Study of Core Degradable Polymeric Nanoparticles" by Lim, Y. H., Heo, G. S., Rezenom, H. Y., Pollack, S., Raymond, J. E., Elsabahy, M., and Wooley, K. L., 2014, *Macromolecules*, 47(14), 4634–4644. Copyright [2014] by the American Chemical Society.

Combined with the extraordinary efficiency in the generation of stable covalent linkages by "click"-type reactions in biomaterials,[120] acid-labile functionalities, such as acetals,[121-123] ortho esters,[124,125] and hydrazones,[126,127] are also of major interest in contemporary materials design, especially toward biomedical applications.[128] In spite of the wide utilization of acetals/thio-acetals in synthetic organic chemistry (*e.g.* as hydroxyl protecting groups), they have received less attention in polymer chemistry. The most intriguing characteristic of acetal/thio–acetal functionalities originates from their unique property of behaving as a "dynamic covalent bond", *i.e.* being cleavable upon exposure to acidic conditions such as those found in the gastrointestinal tract, tissue at sites of inflammation and in tumors, and in endosomal and lysosomal compartments,[129-131] while being relatively stable at the normal physiological pH.[122,123,132-134] In this context, acetals/thio–acetals are appealing for their incorporation into biomacromolecules, where the dynamic covalent linkages can bridge to biologically active molecules and, ultimately, release them at a targeted site in a controlled manner. Furthermore, introduction of hydroxyl functionalities by controlled cleavage of acetals/thio–acetals would improve the hydrophilicity of a given polymer, which has been limited conventionally due to their incompatibility with the polymerization processes.[135]

The inherent acid-labile property of acetals has been introduced to the backbone or the side chains of functional polymers or cross-linkers in the preparation of cross-linked nanoparticles. For instance, among several elegant works, reports on acetal-linked linear polymers or dendrimers have elucidated the cleavability as well as the

chemical stability of acetal linkages in a broad spectrum of polymeric systems, *e.g.*, degradable, biocompatible dextrans, by Frechet *et al.*;[121-123,132,134] poly(ethylene oxides) connected with cleavable acetals by Hawker *et al.*;[136] hydroxyl-group protection during anionic polymerization and hyperbranched polyethers with acetal backbone linkages by Frey *et al.*;[135,137] acetal-based degradable shell cross-linked polymeric micelles by Wooley *et al.*;[138] introduction of vinyl ether side chain moieties along poly(ethylene glycol) backbones by Wurm *et al.*[139] and Brocchini *et al.*;[140] and acetal-linked backbone-cleavable ABA-type triblock copolymers by Ni *et al.*[141] Here, our interest is the application of acid-labile acetal/thio–acetal linkages to the side chains in degradable polymeric systems for their potential use as drug delivery carriers. Recently, acetal-linked prodrug micellar nanoparticles and their pH-triggered controlled drug release from the side chains have been highlighted by Zhang *et al.*[142] and Zhong *et al.*[143] However, the polymeric nanoconstructs used in these studies were hydrocarbon-based, nondegradable backbone systems – polymethacrylates and poly(acrylic acid), respectively – which limit their application as potential biomaterials because of the possible long-term accumulation in the human body.

A major effort of our group has been to develop polyphosphoesters (PPEs) tailored by manipulation of pendant functional groups on the pentavalent phosphorus atoms and to integrate the PPE system into new classes of degradable, biocompatible polymeric nanomaterials.[39,94,96,98,144] Particularly, introduction of reactive vinyl ether moieties to degradable, biocompatible PPEs[58] and their utilization to conjugate a library of hydroxyl- or thiol-containing biologically active molecules *via* multiple types of

conjugation chemistries are envisioned to expand the breadth of this chemical approach in the development of functional biomaterials.

Herein, we report the organocatalyzed ROP of ethylene glycol vinyl ether-containing cyclic phosphotriester monomer, as an initial fundamental study toward unique degradable, functional polymer materials. After demonstrating the well-controlled homopolymerization of the monomer with predetermined molecular weights and narrow molecular weight distributions, the resulting vinyl ether-functionalized PPE scaffold was conjugated with hydroxyl- or thiol-containing model small molecules *via* three different types of conjugation chemistries – thiol–ene "click" reaction, acetalization, or thio–acetalization reaction – revealing efficient routes for postpolymerization modifications of functional polymers. Furthermore, amphiphilic diblock copolymers containing the ethylene glycol vinyl ether-functionalized PPE as a hydrophobic block segment, also prepared by ROP, afforded well-defined micelles that showed a pH-dependent hydrolytic core degradability of both backbone and side chains in aqueous solutions. The degradation products, as identified by mass spectrometry, were found to be nontoxic toward two standard cell lines: RAW 264.7 mouse macrophages and OVCAR-3 human ovarian adenocarcinoma cells. Hence, this polymeric system can have potential applications in the development of nanomedical devices for a variety of biomedical applications.

4.2. Results and Discussions

4.2.1. Monomer Design and Synthesis

A novel ethylene glycol vinyl ether-functionalized cyclic phosphotriester monomer, 2-ethylene glycol vinyl ether-1,3,2-dioxaphospholane 2-oxide (EVEP), **1**, was synthesized by following a typical condensation method: coupling of ethylene glycol vinyl ether (EVE) to 2-chloro-3-oxo-1,3,2-dioxaphospholane (COP) in the presence of triethylamine (TEA) in dichloromethane (DCM) at 4 °C (Figure 4.1.). It was critical to purify the monomer rigorously, by removing the residual starting materials completely, because of the potential for undesired dual initiation by residual EVE and the possible formation of random/branched (co)polymers by remaining reactive COP during the polymerization process. Multiple purification methods, including silica gel column chromatography, (vacuum) distillation, extraction, and precipitation, were attempted, but decomposition of the reactive cyclic monomer and/or incomplete removal of the impurities were inevitable in all cases. Therefore, use of an exact stoichiometric equivalence of reagents was attempted, and then the purification process was applied for removal of the TEA salts by a series of recrystallization in DCM, precipitation in diethyl ether, and filtration. Even though tetrahydrofuran (THF) could be used as a solvent, DCM was more efficient for recrystallization of the TEA salts. The quantitative conversion of EVE and COP to **1** was supported by ^{1}H, ^{13}C, and ^{31}P NMR spectroscopy (Figure 4.2.). By ^{13}C NMR spectroscopy, the methylene carbon of the hydroxymethyl group of EVE resonating as a singlet (^{1}H-decoupled) at 61.2 ppm disappeared upon coupling to COP to result in a doublet ($J(^{31}P,^{13}C)$) having a coupling constant of 10.2 Hz

at 66.1 ppm for the methylene carbon of the new phosphoester linkage. In addition, consumption of the COP was observed by ^{31}P NMR spectroscopy as replacement of the COP phosphorus resonance at 23.20 ppm with that for the monomer at 17.91 ppm. Although the conversion to monomer appeared to be complete, ^{1}H NMR analysis indicated that there were residual solvents and TEA salts that were not removed (~ 96% purity). However, those impurities did not impact the polymerization.

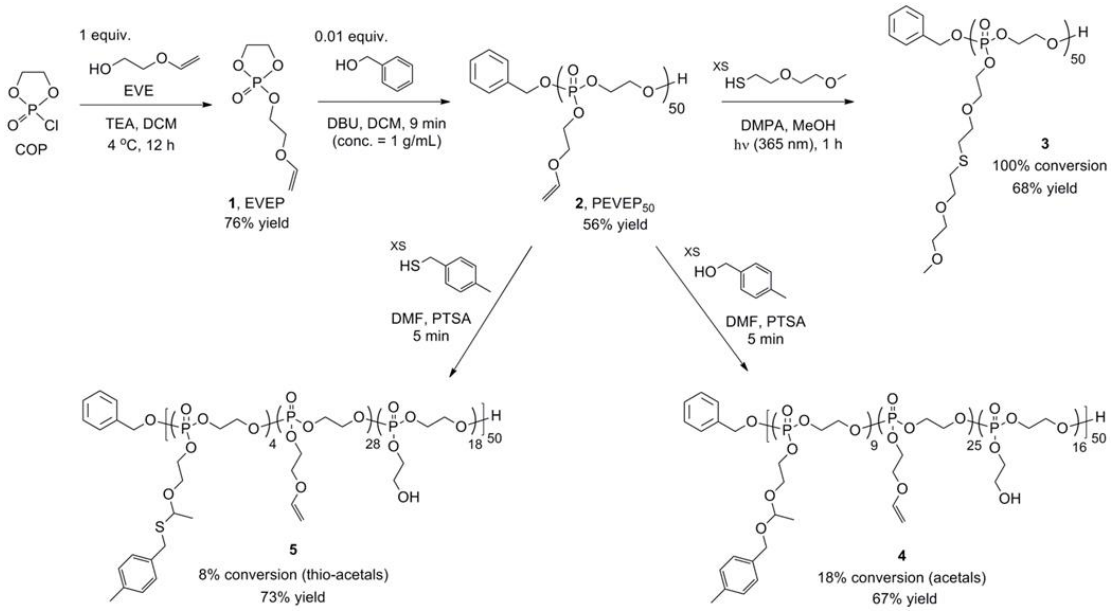

Figure 4.1. Synthetic route for the preparation of ethylene glycol vinyl ether-functionalized cyclic phosphotriester monomer 1 and homopolymer 2 by ROP followed by postpolymerization modifications *via* three different types of conjugation chemistries: Thiol-ene "click" reaction, acetalization, or thio-acetalization reaction.

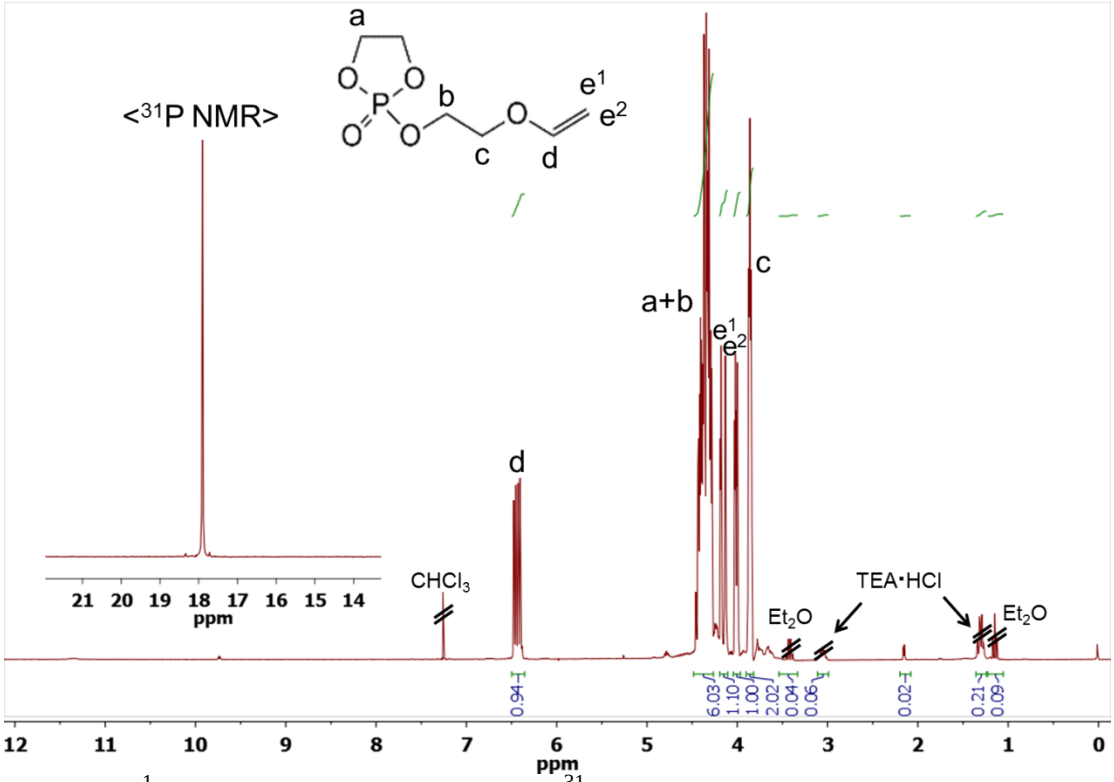

Figure 4.2. ^{1}H (300 MHz, $CDCl_3$, ppm) and ^{31}P (121 MHz, $CDCl_3$, ppm, inset) NMR spectra of 1.

4.2.2. Homopolymerization of the Monomer 1 by Using an Organocatalyst, DBU

The ROP of **1** was performed in a glovebox at ambient temperature. For the kinetic study, **1** and benzyl alcohol (BnOH) (molar ratio of 100:1) were mixed in DCM, and the polymerization began with the addition of 1,8-diazabicyclo[5.4.0]undec-7-ene (DBU) (molar ratio to initiator of 3:1). After being stirred for a predetermined period of time, an aliquot of the reaction mixture was collected, immediately quenched by adding a solution of excess benzoic acid in DCM, and then analyzed by ^{31}P NMR spectroscopy. A portion of the collected samples was precipitated into diethyl ether prior to injection into the gel permeation chromatography (GPC) instrument (Figure 4.3.). Although

routine decoupled ^{31}P NMR spectroscopy has complications that may limit the quantitative value, the distinct resonance frequencies of the phosphorus nuclei of the monomer *vs*. the polymer provided the best opportunity (relative to ^{1}H or ^{13}C NMR spectroscopy) to monitor the polymerization. Therefore, the conversion was estimated from ^{31}P NMR spectroscopy by comparing the integral ratio of two distinct peaks of monomer **1** at 17.91 ppm and homopolymer, PEVEP, at –0.68 ppm, on crude polymerization aliquots. Once the polymerization was quenched and workeup, ^{1}H NMR spectroscopy end-group analysis of the degree of polymerization was found to be in agreement with the monomer conversion calculated from the ^{31}P NMR data. Both the molecular weight and its distribution were determined by GPC. The kinetic study displayed a rapid initial polymerization rate, in which the monomer conversion reached at 23% within the beginning 3 min. However, the maintenance of linearity of M_n *vs.* monomer conversion suggested a living ROP up to 79% conversion (Figure 4.3. (b)). The consistent low PDIs ($\leq$1.04) until the monomer conversion reached at 79% indicated that there was minimal adverse transesterification of the PPE backbone during the polymerization process. A kinetic plot of $\ln([M]_0/[M])$ *vs.* polymerization time illustrated pseudo-first-order kinetics (Figure 4.3. (a)), which is a typical characteristic of ROP.

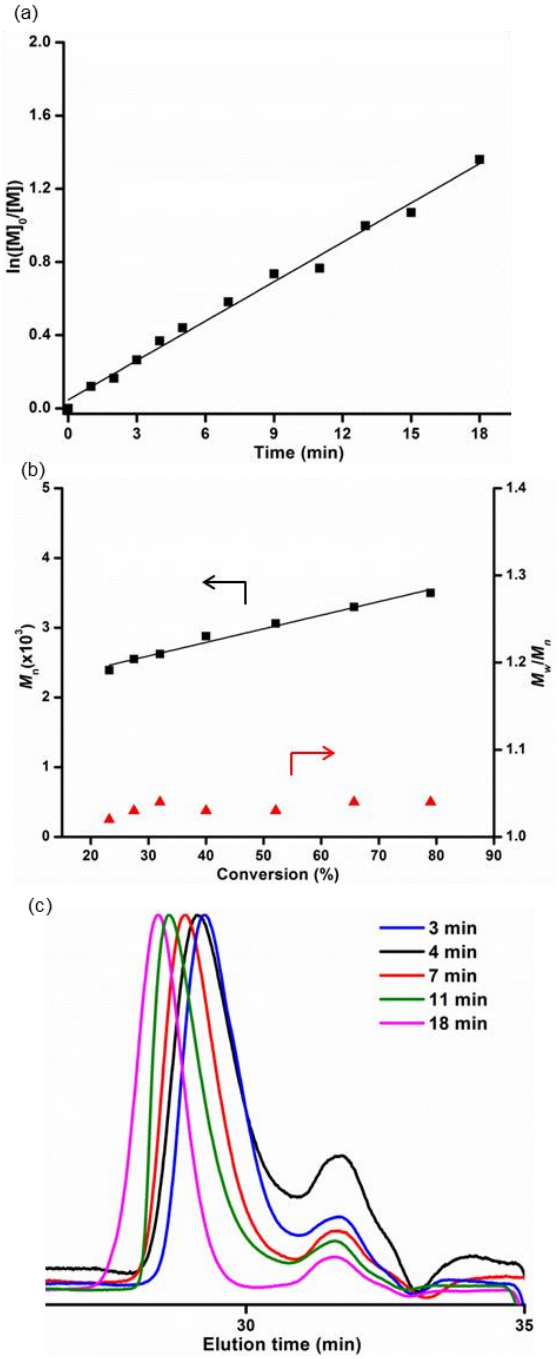

Figure 4.3. (a) Kinetic plots of $\ln([M]_0/[M])$ *vs.* polymerization time (min), obtained from ^{31}P NMR spectroscopy data. (b) Kinetic plots of M_n and M_w/M_n *vs.* monomer conversion in ROP of 1, obtained from GPC analysis. (c) GPC traces as a function of elution time (min), after work-up of aliquots of the polymerization mixture by quenching with a solution of excess of benzoic acid in DCM and precipitation into diethyl ether. Conditions: [EVEP] = 5.2 M in DCM, [EVEP]:[BnOH]:[DBU] = 100:1:3.

The same molar ratio used for the kinetic study was applied for a scaled-up production of **2**. The purification of **2** by precipitation in diethyl ether was insufficient to remove the residual starting materials and benzoic acid completely. Silica gel column chromatography was also attempted, but instability of the PPE backbone was problematic. Dialysis (MWCO 6–8 kDa) of the reaction mixture against organic solvents, switching from MeOH to DCM, was the most assured purification method among those tested. Dialysis in basic aqueous solutions (*e.g.* carbonate buffer at pH 7–8) was also feasible, but the complete removal of water was challenging, which is imperative for the following post-polymerization modification reactions. Being consistent with the kinetic study, quenching the polymerization at a predetermined time (9 min), targeting at 50% conversion, yielded the predicted molecular weight and PDI. The degree of polymerization (DP_n) calculated based on ^{31}P NMR spectroscopy-determined monomer conversion was in agreement with that calculated from chain-end analysis by ^{1}H NMR spectroscopy, *i.e.*, by comparisons of the integrals of proton resonances of the benzyl group (7.43–7.34 or 5.08 ppm, labeled as a or b, respectively, in Figure 4.4.(a)) of the initiated chain end to those of the distinct double bonds (6.49 or 4.06 ppm, labeled as f or g^2, respectively, in Figure 4.4.(a)) or β protons on the substituents to the phosphorus atom (3.94–3.86 ppm, labeled as e in Figure 4.4.(a)) of **2**, which was indicative of retention of the vinyl groups (Figure 4.4.(a)). In addition, one distinct ^{31}P resonance confirmed the stability of the degradable PPE backbone during ROP of **1** and the work-up process of **2**. GPC analysis of **2** showed a monomodal peak with PDI of 1.05.

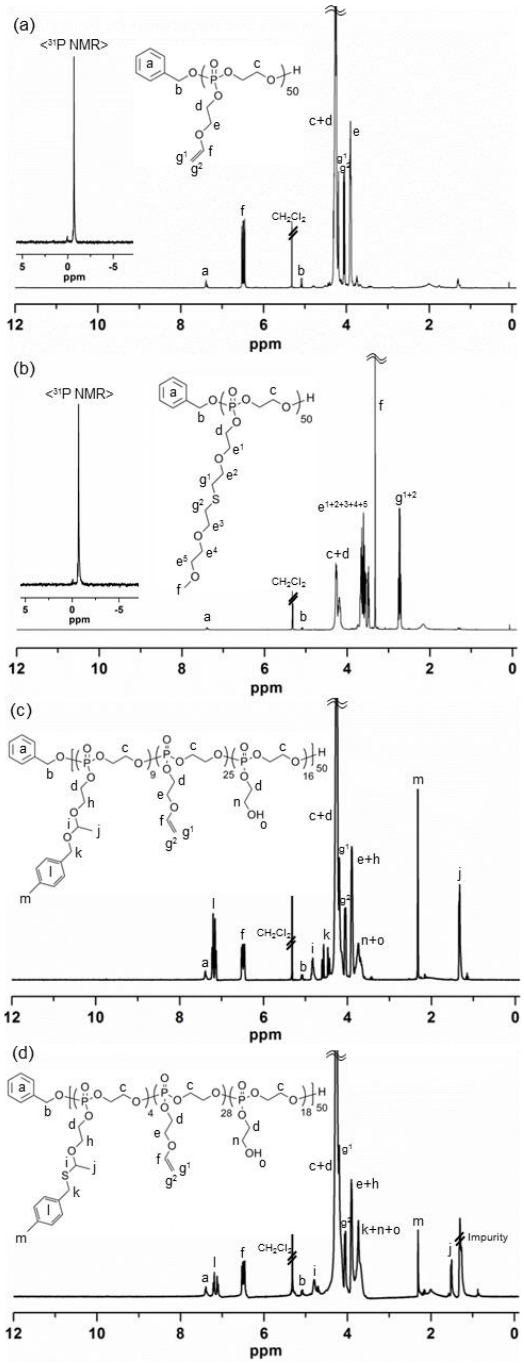

Figure 4.4. ^{1}H (300 MHz, CD_2Cl_2, ppm) and ^{31}P (121 MHz, CD_2Cl_2, ppm, inset) NMR spectra of (a) 2, (b) 3, (c) 4, and (d) 5.

4.2.3. Thiol-ene "Click" Reaction of the Vinyl Ether Side Chain Moieties of PEVEP$_{50}$ 2 with 2-(2-Methoxyethoxy)ethanethiol

The vinyl ether side chain moieties of **2** were functionalized by thiol–ene "click" reaction with thiol-containing model small molecule, 2-(2-methoxyethoxy)ethanethiol. The radical-mediated thiol–ene "click" chemistry is a robust and versatile method that tolerates a variety of functional groups in achieving a high degree of functionalization on vinyl groups.[62,115] Herein, this efficient chemistry was applied to demonstrate the presence and chemical availability of vinyl groups on **2**. To verify the integrity of the PPE backbone in the presence of radicals during UV irradiation, a mixture of **2** and 2,2-dimethoxy-2-phenylacetophenone (DMPA) in methanol-d_4 ($MeOD_4$) was irradiated under UV light (365 nm, 6 W) for several hours, as a preliminary control reaction. ^{31}P NMR spectroscopy confirmed that the polymer backbone was intact under these conditions. Accordingly, an excess of 2-(2-methoxyethoxy)ethanethiol relative to the vinyl ether bonds was employed with DMPA in MeOH and UV irradiation for 1 h to ensure a high coupling efficiency and to avoid undesired cross-linking reactions between the double bonds along the backbone. The purified products were obtained by conducting precipitation in diethyl ether followed by sequential dialysis (MWCO 6–8 kDa) against MeOH and DCM. Comparison of the ^1H NMR spectra of **1** and **2** before and after thiol–ene "click" reaction, as shown in Figure 4.4. (a) and (b), respectively, verified the disappearance of the vinyl proton resonance (6.49 ppm, labeled as f in Figure 4.4.(a)) and the corresponding appearance of two distinct proton resonances of methoxy (3.33 ppm, labeled as f in Figure 4.4.(b)) and α-protons adjacent to the sulfur

atom (2.78–2.69 ppm, labeled as g^1 and g^2 in Figure 4.4.(b)) in the thio–ether functional group. GPC analysis of **3** clearly showed a peak shift to shorter elution time, relative to **2**, with a monomodal peak having a PDI of 1.07 after thiol–ene "click" reaction (Figure 4.5.).

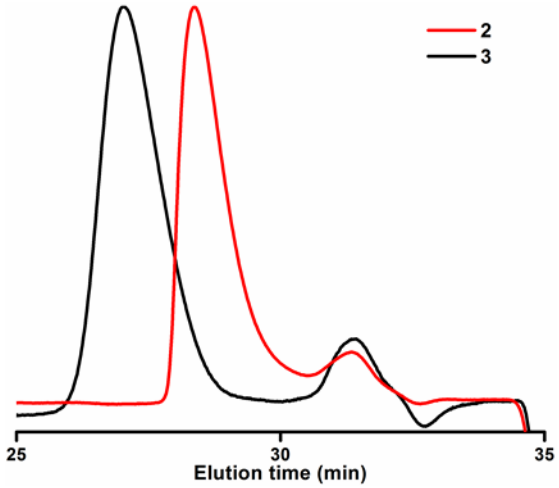

Figure 4.5. GPC traces of 2 and 3, before and after thiol-ene "click" reaction, respectively, as a function of elution time (min).

4.2.4. Acetalization of the Vinyl Ether Side Chain Moieties of PEVEP$_{50}$ 2 with 4-Methylbenzyl Alcohol

Using commercially-available 4-methylbenzyl alcohol and a catalytic amount of *p*-toluenesulfonic acid (PTSA), the presence and chemical availability of vinyl ether moieties of **2** were demonstrated *via* acetalization. Initially, to confirm the integrity of the PPE backbone in the presence of alcohols and strong acidic catalyst, PTSA (pK_a ~ –2.8 (water)), a mixture of **2** and 2 equiv. of 4-methylbenzyl alcohol (relative to the absolute number of vinyl ether bonds) or that of **2** and 0.2 equiv. of PTSA (in relation to

the absolute number of vinyl ether bonds) or that of **2**, 4-methylbenzyl alcohol. and PTSA in *N*,*N*-dimethylformamide-d_7 (DMF-d_7) was allowed to stir for a period of time, as a preliminary control reaction. An aliquot of each reaction solution was collected at a predetermined time, quenched by the addition of an excess of TEA, and then evaluated by ^{31}P NMR spectroscopy. ^{31}P NMR spectra confirmed the intact PPE backbone in the presence of either 4-methylbenzyl alcohol or PTSA for several hours. However, the combination of **2**, 4-methylbenzyl alcohol, and PTSA in the mixture solution was accompanied by undesired degradation/transesterification along the PPE backbone structure after 6 min of reaction, as confirmed by ^{31}P NMR spectroscopy. Accordingly, a scaled-up production of **4** was conducted using the same molar ratio as used for the preliminary control reaction, and the acetalization reaction was quenched at 5 min by the addition of an excess of TEA to ensure the intact PPE backbone structure. With respect to the purification, Hawker *et al.* employed an extraction method to purify their acetal-linked linear poly(ethylene glycol) by using water;[136] however, this extraction method was not compatible with the instability of the PPE backbone in our system. In addition, the complete removal of PTSA and/or 4-methylbenzyl alcohol was not achieved by precipitation of the desired polymer in organic solvent, such as diethyl ether. More importantly, this precipitation method was not desirable, especially for acetal-bearing polymers as a result of the possible cross-linking side reactions by trans-acetalization in the presence of a trace amount of PTSA.[139] Thus, sequential dialysis (MWCO 6–8 kDa) against two different organic solvents, DMF and DCM, was conducted for purification.

Finally, the desired product, **4**, was obtained after removal of the organic solvents, as confirmed by ^{1}H and ^{31}P NMR spectroscopy (Figure 4.4.(c)).

The conversion percentage of vinyl ethers to acetals was calculated from chain-end group analysis by ^{1}H NMR spectroscopy, *i.e.,* by comparison of the integrals of proton resonances of the benzyl group (7.44–7.32 ppm, labeled as a in Figure 4.4.(c)) of the initiated chain end to those of two distinct acetal linkages, methyl (1.33 ppm, labeled as j in Figure 4.4.(c)) and methylene (4.87–4.75 ppm, labeled as i in Figure 4.4.(c)), or 4-methyl protons on the benzyl substituents (2.32 ppm, labeled as m in Figure 4.4.(c)). According to the chain-end analysis by ^{1}H NMR spectroscopy, approximately 18% of the initial vinyl ether groups were converted into the acetal linkages, *ca.* 50% remained intact, and *ca.* 32% of the repeat units carried hydroxyl groups as a result of hydrolysis. The hydrolysis side reaction was probably attributed to a trace of water present in PTSA and/or highly viscous PPE. It is noteworthy that the complete disappearance of vinyl proton resonances was observed with prolonged reaction time (1–2 h), which could have enhanced the acetal conversion percentage. However, quenching the reaction at the optimal time, 5 min according to the preliminary reaction, was essential for the integrity of the PPE backbone. This backbone stability was verified by the existence of one distinct ^{31}P resonance peak at –0.68 ppm, observed by ^{31}P NMR spectroscopy. GPC analysis of **4** was not available in THF because of its polar nature, conferred by the newly formed hydroxyl groups on the side chains.

4.2.5. Thio-acetalization of the Vinyl Ether Side Chain Moieties of PEVEP$_{50}$ 2 with 4-Methylbenzyl Mercaptan

The same reaction protocol for the acetalization reaction was applied to the thio–acetalization of **2**. The ^{1}H NMR spectrum of thio–acetal-bearing PEVEP$_{50}$, **5**, is shown in Figure 4.4.(d). The conversion percentage of vinyl ethers to thio–acetals was calculated from chain-end group analysis by ^{1}H NMR spectroscopy, *i.e.*, by comparisons of the integrals of proton resonances of the benzyl group (7.44–7.32 ppm, labeled as a in Figure 4.4.(d)) of the initiated chain end to those of the two distinct thio-acetal linkages, methyl (1.51 ppm, labeled as j in Figure 4.4.(d)), methylene (4.71 ppm, labeled as i in Figure 4.4.(d)) or 4-methylbenzyl protons (2.31 ppm, labeled as m in Figure 4.4.(d)). By ^{1}H NMR chain-end analysis, approximately 8% of the initial vinyl groups were found to be converted into the thio-acetal linkages, *ca.* 56% of them remained intact, and *ca.* 36% of the repeat units underwent hydrolysis of the side chains to present hydroxyl groups. The intact PPE backbone was affirmed by the presence of one distinct ^{31}P resonance peak at -0.67 ppm, as measured by ^{31}P NMR spectroscopy. Similar to the acetal linkage-bearing polymer, **4**, the polar nature endowed by the newly formed hydroxyl groups on the side chains did not allow for GPC analysis.

4.2.6. Synthesis of the Amphiphilic Diblock Copolymer, α-Methoxy Poly(ethylene glycol)$_{44}$-block-poly(ethylene glycol vinyl ether phosphotriester)$_{33}$ (mPEG$_{44}$-b-PEVEP$_{33}$), 6

Based on the kinetic study of **2**, amphiphilic diblock copolymer, mPEG$_{44}$-*b*-PEVEP$_{33}$, **6**, was prepared by ROP using the molar ratio 100:1:3 of **1**, *α*-methoxy-*ω*-

hydroxy poly(ethylene glycol) 2000 Da ($mPEG_{44}$-OH), and DBU, respectively (Figure 4.6.). The polymerization was quenched at 6 min by the addition of a solution of excess of benzoic acid in DCM, and the desired diblock copolymer product was obtained after sequential dialysis (MWCO 6–8 kDa) against organic solvents, MeOH and DCM. The DP_n calculated based on ^{31}P NMR spectroscopy-determined monomer conversions was in agreement with that calculated from chain-end analysis by ^{1}H NMR spectroscopy, *i.e.*, by comparisons of the integrals of the proton resonance of the methyl group of the initiated chain end (3.33 ppm, labeled as a in Figure 4.7.(a)) to that of the double bond (6.49 or 4.06 ppm, labeled as f or g^2, respectively, in Figure 4.7.(a)) or α- protons to the vinyl ether oxygen atom (3.94–3.86 ppm, labeled as e in Figure 4.7.(a)) of the PEVEP block segment. Additionally, one distinct ^{31}P resonance peak at -0.71 ppm confirmed the intact PEVEP block backbone structure during the chain extension by ROP of **1** and the work-up process of **6**. GPC analysis of **6** showed a distinct peak shift to lower elution time from that of the macroinitiator, $mPEG_{44}$-OH, after polymerization, with a monomodal peak with a PDI of 1.09 (Figure 4.7.(b)).

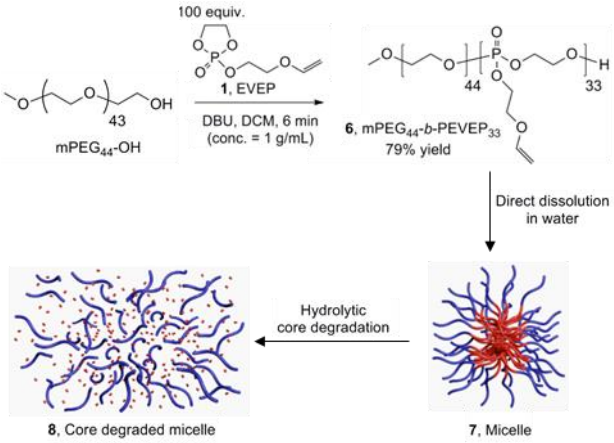

Figure 4.6. Synthetic route for the preparation of amphiphilic diblock copolymer 6 and schematic illustration of the assembly of 6 into micelles 7 by direct dissolution in water followed by the hydrolytic core degradation of 7.

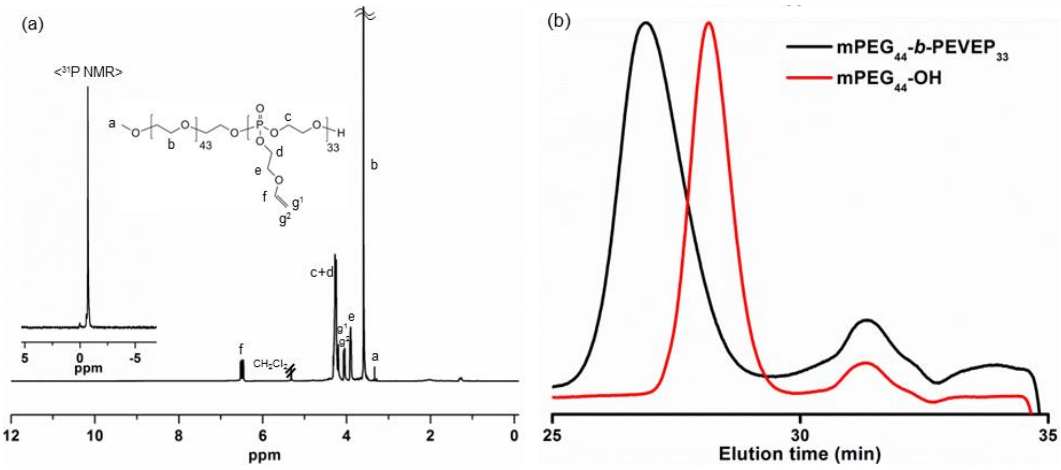

Figure 4.7. (a) ^{1}H (300 MHz, CD_2Cl_2, ppm) and ^{31}P (121 MHz, CD_2Cl_2, ppm, inset) NMR spectra of 6. (b) GPC traces of macroinitiator, $mPEG_{44}$-OH, and diblock copolymer 6, $mPEG_{44}$-*b*-$PEVEP_{33}$, as a function of elution time (min).

4.2.7. Thermal Properties

The T_g values of the prepared polymers varied, as measured by differential scanning calorimetry (DSC), depending on the side chain substituents (Table 4.1.). The conjugation of the 2-(2-methoxyethoxy)ethanethioether groups onto the side chains

induced a decrease of the T_g value from –39 °C of **2** to –64 °C of **3** after the thiol–ene "click" reaction. The slight increase of T_g value of **4** and **5**, –27 and –31 °C, respectively, as compared with that of **2**, –39 °C, was ascribed to the rigidity and π–π interactions of the aromatic rings. Meanwhile, the T_g value of the diblock copolymer with the extended ethylene glycol backbone units, **6**, was complicated to analyze but appeared to give only a single T_g value, similar to that of **2**, –38 °C. In addition, no T_m for the PEG block segment was observed for the diblock system, therefore, an extensive investigation against the homopolymers, $mPEG_{44}$-OH and $PEVEP_{50}$, and a $mPEG_{44}$-OH/$PEVEP_{50}$ blend was conducted. These studies confirmed that the PEVEP block fully suppresses PEG crystallinity in the diblock system; while the physical blend does little to suppress PEG crystallization (full DSC traces for all systems upon heating and cooling are presented with detailed discussions in the Supporting Information (Figure 4.19.)).

Table 4.1. Comparisons of Glass Transition Temperatures, T_g, of the Prepared Polymers, As Measured by Differential Scanning Calorimetry (DSC).

Polymer	T_g (°C)
$PEVEP_{50}$, **2**	–39
$PEVEP_{50}$ after thiol–ene "click" reaction, **3**	–64
$PEVEP_{50}$ after acetalization reaction, **4**	–27
$PEVEP_{50}$ after thio–acetalization reaction, **5**	–31
$mPEG_{44}$-*b*-$PEVEP_{33}$, **6**	–38

4.2.8. Self-Assembly of the Amphiphilic Diblock Copolymer, $mPEG_{44}$-b-$PEVEP_{33}$ 6

The self-assembly behavior of the amphiphilic diblock copolymer, $mPEG_{44}$-*b*-$PEVEP_{33}$ **6**, was studied by direct dissolution in nanopure water. A high concentration of **6** could be dispersed in nanopure water or buffer (>15 mg/mL) without a significant turbidity or precipitation, which allowed for analyses to be performed across a broad range of concentrations and also serves as a promising criterion for its use as a drug delivery carrier. The morphology and surface charge of the resulting micellar nanoparticles, **7**, were characterized by dynamic light scattering (DLS), transmission electron microscopy (TEM), atomic force microscopy (AFM) and ζ-potential measurements (Figure 4.9. and Figure 4.8.). DLS and ζ-potential analyses indicated narrow and monomodal size distributions (PDI = 0.114) with almost neutral charges and

a negligible difference at pH 5.0 and 7.4, –4.52 and –7.64 mV, respectively. The number-averaged hydrodynamic diameter of **7** by DLS was *ca.* 44 ± 6 nm. The TEM images also revealed uniform nanoparticles with an average diameter of 39 ± 5 nm. Although the hydrodynamic and dry-state diameters measured by DLS and TEM, respectively, were in agreement, AFM indicated significant deformation of the micelles upon deposition and drying on the mica substrate. The *ca*. 3 nm height and 40 ± 7 nm diameter indicate flattening of the micelles, which is predicted to occur based upon the fluid shell and core components, each being composed of a highly viscous polymer, PEG (T_g = –17 °C) and PEVEP (T_g = –39 °C, Table 4.1. and Figure 4.19.). The AFM data are useful qualitatively; however, further quantitative analysis is complicated by the presence of substantial amounts of polymer debris and agglomerations of **7** across the substrate (Figure 4.9.(c) and (d)), which are also indicators of the fluidity of the micellar assemblies.

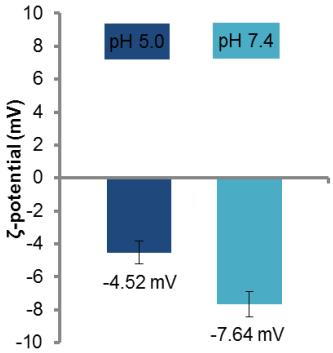

Figure 4.8. ζ-Potential values of 7 in acetate buffer solutions at pH 5.0 and in MOPS buffer solutions at pH 7.4. The average values and their standard deviations, from three measurements, are shown.

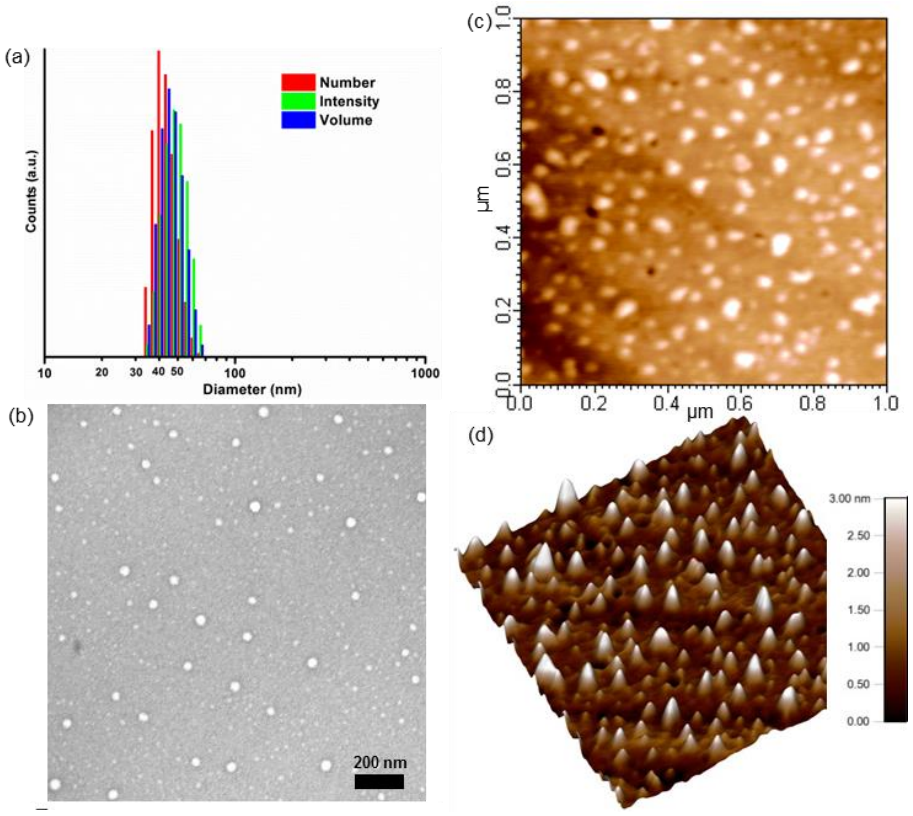

Figure 4.9. Self-assembly results of micelle 7 in water. (a) DLS results of 7: $D_{h(intensity)}$ = 49 ± 7 nm, $D_{h(volume)}$ = 46 ± 7 nm, and $D_{h(number)}$ = 44 ± 6 nm (PDI = 0.114). (b) TEM image of 7: D_{av} = 39 ± 5 nm, after counting more than 150 nanoparticles. AFM height image (c) and three-dimensional image (d) of 7: D_{av} = 40 ± 7 nm, after counting more than 100 nanoparticles.

4.2.9. Degradation Study

The phosphoester linkages of PPEs can be cleaved by spontaneous hydrolysis and/or enzymatic degradation; the hydrolysis rate of the phosphoester linkages is known to be highly pH-dependent.[42,104,106,145-147] In this study, we postulated that the exposure of micelles, **7**, in acidic aqueous environment would induce a dual degradation of the phosphoester backbone linkages and the vinyl ether side chain moieties of the PEVEP block segment. Hence, the stability of the phosphoester backbone linkage and the vinyl

ether functionality of **7** were monitored in deuterated buffer solutions by ^{31}P and ^{1}H NMR spectroscopies, respectively, in parallel to measuring the micelle size and the intensity by DLS. Furthermore, the collected degradation products were identified using electrospray ionization (ESI), gas chromatography (GC), and matrix-assisted laser desorption/ionization time-of-flight (MALDI-TOF) mass spectrometry.

4.2.10. Degradability of the PEVEP Backbone in Aqueous Solutions, As Monitored by ^{31}P NMR Spectroscopy

The backbone stability of the PEVEP segment in D_2O at pH values of 5.0 and 7.4 and temperature of 37 °C was monitored by ^{31}P NMR spectroscopy (Figure 4.10.). The integral ratio of the ^{31}P resonance of the intact PEVEP segment at –0.71 ppm to that of the newly emerging peaks was analyzed. The pH-dependent degradation of the PEVEP backbone linkages became apparent by the disappearance of ^{31}P resonance corresponding to the intact PEVEP backbone, coincident with the appearance of new ^{31}P resonances as a result of hydrolytic degradation at pH 5.0, whereas there was no significant change in the PEVEP ^{31}P resonance when the samples were incubated at pH

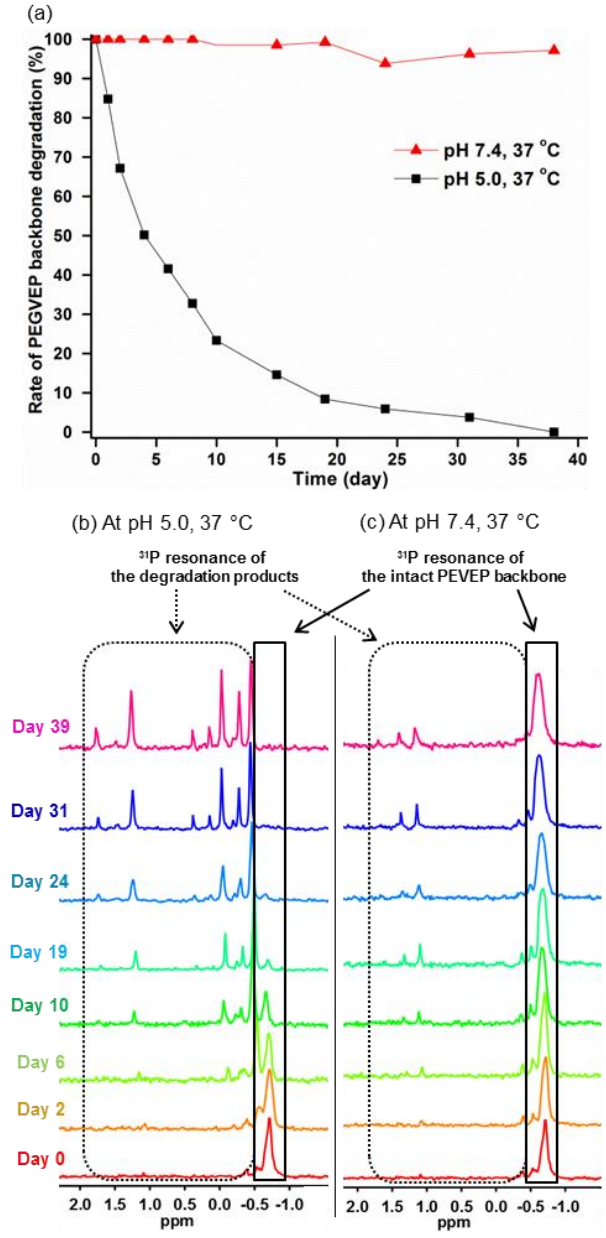

Figure 4.10. (a) Rate of the PEVEP backbone degradation of 7 at pH 5.0 (black line) or pH 7.4 (red line) at 37 °C as a function of time, as measured by a comparison of the integrals of initial to the newly appeared ^{31}P NMR resonances. Changes in the ^{31}P NMR resonance of PEVEP backbone of 7 at pH 5.0 (b) and 7.4 (c) at 37 °C over a period of time.

4.2.11. Stability of the Vinyl Ether Side Chain Moieties in Aqueous Solutions, As Monitored by ^{1}H NMR Spectroscopy

To compensate for potential complications in the detection of vinylic proton resonances of the micelle core, we evaluated the pH-dependent hydrolytic reactivity of the vinyl ether functionalities by observing both the polymer side chain functionalities and the small molecule hydrolysis product using ^{1}H NMR spectroscopy. To determine the reactivity of the acid-labile vinyl ether functionality, the integral ratio of a distinct vinyl proton resonance of the micelles at 6.49 ppm to the newly appeared proton resonance of acetaldehyde, one of the hydrolysis products of the vinyl ether functionality, at 9.60 ppm was compared in D_2O at pH values of 5.0 and 7.4 at 37 °C over a period of time (Figure 4.11.). For the micellar nanoparticles in pH 5.0 aqueous solution at 37 °C, both the gradual disappearance of vinyl proton resonance intensity and the appearance of an acetaldehyde proton resonance signal were clearly observed within 1 day, and the equal ratio of these two different proton resonances was reached after 14 days. By contrast, the vinyl proton resonance of the micelles in pH 7.4 aqueous solution at 37 °C remained consistent without any observable generation of acetaldehyde over 39 days. Indeed, this observation bolstered our hypothesis that the spontaneous cleavage of the vinyl ether moieties occurred in pH 5.0 aqueous solution simultaneously with the PPE backbone degradation, but not at pH 7.4.

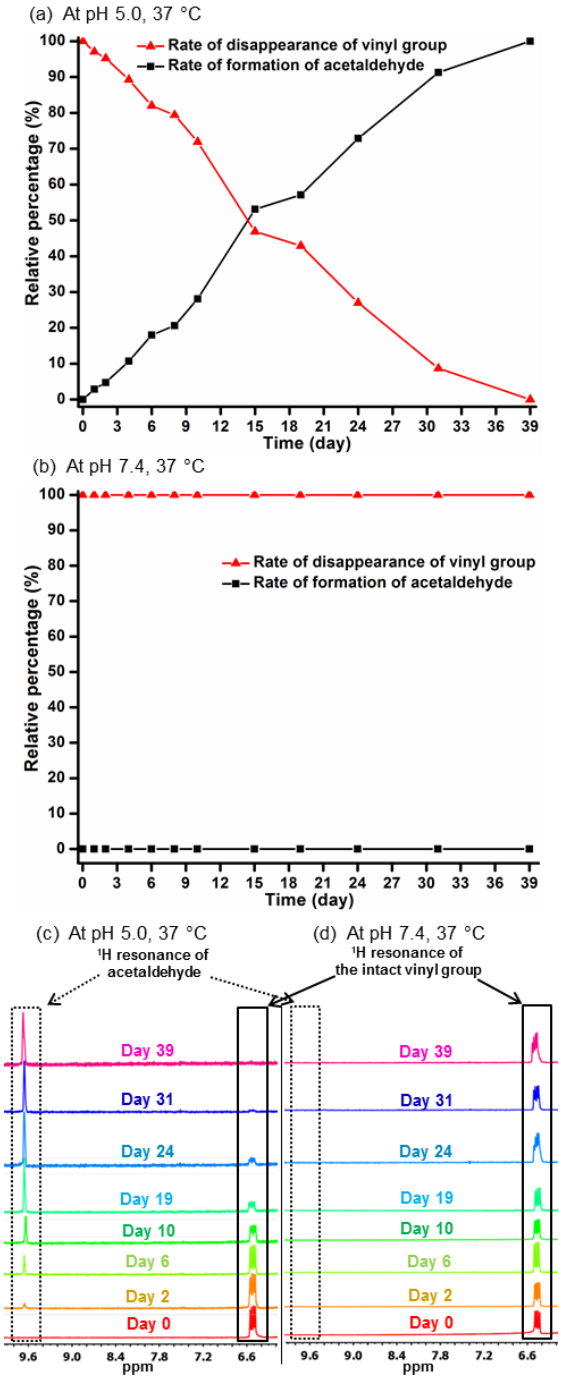

Figure 4.11. Rate of formation of acetaldehyde or disappearance of vinyl proton resonance at pH 5.0 (a) and pH 7.4 (b) and at 37 °C as a function of time, as measured by a comparison of the integrals of vinyl and acetaldehyde proton resonance. Transition of proton resonances of acetaldehyde and vinyl groups at pH 5.0 (c) or pH 7.4 (d) and at 37 °C over a period of time.

4.2.12. Hydrolytic Micelle Stability in Water by Monitoring the Changes in (1) Hydrodynamic Diameter and (2) the Intensity of Light, Scattered by Micelles 7, As Measured by DLS

It was hypothesized that hydrolysis of the PPE backbone would decrease the proportion of the hydrophobic:hydrophilic block segment ratio and that hydrolysis of the side chain vinyl ether groups would increase the hydrophilicity of the PPE backbone; thereby, each would weaken the micelle assemblies. In order to demonstrate the effects of pH-dependent hydrolytic degradation of the polymer on the behavior and stability of the micelles, **7**, aqueous buffer solutions containing **6** at pH 5.0 and 7.4 were incubated at 25 and 37 °C, and their degradation profiles were assessed by measuring the changes in hydrodynamic diameter and the intensity of light, scattered by micelles, when measured by DLS over a period of time (Figure 4.12.). Overall, as predicted from the NMR degradation studies, the micelle assemblies in pH 5.0 aqueous solutions, at both 25 and 37 °C, became unstable within 1 day, and the nanoparticles were undetectable within 7 and 2 days, respectively. The swelling behavior of the micelles upon hydrolysis of PEVEP segment was accounted for by the diffusion of water into the core region (Figure 4.12.(a)). Interestingly, the unstable and dissociated micelles did not cause the formation of visible precipitates, and thus, the micelle solutions remained clear during monitoring. Also, in agreement with the lack of backbone or side chain hydrolysis observed by NMR spectroscopy, the nanoparticle sizes in pH 7.4 aqueous solutions at 25 °C remained consistent over 39 days (Figure 4.12.(b)). Surprisingly, when the samples were incubated at pH 7.4 and 37 °C, large aggregates formed after 20 days, which

persisted until day 43 when particles were no longer detectable. The lack of changes in the NMR data over the same period of time and conditions suggests that transesterification reactions may be a possible chemical change that produced subsequent morphological changes. In accordance with these observations, the intensity of light, scattered by the nanoparticles, as measured by DLS, was also dependent on the pH of water and temperature (Figure 4.12.(c)). In the case of nanoparticles in pH 5.0 aqueous solutions, both at 25 and 37 °C, the signal intensities became weaker rapidly, reaching below 20% as compared to the initial intensity, and finally were undetectable within a week. The signal intensity of light scattered by micelles in pH 7.4 aqueous solution at 37 °C decreased gradually over a period of month. Meanwhile, there was no significant change in the signal intensity for the micelles in pH 7.4 aqueous solution at 25 °C throughout the monitoring period. Taken together, the acidity of solutions was the primary determinant of the micelle stability.

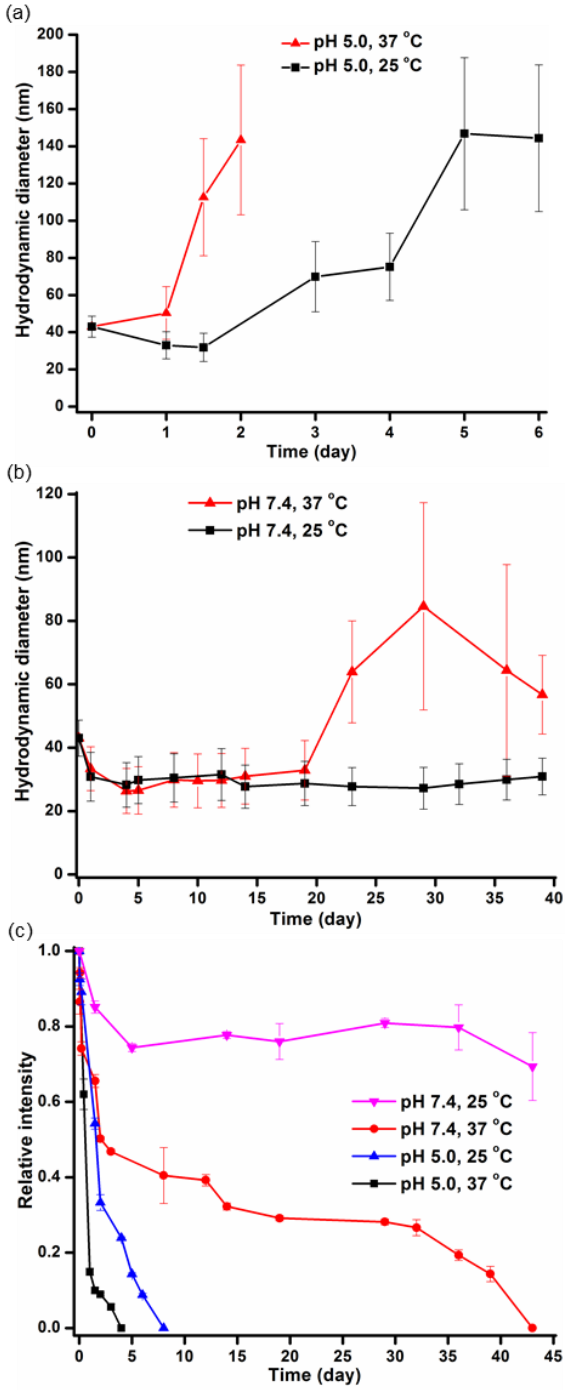

Figure 4.12. Study of the micelle stability by using DLS. Changes in the hydrodynamic diameter of micelles at pH 5.0 (a) or pH 7.4 (b) and at a temperature of 25 °C (black line) or 37 °C (red line) over a period of time. (c) Changes in the relative intensity of micelles in different environments, pH and temperature, over a period of time. The average values and their standard deviations, from three measurements, are shown.

4.2.13. Identification of the Degradation Products by ESI, GC and MALDI-TOF Mass Spectrometry

There have been several reports where the hydrolytic or enzymatic degradation behavior of PPE-containing micelles were studied by using titration,[104] NMR spectroscopy,[42,104] GPC,[106,145-147] and/or DLS[144] methods; however, to the best of our knowledge, the identification of the actual degradation products of PPE has not been performed directly. In this study, we successfully identified the degradation products of PPE qualitatively using electrospray ionization (ESI), gas chromatography (GC), and matrix-assisted laser desorption/ionization time-of-flight (MALDI-TOF) mass spectrometry. For this study, nanoparticles in aqueous solution at pH 5.0 were incubated at 37 °C until they were not detectable by DLS, and the complete disappearance of ^{31}P resonance signal from the intact PEVEP backbone was confirmed by ^{31}P NMR spectroscopy. The mixture solution containing the degradation products was analyzed by using ESI, GC, and MALDI-TOF MS.

The presence of oligomers and phosphoric acids was confirmed by ESI MS (Figure 4.13.), demonstrating the hydrolytic degradability of phosphoester linkages of PPE. Tandem mass spectrometry was performed on most of the precursor ions as a way of verifying the chemical structures of these ions. The MS/MS product ions are listed along with the structures in Figure 4.13.

Two series of oligomers (f and g series) that differ by 44 Da were observed (Figure 4.13.). In order to verify that the f series were not the fragments of the g series, *i.e.*, by losing vinyl alcohol (*m/z* 44), MS/MS of the lower mass precursor ions *m/z* 309

and 353 were performed (Figure 4.14. and 4.15.). The predominant fragment ion for *m/z* 309 was 141 while that for *m/z* 353 was 185, thus both losing a neutral repeating unit, 168. In addition, a loss of ethylene glycol was observed for both ions. However, unlike the precursor ion *m/z* 353, *m/z* 309 lost vinyl dihydrogen phosphate to produce ion e. This major difference implied that the end group of the f series oligomers is 2-hydroxyethyl dihydrogen phosphate, while that of g series oligomers is bis(2-hydroxyethyl) hydrogen phosphate. Therefore, the f series were not the fragment ions from the g series.

Because of its unionizable nature by electrospray ionization, the presence of ethylene glycol, as one of the degradation products, was confirmed by GC MS with electron ionization (EI) (Figure 4.16.). Neither vinyl- nor vinyl ether-containing compounds were detected using GC MS, which agreed with our observation by ^{1}H NMR spectroscopy, shown in Figure 4.11. Again, this absence of vinyl or vinyl ether functionalities within the degradation products substantiated our hypothesis of a simultaneous hydrolysis of the vinyl ether moieties during the degradation process of the PPE backbone. Finally, MALDI-TOF MS analysis of the mixture of the degradation products verified the presence of the intact PEG block segment with a single distribution having a spacing of 44 Da, corresponding to a PEG repeat unit (Figure 4.17.).

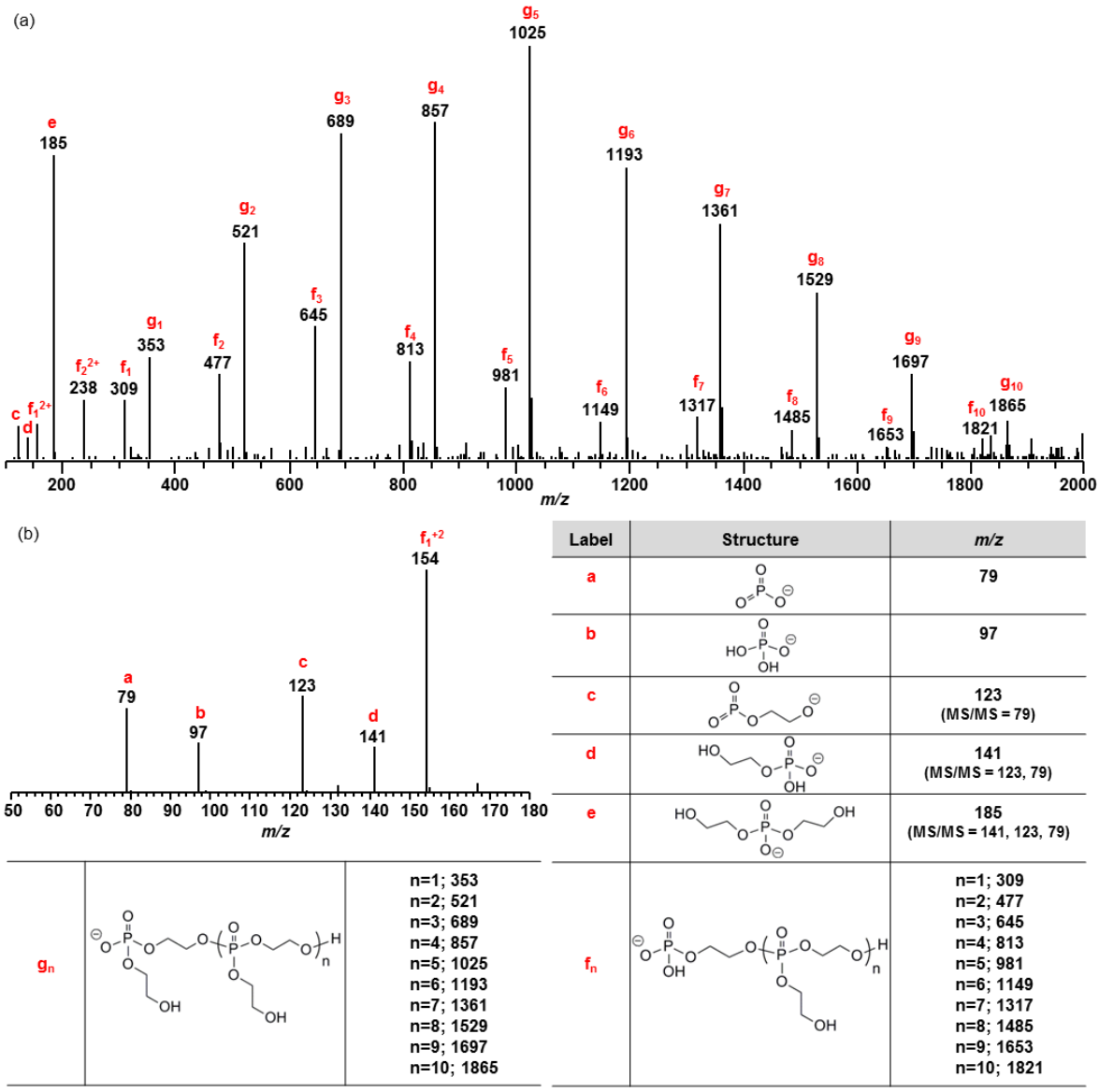

Figure 4.13. ESI MS analysis of the degradation products of 8. Mass spectra in negative ion mode; *m/z* range of 100–2000 (a) and 50–180 (b). See Figures 4.14. and 4.15. for MS/MS spectra of f_1 and g_1.

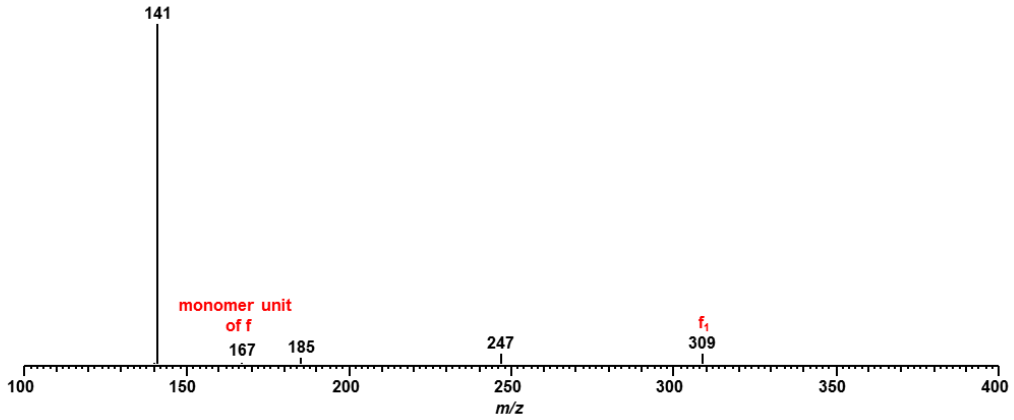

Figure 4.14. MS/MS spectrum of *m/z* 309.

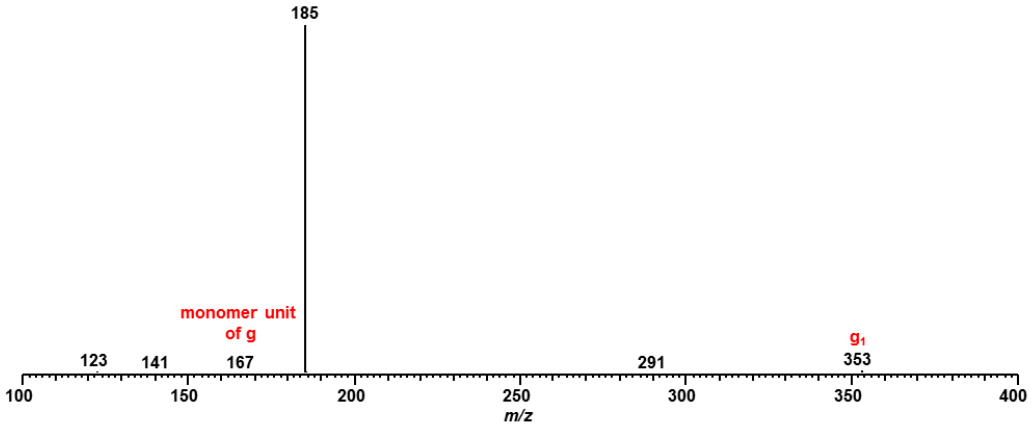

Figure 4.15. MS/MS spectrum of *m/z* 353.

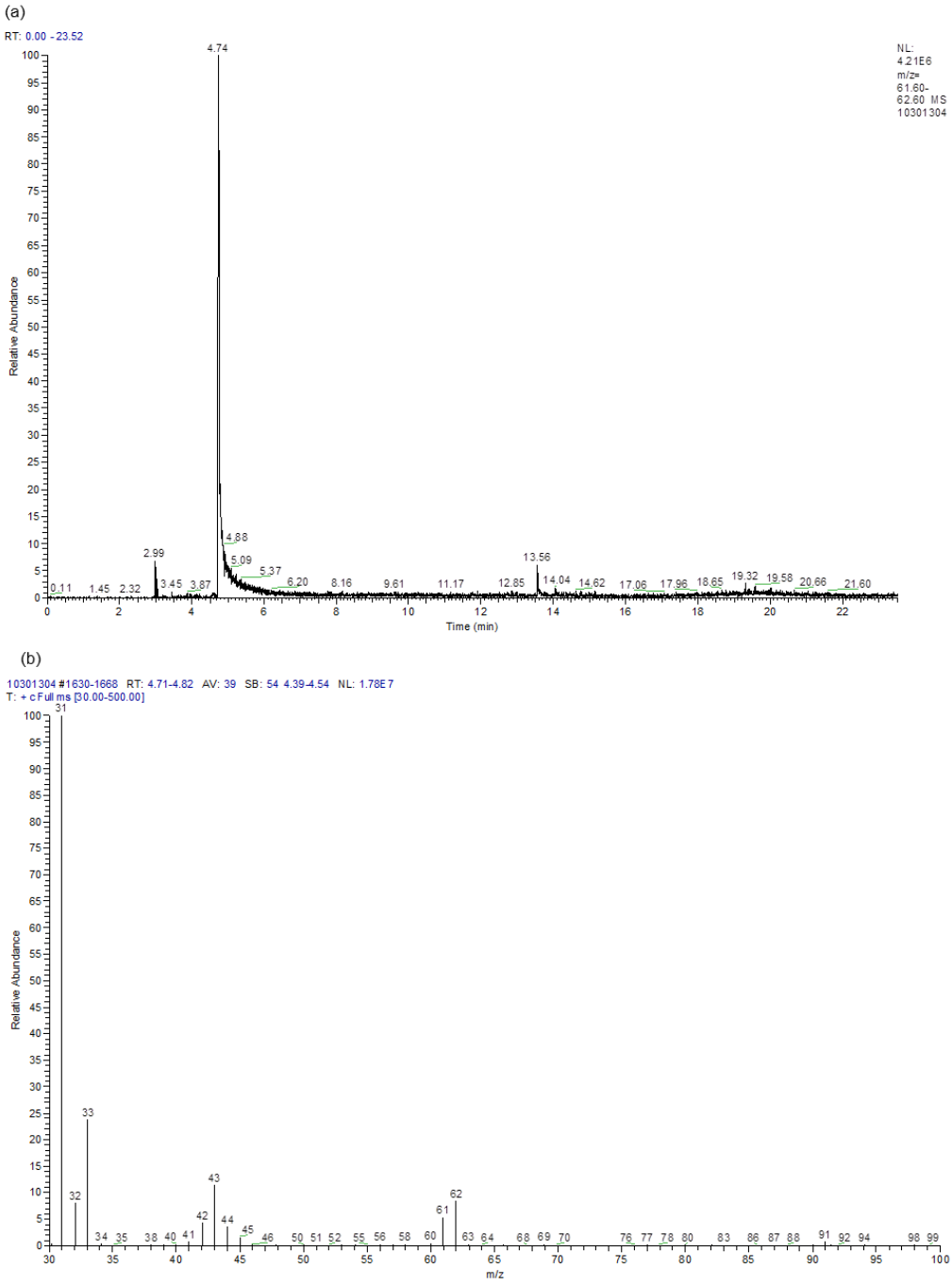

Figure 4.16. GC MS analysis of the degradation products of 8. (a) Extracted ion chromatogram at *m/z* 62. (b) EI MS at retention time 4.74 min.

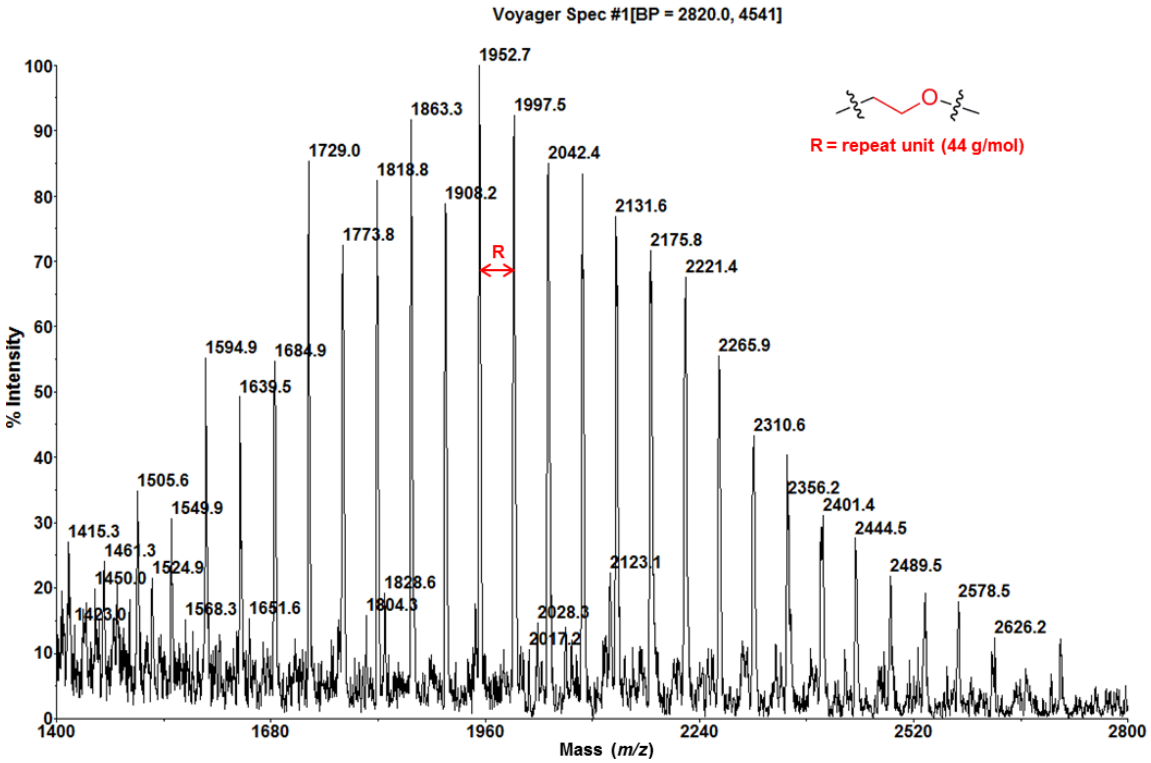

Figure 4.17. MALDI-TOF MS spectrum of the degradation products of 8.

4.2.14. Cytotoxicity of Micelles of mPEG$_{44}$-b-PEVEP$_{33}$ 7 and Their Degradation Products 8

The cytotoxicities of the parent micelles, **7**, and their degradation products, **8**, were evaluated toward two cell lines, RAW 264.7 mouse macrophages and OVCAR-3 human ovarian adenocarcinoma cells at a concentration range from 3 to 3000 µg/mL for 24 h (Figure 4.18.). Both **7** and **8** maintained high cell viability over the range of the tested concentrations in both cell lines. We have previously observed low cytotoxicity and immunotoxicity of PPE-based micelles with different surface charges, their shell cross-linked analogs and their degradation products even though we were not able to identify the degradation products at that time.[97] These PPE-based nanoparticles are

expected to have broad implications in clinical nanomedicine as alternative vehicles to those involved in several of the currently available medications, with precise control over their molecular structures and overall architectures.

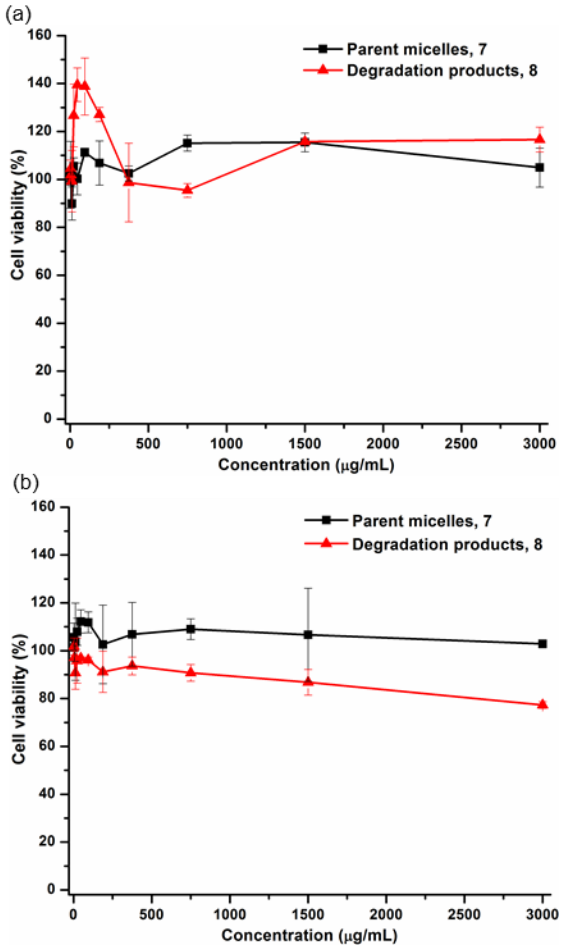

Figure 4.18. Cytotoxicity of the parent micelles of $mPEG_{44}$-*b*-$PEVEP_{33}$ 7 (black line) and their degradation products 8 (red line) at a concentration range of 3–3000 μg/mL for 24 h in RAW 264.7 mouse macrophages (a) and OVCAR-3 human ovarian adenocarcinoma cells (b).

4.2.15. Additional Thermal Studies Regarding the Suppression of the Crystallinity of PEG in mPEG$_{44}$-b-PEVEP$_{33}$

Since the ability of the PEVEP block segment to suppress the crystallization of PEG was unexpected, additional experiments were conducted to confirm the finding by contrasting the mPEG$_{44}$-*b*-PEVEP$_{33}$ diblock behavior to two analogous homopolymers, mPEG$_{44}$-OH and PEVEP$_{50}$, and an equimolar physical blend of mPEG$_{44}$-OH and PEVEP$_{50}$. Furthermore, we present these studies in contrast to liquid nitrogen crash-cooled (CC) samples of mPEG$_{44}$-OH, mPEG$_{44}$-*b*-PEVEP$_{33}$ and the mPEG$_{44}$-OH/PEVEP$_{50}$ blend (Figure 4.19.), in order to kinetically capture PEG domains in an amorphous state and enhance the ability to observe PEG T_g values. Looking at the T_m region for PEG in the mPEG$_{44}$-*b*-PEVEP$_{33}$ and mPEG$_{44}$-OH/PEVEP$_{50}$ blend samples, for both crash-cooled and ambient-cooled samples, it was clear that (regardless of the cooling rate) the PEVEP block completely suppresses the crystallization of PEG for the diblock copolymer system and that the blend still expresses a high degree of PEG crystallinity. This result made a strong case for the diblock structure being critical to the observed suppression of PEG crystallization, not merely an effect of the presence of PEVEP. When crash-cooled, the mPEG$_{44}$-OH sample presented T_g at *ca.* -17 °C, the crash-cooled mPEG$_{44}$-OH/PEVEP$_{50}$ blend displayed a minor transition in the same range, however, the mPEG$_{44}$-*b*-PEVEP$_{33}$ diblock showed an uncertain fluctuation of the baseline over the broad range from -20 to +30 °C, which complicated the analysis and prevented determination of whether there may be amorphous PEG-rich domains in the diblock sample that were capable of exhibiting a glass transition. Comparison of the

$PEVEP_{50}$, $mPEG_{44}$-*b*-$PEVEP_{33}$ and blend samples over the -40 to -25 °C range indicated a virtually identical heat curve for T_g of PEVEP at *ca.* -35 °C.

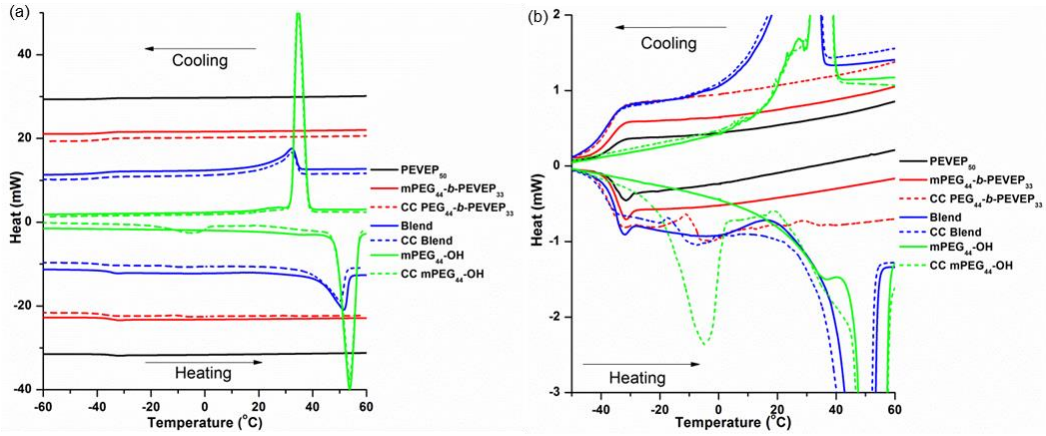

Figure 4.19. DSC traces for $mPEG_{44}$-OH, $PEVEP_{50}$, $mPEG_{44}$-*b*-$PEVEP_{33}$ and a physical mixture of $mPEG_{44}$-OH and $PEVEP_{50}$. The crash-cooling (CC) samples are those which were crash-cooled from 100 °C into liquid nitrogen before heating. (a) Trace over the region of interest (-60–60 °C) for the system, offset to increase clarity. (b) Rescaled trace (-50–60 °C) to contrast the glass transition regions for all samples.

4.3. Experimental Section

4.3.1. Materials

Ethylene glycol vinyl ether (EVE), 2-(2-methoxyethoxy)ethanethiol, 2,2-dimethoxy-2-phenylacetophenone (DMPA), diethyl ether, triethylamine (TEA), methanol (MeOH) and benzoic acid were used as received from Sigma-Aldrich Company or TCI America. 2-Chloro-2-oxo-1,3,2-dioxaphospholane (COP) was used as received from Thermo Fisher Scientific Inc. Benzyl alcohol (BnOH), 1,8-diazabicyclo[5.4.0]undec-7-ene (DBU), 4-methylbenzyl alcohol, 4-methylbenzyl mercaptan were purchased from Sigma-Aldrich Company, and they were distilled from

calcium hydride prior to use. *p*-toluenesulfonic acid monohydrate (PTSA) was purchased from Sigma-Aldrich Company, and it was dried by azeotropic distillation in toluene three times prior to use. α-Methoxy-ω-hydroxy poly(ethylene glycol) 2,000 Da ($mPEG_{44}$-OH) was purchased from Rapp Polymere, and it was dried by azeotropic distillation in toluene three times prior to use. The dried benzyl alcohol, DBU, 4-methylbenzyl alcohol, 4-methylbenzyl mercaptan, PTSA and $mPEG_{44}$-OH were stored in an argon-filled glovebox until use. Dichloromethane (DCM) and *N*,*N*-dimethylformamide (DMF) were dried through columns (J. C. Meyer Solvent Systems, Inc.). Spectra/Pro® membranes (MWCO 6–8 kDa, Spectrum Medical Industries, Inc., Laguna Hills, CA) were used for dialysis. RAW 264.7 and OVCAR-3 cell lines, as well as RPMI and DMEM media were purchased from the American Type Culture Collection. Media additives (fetal bovine serum, penicillin/streptomycin) were purchased from Sigma Aldrich Company. The cell culture 96-well flat bottom plates were purchased from Corning Costar Co. The CellTiter 96 non-radioactive cell proliferation assay was obtained from Promega Co.

4.3.2. Characterization Methods

^{1}H, ^{13}C, and ^{31}P NMR spectra were recorded on Inova 300 MHz spectrometers interfaced to a UNIX computer using VnmrJ software. Chemical shifts were referenced to solvent resonance signals. For ^{31}P NMR spectroscopy, phosphoric acid (85 wt. % in H_2O) at 0 ppm was used as an external standard. IR spectra were recorded on an IR Prestige 21 system (Shimadzu Corp.) and analyzed by using the IRsolution software.

The polymer molecular weight and molecular weight distribution were determined by Gel Permeation Chromatography (GPC). The GPC was conducted on a Waters 1515 HPLC (Waters Chromatography, Inc.) equipped with a Waters 2414 differential refractometer, a PD2020 dual-angle (15° and 90°) light scattering detector (Precision Detectors, Inc.), and a three-column series (PL gel 5 μm Mixed C, 500 Å, and 104 Å, 300 × 7.5 mm columns; Polymer Laboratories, Inc.). The system was equilibrated at 40 °C in THF, which served as the polymer solvent and eluent with a flow rate of 1.0 mL/min. Polymer solutions were prepared at a known concentration (3–5 mg/mL) and an injection volume of 200 μL was used. Data collection and analysis were performed with Precision Acquire software and Discovery 32 software (Precision Detectors, Inc.), respectively.

Glass transition temperatures (T_g) were measured by differential scanning calorimetry (DSC) on a Mettler-Toledo DSC822® (Mettler-Toledo, Inc., Columbus, OH), with a heating rate of 10 °C/min. Measurements were analyzed by using Mettler-Toledo Star^e v. 7.01 software. The T_g was taken as the midpoint of the inflection tangent, upon the second heating scan. Thermogravimetric analysis (TGA) was performed under N_2 atmosphere using a Mettler-Toledo model TGA/SDTA851e, with a heating rate of 5 °C/min and cooling rate of 5 °C/min. Measurements were analyzed by using Mettler-Toledo Star^e v. 7.01 software.

Dynamic light scattering (DLS) measurements were conducted using Delsa Nano C (Beckman Coulter, Inc., Fullerton, CA) equipped with a laser diode operating at 658 nm. Size measurements were made in nanopure water (n = 1.3329, η = 0.890 cP at 25 ±

1 °C). Scattered light was detected at 165° angle and analyzed using a log correlator over 70 accumulations for a 3.0 mL sample in a glass sizing cell (4.0 mL capacity). The samples in the glass sizing cell were equilibrated for 30 minutes before measurements were made. The photomultiplier aperture and the attenuator were automatically adjusted to obtain a photon counting rate of *ca.* 10 kcps. Calculation of the particle size distribution and distribution averages was performed using CONTIN particle size distribution analysis routines. The peak averages of histograms from number distributions out of 70 accumulations were reported as the average diameters of the particles.

The zeta potential values of the nanoparticles were determined by Delsa Nano C particle analyzer (Beckman Coulter, Fullerton, CA) equipped with a 30 mW dual laser diode (658 nm). The zeta potential of the particles in suspension was obtained by measuring the electrophoretic movement of charged particles under an applied electric field. Scattered light was detected at a 30° angle at 25 °C. The zeta potential was measured at five regions in the flow cell and a weighted mean was calculated. These five measurements were used to correct for electroosmotic flow that was induced in the cell due to the surface charge of the cell wall. All determinations were repeated three times.

Transmission electron microscopy (TEM) images were collected on a JEOL 1200EX operating at 100 kV and micrographs were recorded at calibrated magnifications using a SIA-15C CCD camera. The samples as aqueous solutions (5 µL) were deposited onto carbon-coated copper grids. Excess sample was wicked off using

filter paper and the grids were allowed to dry in the air for 1 min. Following this, the grids were stained with 5 µL of a 2% uranyl acetate aqueous solution. Excess stain was wicked off by using filter paper after 20 seconds. The sample grids were dried under vacuum overnight before analysis.

Atomic force microscopy (AFM) imaging was performed by using a MFP-3D system (Asylum Research) using a standard silicon probe (VISTAprobes, resonance constant: 62 kHz, tip radius: 15 nm, spring constant: 3 N/m). For AFM sample preparation, the sample was dissolved in nanopure water at 0.25 mg/mL and 20 µL of the sample was spin coated onto a glass coverslip. All AFM samples were stored at room temperature under vacuum prior to use.

Electrospray ionization (ESI) in negative ion mode was carried on a quadruple ion trap mass spectrometer (LCQ-DECA, ThermoFinnigan, San Jose, CA). The sample was directly infused at a flow rate of 6 µL/min. The spray voltage was set at -4.5 kV. Sheath gas and auxiliary gas flow rates were 50 and 10 arbitrary units, respectively. Transfer capillary temperature was held at 250 °C. MS/MS experiments were performed on the same instrument at a relative collision energy of 30−32%. Xcalibur 2.0 software package (ThermoFinnigan) was used for data acquisition and processing.

Gas chromatography-mass spectrometry (GC-MS) was performed on Ultra GC/DSQ (ThermoElectron, Waltham, MA). Chromatography was carried out using an Rxi-5ms column (60 m × 0.25 mm with 0.25 µm film thickness) (Restek; Bellefonte, PA). Helium was used as a carrier gas at constant flow of 1.5 mL/min. GC inlet was held at 225 °C while transfer line and ion source were held at 250 °C. An aliquot of 1

μL of sample was injected in splitless mode. The oven temperature was maintained at 50 °C for 5 min and raised to 320 °C at 20 °C/min. Electron impact ionization at 70eV was used for ionization and mass spectra were acquired in full scan mode in the range of 30-500 m/z.

Matrix assisted laser desorption ionization (MALDI) experiments were performed on a Voyager DE-STR mass spectrometer (Applied Biosystems, Foster City, CA) under optimized conditions in positive linear mode. Ions were generated by a pulsed nitrogen laser at 337 nm and accelerated through 25 kV. 100 laser shots were used per spectrum. Trans-2-[3-(4-*t*-butyl-phenyl)-2-methyl-2-propenylidene] malononitrile (DCTB) and potassium trifluoroacetate (KTFA) were used as a matrix and cationization reagent, respectively. The sample, KTFA, and matrix were prepared at concentration of 1, 10 and 20 mg/mL respectively. The sample solution was mixed with the matrix and KTFA at a volume ratio of 1:5:1. About 0.5 μL of this mixture was deposited on a stainless steel sample holder. After air-dried, the sample was analyzed using MALDI TOF MS.

4.3.3. Synthesis of Monomer, 2-Ethylene glycol vinyl ether-1,3,2-dioxaphospholane 2-oxide (EVEP)

A solution of COP (5.0026 g, 35.11 mmol) in 10 mL of anhydrous DCM was added dropwise to a stirred solution of EVE (3.0908 g, 35.08 mmol) and TEA (4.89 mL, 3.55 g, 35.1 mmol) in 50 mL of anhydrous DCM at 4 °C. The reaction mixture was allowed to stir for 12 h at 4 °C and then for 30 min at rt. The precipitate was filtered off, and the filtrate was concentrated under reduced pressure. Diethyl ether (200 mL) was

then added to precipitate the remaining triethylammonium chloride. After the removal of the precipitates by filtration and the solvent *in vacuo*, the clear viscous liquid EVEP was collected (5.13 g, 76% yield). IR: 3045–2800, 1622, 1500–1432, 1368, 1285, 1198, 1070, 1024, 993, 926, 835, 764 cm^{-1}. ^{1}H NMR ($CDCl_3$, ppm): δ 6.44 (dd, J = 14.4 Hz, J = 6.9 Hz, 1H, CH_2OCHCH_2), 4.46–4.26 (m, 6H, $POCH_2CH_2OP$ and $POCH_2CH_2OCHCH_2$), 4.16 (dd, J = 14.4 Hz, J = 2.4 Hz, 1H, $CH_2OCHCHH$), 4.01 (dd, J = 6.9 Hz, J = 2.4 Hz, 1H, $CH_2OCHCHH$), 3.86 (m, 2H, $POCH_2CH_2OCHCH_2$). ^{13}C NMR ($CDCl_3$, ppm): δ 151.3, 87.3, 66.8 (d, J = 23.4 Hz), 66.6 (d, J = 24.3 Hz), 66.1 (d, J = 10.2 Hz). ^{31}P NMR ($CDCl_3$, ppm): δ 17.91. +ESI MS: calculated $[M+H]^+$ for $C_6H_{11}O_5P$: 195.0422, found: 195.0419.

4.3.4. Kinetic Study of the Homopolymerization of EVEP via ROP by Using an Organocatalyst, DBU

In a glovebox, a solution of EVEP (1.0050 g, 5.18 mmol) and benzyl alcohol (5.34 µL, 5.58 mg, 0.052 mmol) in anhydrous DCM (1.0 mL) was placed in a flamed-dried 5 mL shell vial with a magnetic stir bar. DBU (23.1 µL, 23.5 mg, 0.15 mmol) was added into the mixture solution. 70 µL of samples were extracted at 1, 2, 3, 4, 5, 7, 9, 11, 13, 15, and 18 min and quenched immediately by adding a solution of benzoic acid (excess). Conversion of monomer to polymer was calculated by ^{31}P NMR spectroscopy. A portion of the collected samples was purified by precipitation in diethyl ether twice and dried *in vacuo* before injection into the THF GPC to obtain the number average molecular weight, M_n, and polydispersity index, PDI.

4.3.5. Synthesis of Homopolymer, Poly(ethylene glycol vinyl ether phosphotriester)$_{50}$ (PEVEP$_{50}$)

In a glovebox, a solution of EVEP (1.9991 g, 10.30 mmol) and benzyl alcohol (10.7 µL, 11.2 mg, 0.10 mmol) in anhydrous DCM (2.0 mL) was placed in a flamed-dried 5 mL shell vial with a magnetic stir bar. DBU (46.2 µL, 47.0 mg, 0.31 mmol) was added into the mixture solution. After 9 min of stirring, the reaction was quenched immediately by adding a solution of benzoic acid (excess). The product was dialyzed (MWCO 6–8 kDa) in MeOH followed by DCM overnight. A viscous liquid was collected after removal of the solvent *in vacuo* (0.5588 g, 56% yield). GPC (THF): M_n = 4040 g/mol, PDI = 1.05. IR: 3700–3300, 3025–2825, 1622, 1454, 1425–1350, 1323, 1269, 1198, 1022, 964, 812 cm^{-1}. ^{1}H NMR (CD_2Cl_2, ppm): δ 7.43–7.34 (m, 5H, aromatic ring), δ 6.49 (dd, *J* = 14.4 Hz, *J* = 6.9 Hz, 50H, $CH_2OC\mathit{H}CH_2$), 5.08 (d, *J* = 8.1 Hz, 2H, $POC\mathit{H}_2Ar$), 4.34–4.15 (broad, 350H, $POC\mathit{H}_2C\mathit{H}_2OP$, $POC\mathit{H}_2CH_2OCHCH_2$ and $CH_2OCHC\mathit{H}H$), 4.06 (broad dd, *J* = 6.9 Hz, *J* = 2.1 Hz, 50H, $CH_2OCHCH\mathit{H}$), 3.94–3.86 (broad t, 100H, $POCH_2C\mathit{H}_2OCHCH_2$). ^{13}C NMR ($CD_2Cl_2$, ppm): δ 151.9, 129.1, 128.6, 87.7, 67.4 (d, *J* = 28.2 Hz), 67.2–66.6 (m). ^{31}P NMR (CD_2Cl_2, ppm): δ -0.68. DSC: (T_g) = -39 °C. TGA in N_2: 225 °C, 10% mass loss; 245 °C, 10% mass loss; 285 °C, 22% mass loss; 48% mass remaining above 285 °C.

4.3.6. Thiol-ene "Click" Reaction of Vinyl Ether Side Chain Moieties of PEVEP$_{50}$ with 2-(2-Methoxyethoxy)ethanethiol

A solution of PEVEP$_{50}$ (0.3003 g, 0.035 mmol), 2-(2-methoxyethoxy)ethanethiol (0.6 mL, 0.6 g, 4 mmol), and DMPA (0.2302 g, 0.898 mmol) in 10 mL of MeOH was

irradiated under UV irradiation (365 nm, 6 W) for 1 h while being stirred. The reaction mixture was purified by precipitated in diethyl ether twice and dialysis (MWCO 6–8 kDa) in MeOH followed by DCM overnight. A viscous liquid was collected after the removal of solvent *in vacuo* (0.3651 g, 68% yield). GPC (THF): M_n = 6020 g/mol, PDI = 1.07. IR: 3675–3175, 3050–2700, 1675–1600, 1456, 1356, 1273, 1197, 1094, 1020, 970, 812 cm^{-1}. ^1H NMR (CD_2Cl_2, ppm): δ 7.45–7.30 (m, 5H, aromatic ring), 5.09 (d, *J* = 8.1 Hz, 2H, POC*H*$_2$Ar), 4.40–4.05 (broad, 300H, POC*H*$_2$$CH_2OCH_2CH_2S$ and POC*H*$_2$C*H*$_2$OP), 3.72–3.44 (broad, 500H, $POCH_2CH_2OCH_2CH_2SCH_2CH_2OCH_2CH_2OCH_3$), 3.33 (s, 150H, $OCH_2CH_2OCH_3$), 2.78–2.69 (broad q, 200H, $OCH_2CH_2SCH_2CH_2O$). ^{13}C NMR (CD_2Cl_2, ppm): δ 129.1, 128.5, 72.4, 71.5 (d, *J* = 18.9 Hz), 70.7, 70.1 (d, *J* = 27.9 Hz), 67.6, 67.0, 59.2, 32.4 (d, *J* = 25.5 Hz). ^{31}P NMR (CD_2Cl_2, ppm): δ -0.68. DSC: (T_g) = -64 °C. TGA in N_2: 280 °C, 70% mass loss; 30% mass remaining above 280 °C.

4.3.7. Acetalization of the Vinyl Ether Side Chain Moieties of PEVEP$_{50}$ with 4-Methylbenzyl Alcohol

In a glovebox, a solution of $PEVEP_{50}$ (0.1004 g, 0.010 mmol) and dried 4-methylbenzyl alcohol (128 mg, 1.05 mmol) in 0.5 mL of DMF were placed in a flame-dried 5 mL shell vial, and a solution of PTSA (20 mg, 0.12 mmol) in 0.5 mL of DMF was added into the solution. After 5 min of stirring, the reaction was quenched by adding TEA (excess). The reaction mixture was purified by dialysis (MWCO 6–8 kDa) in DMF followed by DCM overnight. A viscous liquid was collected after the removal of solvent *in vacuo* (74.1 mg, 67% yield). IR: 3700–3200, 3075–2775, 1622, 1454,

1430–1357, 1323, 1267, 1200, 1020, 966, 806, 750 cm^{-1}. ^{1}H NMR (CD_2Cl_2, ppm): δ 7.44–7.32 (m, 5H, aromatic ring), 7.22 (d, *J* = 7.5 Hz, 18H, $OCH_2CCHCH(CHCH)CCH_3$), 7.14 (d, *J* = 7.8 Hz, 18H, $OCH_2CCHCH(CHCH)CCH_3$), 6.49 (dd, *J* = 14.4 Hz, *J* = 6.9 Hz, 25H, CH_2OCHCH_2), 5.08 (d, *J* = 8.1 Hz, 2H, $POCH_2Ar$), 4.87–4.75 (broad q, 9H, $OCH(CH_3)O$), 4.59 and 4.45 (d, *J* = 11.4 Hz, 18H, OCH_2ArCH_3), 4.38–4.10 (broad, 325H, $POCH_2CH_2OP$, $OPOCH_2CH_2O$ and $CH_2OCHCHH$), 4.05 (broad dd, 25H, $CH_2OCHCHCHH$), 3.94–3.84 (broad, 68H, $POCH_2CH_2OCHCH_2$ and $POCH_2CH_2OCH(CH_3)O$), 3.83–3.61 (b, 48H, $OPOCH_2CH_2OH$), 2.32 (s, 27H, OCH_2ArCH_3), 1.33 (d, *J* = 5.1 Hz, 27H, $OCH(O)CH_3$). ^{13}C NMR (CD_2Cl_2, ppm): δ 151.90, 137.85, 135.83, 129.52, 128.30, 99.87, 87.66, 70.58, 68.1–67.6 (broad), 67.3 (d, *J* = 28.2 Hz), 67.2–66.4 (broad), 64.02 (d, *J* = 28.8 Hz), 21.40, 20.05. ^{31}P NMR (CD_2Cl_2, ppm): δ -0.68. DSC: (T_g) = -27 °C. TGA in N_2: 225 °C, 26% mass loss; 295 °C, 28% mass loss; 46% mass remaining above 295 °C.

4.3.8. Thio-acetalization of Vinyl Ether Side Chain Moieties of $PEVEP_{50}$ with 4-Methylbenzyl Mercaptan

In a glovebox, a solution of $PEVEP_{50}$ (0.1005 g, 0.010 mmol) and dried 4-methylbenzyl mercaptan (136 µL, 0.141 g, 1.02 mmol) in 0.5 mL of DMF were placed in a flame-dried vial, and a solution of PTSA (21 mg, 0.12 mmol) in 0.5 mL of DMF was added into the solution. After 5 min of stirring, the reaction was quenched by adding TEA (excess). The reaction mixture was purified by dialysis (MWCO 6–8 kDa) in DMF followed by DCM overnight. A viscous liquid was collected after the removal of solvent *in vacuo* (73.6 mg, 73% yield). IR: 3700–3200, 3045–2835, 1622, 1454,

1425–1350, 1323, 1265, 1200, 1020, 966, 812, 739 cm^{-1}. ^{1}H NMR (CD_2Cl_2, ppm): δ 7.44–7.32 (m, 5H, aromatic ring), 7.20 (d, *J* = 8.1 Hz, 8H, $SCH_2CC\mathit{H}CH(C\mathit{H}CH)CCH_3$), 7.11 (d, *J* = 7.8 Hz, 8H, $SCH_2CCHC\mathit{H}(CHC\mathit{H})CCH_3$), 6.50 (dd, *J* = 14.4 Hz, *J* = 6.9 Hz, 28H, $CH_2OC\mathit{H}CH_2$), 5.09 (d, *J* = 8.1 Hz, 2H, $POC\mathit{H}_2Ar$), 4.71 (q, *J* = 6.3 Hz, 4H, $SC\mathit{H}(CH_3)O$), 4.38–4.09 (broad, 328H, $POC\mathit{H}_2C\mathit{H}_2OP$, $OPOC\mathit{H}_2CH_2O$ and $CH_2OCHC\mathit{H}H$), 4.06 (broad dd, 28H, $CH_2OCHCH\mathit{H}$), 3.94–3.83 (broad, 64H, $POCH_2C\mathit{H}_2OCHCH_2$ and $POCH_2C\mathit{H}_2OCH(CH_3)S$), 3.83–3.58 (broad, 62H, $OPOCH_2C\mathit{H}_2O\mathit{H}$ and $SC\mathit{H}_2Ar$), 2.31 (s, 12H, $OCH_2ArC\mathit{H}_3$), 1.51 (d, *J* = 6.3 Hz, 12H, $OCH(O)C\mathit{H}_3$). ^{13}C NMR (CD_2Cl_2, ppm): δ 151.91, 129.66, 129.31, 105.54, 100.33, 87.68, 70.67, 67.4 (d, *J* = 28.8 Hz), 67.2–66.6 (broad), 64.42, 61.75, 32.83, 22.34, 21.34, 19.89. ^{31}P NMR (CD_2Cl_2, ppm): δ -0.67. DSC: (T_g) = -31 °C. TGA in N_2: 240 °C, 22% mass loss; 290 °C, 22% mass loss; 56% mass remaining above 290 °C.

4.3.9. Synthesis of Diblock Copolymer, α-Methoxy Poly(ethylene glycol)$_{44}$-block-poly(ethylene glycol vinyl ether phosphotriester)$_{33}$, mPEG$_{44}$-b-PEVEP$_{33}$

In a glovebox, a solution of EVEP (1.2950 g, 6.67 mmol) and $mPEG_{44}$-OH (134 mg, 0.067 mmol) in anhydrous DCM (1.3 mL) was placed in a flame-dried 5 mL shell vial with a magnetic stir bar. DBU (30 µL, 31 mg, 0.20 mmol) was injected into the mixture solution. After 6 min of stirring, the reaction was quenched by adding a solution of benzoic acid (excess). The reaction mixture was purified by dialysis in MeOH followed by DCM overnight. A viscous solid was collected after the removal of solvent *in vacuo* (0.6776 mg, 79% yield). GPC (THF): M_n = 6550 g/mol, PDI = 1.09. IR: 3700–3325, 3020–2780, 1620, 1454, 1323, 1269, 1200, 1022, 972, 814, 748 cm^{-1}. ^{1}H

NMR (CD_2Cl_2, ppm): δ 6.49 (dd, *J* = 14.4 Hz, *J* = 6.9 Hz, 33H, CH_2OCHCH_2), 4.34–4.12 (broad, 231H, $POCH_2CH_2OP$, $POCH_2CH_2OCHCH_2$ and $CH_2OCHCHH$), 4.06 (broad dd, *J* = 6.9 Hz, *J* = 2.1 Hz, 33H, $CH_2OCHCHH$), 3.94–3.86 (broad t, 66H, $POCH_2CH_2OCHCH_2$), 3.61–3.58 (broad, 176H, $CH_3OCH_2CH_2O$), 3.33 (s, 3H, $CH_3OCH_2CH_2OCH_2$). ^{13}C NMR (CD_2Cl_2, ppm): δ 151.9, 87.7, 71.0, 67.4 (d, *J* = 28.2 Hz), 67.2–66.6 (broad). ^{31}P NMR (CD_2Cl_2, ppm): δ -0.71. DSC: (T_g) = -38 °C. TGA in N_2: 250 °C, 16% mass loss; 265 °C, 10% mass loss; 300 °C, 27% mass loss; 47% mass remaining above 300 °C.

4.3.10. General Procedure for the Self-assembly of $mPEG_{44}$-b-$PEVEP_{33}$

The amphiphilic diblock copolymer, $mPEG_{44}$-*b*-$PEVEP_{50}$, (1.0 mg) was suspended into nanopure water (for TEM and AFM analyses), 3-(*N*-morpholino)propanesulfonic acid (MOPS) buffer (10 mM, pH 7.4) or ammonium acetate buffer (10 mM, pH 5.0) (for DLS and zeta potential measurements) in a vial and stirred at room temperature for 30 min.

4.3.11. Investigation of the Micelle Stability in Aqueous Solution by Monitoring the Changes in Hydrodynamic Diameters and Intensity, Scattered by Micelles, as Measured by DLS

Amphiphilic diblock copolymers, $mPEG_{44}$-*b*-$PEVEP_{33}$, were dissolved (1 mg/mL) in 3-(*N*-morpholino)propanesulfonic acid (MOPS) buffer (10 mM, pH 7.4) or ammonium acetate buffer (10 mM, pH 5.0) in a vial. The prepared solutions were stirred at room temperature or incubated in a shaker at 37 °C and, hydrodynamic

diameter and intensity, scattered by the micelles were monitored by using DLS over a period of time.

4.3.12. Investigation of the Degradability of the PEVEP Backbone Segment in Aqueous Solution by Using ^{31}P NMR Spectroscopy

A solution of amphiphilic diblock copolymers, mPEG$_{44}$-*b*-PEVEP$_{33}$, (10 mg/mL) in 3-(*N*-morpholino)propanesulfonic acid (MOPS) buffer (10 mM in D_2O, pH 7.4) or sodium acetate buffer (10 mM in D_2O, pH 5.0) was incubated in a shaker at 37 °C and, and the backbone degradability of PEVEP was monitored by ^{31}P NMR spectroscopy over a period of time.

4.3.13. Investigation of the Stability of the Vinyl Ether Side Chain Moieties in Aqueous Solution by Using ^{1}H NMR Spectroscopy

A solution of amphiphilic diblock copolymers, mPEG$_{44}$-*b*-PEVEP$_{33}$, (10 mg/mL) in 3-(*N*-morpholino)propanesulfonic acid (MOPS) buffer (10 mM in D_2O, pH 7.4) or sodium acetate buffer (10 mM in D_2O, pH 5.0) was incubated in a shaker at 37 °C and, the disappearance of the vinyl group and the appearance of acetaldehyde ^{1}H resonance peaks were monitored by using ^{1}H NMR spectroscopy over a period of time.

4.3.14. Preparation and Identification of the Degradation Products of the Micelles

A solution of amphiphilic diblock copolymers, mPEG$_{44}$-*b*-PEVEP$_{33}$, (6 mg/mL) in ammonium acetate buffer (D_2O, 10 mM, pH 5.0) was incubated in a shaker at 37 °C until the micelle detection was not possible by DLS and the complete disappearance of ^{31}P resonance signal from the intact PEVEP backbone was confirmed by ^{31}P NMR

spectroscopy. The solution was lyophilized into a powder, and then analyzed by ESI, GC and MALDI-TOF MS.

4.3.15. Preparation of Degradation Products for Cytotoxicity Tests

A solution of amphiphilic diblock copolymers, $mPEG_{44}$-*b*-$PEVEP_{33}$, (9 mg/mL) in phosphate buffered saline (PBS) (10 mM, pH 7.4) was incubated in a shaker at 37 °C until the micelles were not detectable by DLS. The solution was lyophilized into a powder and was used for the cytotoxicity tests.

4.3.16. Cytotoxicity Assays

Human ovarian adenocarcinoma cells (OVCAR-3) (5×10^3 cells/well) and RAW 264.7 mouse macrophages (2×10^4 cells/well) were plated in 96-well plates in RPMI-1640 medium and Dulbecco's Modified Eagle's Medium (DMEM) (20% and 10% fetal bovine serum, for the OVCAR-3 and RAW 264.7, respectively, and 1% penicillin/streptomycin). Cells were incubated at 37 °C in a humidified atmosphere containing 5% CO_2 atmosphere. The medium was replaced with a fresh medium 24 h after seeding, and 1 h prior to the addition of the various formulations at concentrations ranged from 18.0×10^{-3} to 1.76 μg/mL of polymer dissolved in phosphate buffered saline (PBS). For each well, 20 μL of each formulation was added to 100 μL of the medium. Negative controls were created by addition of 20 μL of PBS to wells containing 100 μL of the medium. The cells were incubated for 24 h, and after this period, the media was replaced with 100 μL of the complete medium. Then, 20 μL of the MTS combined reagent was added to each well (Cell Titer 96® Aqueous Non-Radioactive Cell Proliferation Assay, Promega Co.). The cells were incubated with the

reagent for 2 h for RAW 264.7 cells, and 3 h for OVCAR-3 cells, at 37 ˚C in a humidified atmosphere containing 5% CO_2 protected from light. Absorbance was measured at 490 nm by using SpectraMax M5 (Molecular Devices Co.). The cell viability was calculated based on the relative absorbance to the control untreated cells.

4.4. Conclusions

In conclusion, a novel polyphosphoester with ethylene glycol vinyl ether side chain functionality was developed as a versatile template for postpolymerization modifications, and its degradability and biocompatibility were investigated. A well-defined (PDI ≤1.05) homopolymer with vinyl ether side chain functionality was prepared by conducting ROP using an organocatalyst, DBU. The kinetic study of this homopolymerization revealed an excellent controllability during ROP with predetermined molecular weights and narrow molecular weight distributions. Subsequently, the vinyl ether side chain moieties displayed chemical availability and reactivity upon conjugation with hydroxyl- or thiol-containing model small molecules *via* three different types of conjugation chemistries – thiol-ene "click" reaction, acetalization, or thio–acetalization reaction – resulting in modified polymers that contained either stable thio–ether or hydrolytically–labile acetal or thio–acetal linkages. Despite the relatively low conversion percentages observed during acetalization and thio-acetalization, *ca.* 18 and 8%, respectively, we anticipate that these degrees of conjugation efficiency would be adequate to achieve a sufficient loading of diagnostic and/or therapeutic molecules into this nanoparticle system. Meanwhile, amphiphilic diblock copolymers, $mPEG_{44}$-*b*-$PEVEP_{33}$, were also prepared by ROP, and they afforded

well-defined micelles with a narrow and monomodal size distribution in water. The degradation study of the prepared micelles demonstrated a full acid-catalyzed hydrolytic degradation behavior of both the side chain functionalities and the backbone linkages. Finally, the parent micelles and their degradation products, as identified qualitatively by mass spectrometry, were found to be nontoxic toward RAW 264.7 mouse macrophages and OVCAR-3 human ovarian adenocarcinoma cells. The fundamental understanding of selective hydrolysis of the vinyl ether and/or acetal/thio–acetal moieties for the introduction of hydroxyl groups to the PPE system, which was conventionally limited to a cyclic PPE monomer, as a potential protecting group strategy is currently under investigation. Moreover, incorporation of biologically–active molecules into these PEVEP-based functional, degradable polymers *via* the presented conjugation chemistries is underway.

CHAPTER V

CONCLUSIONS

In the development of highly well-defined polymer nanoparticles (NPs) demonstrating unique performance toward the effective treatment of infectious diseases, the combination of state-of-the-art polymerization chemistries, postpolymerization chemical modifications, supramolecular assembly processes and further transformations is essential. Toward this aim, this research dissertation heighted two parts: (1) development of potentially fully degradable, biocompatible NPs as delivery carriers for silver-based antimicrobials, as described in Chapter II, and (2) preparation and evaluation of degradable, biocompatible, and functional polymeric system as potential delivery carrier, as discussed in Chapter III and IV.

In Chapter II, synthesis of a diblock copolymer, polyphosphoester-*block*-poly(L-lactide) (PPE-*b*-PLLA), which has potential for being fully degradable and biocompatible, was achieved by one-pot sequential ring-opening polymerizations (ROPs) of two cyclic monomers: alkyne-functionalized phospholane and L-lactide (LLA). A kinetic study of the polymerization in each step was investigated in a detailed manner by nuclear magnetic resonance spectroscopy (NMR) and gel permeation chromatography, revealing living/controlled characteristics with narrow molecular weight distributions and a linear increase of molecular weights *vs.* monomer conversion and time. Subsequently, photoinduced thiol-yne "click" reactions with small-molecule thiols bearing either carboxylic acid or amino groups afforded amphiphilic diblock

copolymers with carboxylate or amino side-chain functionalities along the PPE segment of the diblock copolymer backbone. Finally, direct dissolution of the two different types of amphiphilic diblock copolymers in aqueous solutions yielded well-defined spherical micelles with corresponding negative or positive surface charges, respectively, as confirmed by transmission electron microscopy, dynamic light scattering, and zeta potential analyses.

In Chapter III, silver-bearing, fully biodegradable and functional polymeric NPs were developed, and their antimicrobial activity was evaluated *in vitro.* A series of degradable polymeric nanoparticles (dNPs), composed of PPE and PLLA and designed specifically for silver loading into the hydrophilic shell and/or the hydrophobic core, were prepared as potential delivery carriers for three different types of silver-based antimicrobials – silver acetate or one of two silver carbene complexes (SCCs). Silver-loading capacities of the dNPs were not influenced by the hydrophilic block chain length, loading site (*i.e.*, core or shell), or type of silver compound, but optimization of the silver feed ratio was crucial to maximize the silver loading capacity of dNPs, up to *ca.* 12% (w/w). The release kinetics of silver-bearing dNPs revealed 50% release at *ca.* 2.5–5.5 h depending on the type of silver compound. In addition, we undertook a comprehensive evaluation of the rates of hydrolytic or enzymatic degradability and performed structural characterization of the degradation products. Interestingly, packaging of the SCCs in the dNP-based delivery system improved minimum inhibitory concentrations up to 70%, compared with the SCCs alone, as measured *in vitro* against 10 contemporary epidemic strains of *Staphylococcus aureus* and eight uropathogenic

strains of *Escherichia coli*. We conclude that these dNP-based delivery systems may be beneficial for direct epithelial treatment and/or prevention of ubiquitous bacterial infections, including those of the skin and urinary tract. Further studies include the understanding of fundamental interactions between bacterial cells, the dNPs and their degradation products. Moreover, conjugation of the dNPs with tissue-specific targeting proteins or peptides and determination of *in vivo* biodistribution, toxicity, and therapeutic efficacy of the Ag-dNPs against bacterial infectious diseases represent important future goals in demonstrating the translational potential of these novel nanoconstructs.

In Chapter IV, a novel PPE with vinyl ether side chain functionality was developed as a versatile template for postpolymerization modifications, and its degradability and biocompatibility were evaluated. An organocatalyzed ROP of ethylene glycol vinyl ether-pendant cyclic phosphotriester monomer allowed for construction of poly(ethylene glycol vinyl ether phosphotriester) (PEVEP). This vinyl ether-functionalized PPE scaffold was coupled with hydroxyl- or thiol-containing model small molecules *via* three different types of conjugation chemistries – thiol–ene "click" reaction, acetalization, or thio–acetalization reaction – to afford modified polymers that accommodated either stable thio-ether or hydrolytically-labile acetal or thio-acetal linkages. Amphiphilic diblock copolymers of poly(ethylene glycol) and PEVEP formed well-defined micelles with a narrow and monomodal size distribution in water, as confirmed by DLS, transmission electron microscopy, and atomic force microscopy. The stability of the micelles and the hydrolytic degradability of the backbone and side

chains of the PEVEP block segment were assessed by DLS and NMR spectroscopy (^{1}H and ^{31}P), respectively, in aqueous buffer solutions at pH values of 5.0 and 7.4 and at temperatures of 25 and 37 °C. The hydrolytic degradation products of the PEVEP segments of the block copolymers were then identified by electrospray ionization, gas chromatography, and matrix-assisted laser desorption/ionization mass spectrometry. The parent micelles and their degradation products were found to be non-cytotoxic at concentrations up to 3 mg/mL, when evaluated with RAW 264.7 mouse macrophages and OVCAR-3 human ovarian adenocarcinoma cells. The fundamental understanding of selective hydrolysis of the vinyl ether and/or acetal/thio–acetal moieties for the introduction of hydroxyl groups to the PPE system, which was conventionally limited to a cyclic PPE monomer, as a potential protecting group strategy would be vital. Moreover, the future studies include incorporation of biologically–active molecules into these PEVEP-based functional, degradable polymers *via* the presented conjugation chemistries.

REFERENCES

(1) Koul, A.; Arnoult, E.; Lounis, N.; Guillemont, J.; Andries, K. *Nature* **2011**, *469*, 483-490.

(2) Allen, T.; Cullis, P. *Science* **2004**, *303*, 1818-1822.

(3) Zhang, L.; Gu, F. X.; Chan, J. M.; Wang, A. Z.; Langer, R. S.; Farokhzad, O. C. *Clin. Pharmacol. Ther.* **2008**, *83*, 761-769.

(4) Wagner, V.; Dullaart, A.; Bock, A. K.; Zweck, A. *Nat. Biotechnol.* **2006**, *24*, 1211-1217.

(5) Huang, R.; Mocherla, S.; Heslinga, M.; Charoenphol, P.; Eniola Adefeso, O. *Molec. Membrane Biol.* **2010**, *27*, 312-327.

(6) Zhao, F.; Zhao, Y.; Liu, Y.; Chang, X.; Chen, C. *Small* **2011**, *7*, 1322-1337.

(7) Dykman, L.; Khlebtsov, N. *Chem. Soc. Rev.* **2012**, *41*, 2256-2282.

(8) Veiseh, O.; Gunn, J. W.; Zhang, M. *Adv. Drug Deliv. Rev.* **2010**, *62*, 284-304.

(9) Elsabahy, M.; Wooley, K. *Chem. Soc. Rev.* **2012**, *41*, 2545-2561.

(10) Elsabahy, M.; Wooley, K. L. *J. Polym. Sci. A Polym. Chem.* **2012**, *50*, 1869-1880.

(11) Son, Y.-J.; McConville, J. T. *Drug Dev. Ind. Pharm.* **2008**, *34*, 948-959.

(12) du Toit, L. C.; Pillay, V.; Danckwerts, M. P. *Respir. Res.* **2006**, *7*.

(13) Petros, R.; DeSimone, J. *Nat. Rev. Drug Discov.* **2010**, *9*, 615-627.

(14) Choi, H. S.; Frangioni, J. V. *Molecular Imaging* **2010**, *9*, 291-310.

(15) Courrier, H. M.; Butz, N.; Vandamme, T. F. *Crit. Rev. Ther. Drug Carr. Syst.* **2002**, *19*, 425-498.

(16) Azarmi, S.; Roa, W. H.; Löbenberg, R. *Adv. Drug Deliv. Rev.* **2008**, *60*, 863-875.

(17) Sung, J. C.; Pulliam, B. L.; Edwards, D. A. *Trends in Biotechnology* **2007**, *25*, 563-570.

(18) Sanders, N.; Rudolph, C.; Braeckmans, K.; De Smedt, S. C.; Demeester, J. *Adv. Drug Deliv. Rev.* **2009**, *61*, 115-127.

(19) Lai, S. K.; Wang, Y.-Y.; Hanes, J. *Adv. Drug Deliv. Rev.* **2009**, *61*, 158-171.

(20) Griesenbach, U.; Alton, E. W. F. W. *Adv. Drug Deliv. Rev.* **2009**, *61*, 128-139.

(21) Mühlfeld, C.; Rothen-Rutishauser, B.; Blank, F.; Vanhecke, D.; Ochs, M.; Gehr, P. *Am. J. Physiol. Lung Cell. Mol. Physiol.* **2008**, *294*, L817-L829.

(22) Lai, S.; Wang, Y.-Y.; Wirtz, D.; Hanes, J. *Adv. Drug Deliv. Rev.* **2009**, *61*, 86-100.

(23) Henke, M. O.; Ratjen, F. *Paediatr. Respir. Rev.* **2007**, *8*, 24-29.

(24) Dobrovolskaia, M. A.; McNeil, S. E. *Nat. Nanotechnol.* **2007**, *2*, 469-478.

(25) Elsabahy, M.; Wooley, K. L. *Chem. Soc. Rev.* **2013**, *42*, 5552-5576.

(26) Langer, R. *Science* **1990**, *249*, 1527-1533.

(27) Nederberg, F.; Zhang, Y.; Tan, J. P. K.; Xu, K.; Wang, H.; Yang, C.; Gao, S.; Guo, X. D.; Fukushima, K.; Li, L.; Hedrick, J. L.; Yang, Y.-Y. *Nat. Chem.* **2011**, *3*, 409-414.

(28) Kang, N.; Perron, M.-È.; Prud'homme, R. E.; Zhang, Y.; Gaucher, G.; Leroux, J.-C. *Nano Lett.* **2005**, *5*, 315-319.

(29) Yu, Y.; Zou, J.; Yu, L.; Ji, W.; Li, Y.; Law, W.-C.; Cheng, C. *Macromolecules* **2011**, *44*, 4793-4800.

(30) Zhang, X.; Zhong, Z.; Zhuo, R. *Macromolecules* **2011**, *44*, 1755-1759.

(31) Xu, J.; Prifti, F.; Song, J. *Macromolecules* **2011**, *44*, 2660-2667.

(32) Csihony, S.; Culkin, D. A.; Sentman, A. C.; Dove, A. P.; Waymouth, R. M.; Hedrick, J. L. *J. Am. Chem. Soc.* **2005**, *127*, 9079-9084.

(33) Dove, A. P.; Pratt, R. C.; Lohmeijer, B. G. G.; Waymouth, R. M.; Hedrick, J. L. *J. Am. Chem. Soc.* **2005**, *127*, 13798-13799.

(34) Kang, H. U.; Yu, Y. C.; Shin, S. J.; Kim, J.; Youk, J. H. *Macromolecules* **2013**, *46*, 1291-1295.

(35) Coady, D. J.; Engler, A. C.; Horn, H. W.; Bajjuri, K. M.; Fukushima, K.; Jones, G. O.; Nelson, A.; Rice, J. E.; Hedrick, J. L. *ACS Macro Lett.* **2011**, *1*, 19-22.

(36) Kamber, N. E.; Jeong, W.; Waymouth, R. M.; Pratt, R. C.; Lohmeijer, B. G. G.; Hedrick, J. L. *Chem. Rev.* **2007**, *107*, 5813-5840.

(37) Hild, F.; Neehaul, N.; Bier, F.; Wirsum, M.; Gourlaouen, C.; Dagorne, S. *Organometallics* **2013**, *32*, 587-598.

(38) Tempelaar, S.; Barker, I. A.; Truong, V. X.; Hall, D. J.; Mespouille, L.; Dubois, P.; Dove, A. P. *Polym. Chem.* **2013**, *4*, 174-183.

(39) Zhang, S.; Zou, J.; Zhang, F.; Elsabahy, M.; Felder, S. E.; Zhu, J.; Pochan, D. J.; Wooley, K. L. *J. Am. Chem. Soc.* **2012**, *134*, 18467-18474.

(40) Zhang, S.; Li, A.; Zou, J.; Lin, L. Y.; Wooley, K. L. *ACS Macro Lett.* **2012**, *1*, 328-333.

(41) Wang, Y.-C.; Yuan, Y.-Y.; Wang, F.; Wang, J. *J. Polym. Sci. A Polym. Chem.* **2011**, *49*, 487-494.

(42) Liu, J.; Huang, W.; Pang, Y.; Zhu, X.; Zhou, Y.; Yan, D. *Biomacromolecules* **2010**, *11*, 1564-1570.

(43) Iwasaki, Y.; Akiyoshi, K. *Macromolecules* **2004**, *37*, 7637-7642.

(44) Thurn-Albrecht, T.; Schotter, J.; Kästle, G. A.; Emley, N.; Shibauchi, T.; Krusin-Elbaum, L.; Guarini, K.; Black, C. T.; Tuominen, M. T.; Russell, T. P. *Science* **2000**, *290*, 2126-2129.

(45) Bates, F. S.; Hillmyer, M. A.; Lodge, T. P.; Bates, C. M.; Delaney, K. T.; Fredrickson, G. H. *Science* **2012**, *336*, 434-440.

(46) Li, B.; Li, L.; Wang, B.; Li, C. Y. *Nat. Nanotechnol.* **2009**, *4*, 358-362.

(47) Warren, S. C.; Messina, L. C.; Slaughter, L. S.; Kamperman, M.; Zhou, Q.; Gruner, S. M.; DiSalvo, F. J.; Wiesner, U. *Science* **2008**, *320*, 1748-1752.

(48) Jeong, B.; Bae, Y. H.; Lee, D. S.; Kim, S. W. *Nature* **1997**, *388*, 860-862.

(49) Dimitrov, I. V.; Berlinova, I. V.; Michailova, V. I. *Polym. J.* **2013**, *45*, 457-461.

(50) Samarajeewa, S.; Ibricevic, A.; Gunsten, S. P.; Shrestha, R.; Elsabahy, M.; Brody, S. L.; Wooley, K. L. *Biomacromolecules* **2013**, *14*, 1018-1027.

(51) Samarajeewa, S.; Shrestha, R.; Li, Y.; Wooley, K. L. *J. Am. Chem. Soc.* **2011**, *134*, 1235-1242.

(52) Yamamoto, Y.; Yasugi, K.; Harada, A.; Nagasaki, Y.; Kataoka, K. *J. Controlled Release* **2002**, *82*, 359-371.

(53) Sun, J.; Chen, X.; Lu, T.; Liu, S.; Tian, H.; Guo, Z.; Jing, X. *Langmuir* **2008**, *24*, 10099-10106.

(54) Petzetakis, N.; Dove, A. P.; O'Reilly, R. K. *Chem. Sci.* **2011**, *2*, 955-960.

(55) Ting, S. R. S.; Gregory, A. M.; Stenzel, M. H. *Biomacromolecules* **2009**, *10*, 342-352.

(56) Xiong, M.-H.; Bao, Y.; Yang, X.-Z.; Wang, Y.-C.; Sun, B.; Wang, J. *J. Am. Chem. Soc.* **2012**, *134*, 4355-4362.

(57) Lapienis, G.; Penczek, S.; Pretula, J. *Macromolecules* **1983**, *16*, 153-158.

(58) Wang, Y.-C.; Yuan, Y.-Y.; Du, J.-Z.; Yang, X.-Z.; Wang, J. *Macromol. Biosci.* **2009**, *9*, 1154-1164.

(59) Iwasaki, Y.; Yamaguchi, E. *Macromolecules* **2010**, *43*, 2664-2666.

(60) Clément, B.; Grignard, B.; Koole, L.; Jérôme, C.; Lecomte, P. *Macromolecules* **2012**, *45*, 4476-4486.

(61) Yang, X.-Z.; Sun, T.-M.; Dou, S.; Wu, J.; Wang, Y.-C.; Wang, J. *Biomacromolecules* **2009**, *10*, 2213-2220.

(62) Hoyle, C. E.; Bowman, C. N. *Angew. Chem., Int. Ed.* **2010**, *49*, 1540-1573.

(63) Iha, R. K.; Wooley, K. L.; Nyström, A. M.; Burke, D. J.; Kade, M. J.; Hawker, C. J. *Chem. Rev.* **2009**, *109*, 5620-5686.

(64) Huh, A. J.; Kwon, Y. J. *J. Controlled Release* **2011**, *156*, 128-145.

(65) Taubes, G. *Science* **2008**, *321*, 356-361.

(66) Mitragotri, S.; Burke, P. A.; Langer, R. *Nat. Rev. Drug Discov.* **2014**, *13*, 655-672.

(67) Rizzello, L.; Pompa, P. P. *Chem. Soc. Rev.* **2014**, *43*, 1501-1518.

(68) Melaiye, A.; Youngs, W. J. *Expert Opin. Ther. Pat.* **2005**, *15*, 125-130.

(69) Silver, S. *FEMS Microbiol. Rev.* **2003**, *27*, 341-353.

(70) Gupta, A.; Matsui, K.; Lo, J.-F.; Silver, S. *Nat. Med.* **1999**, *5*, 183-188.

(71) Lansdown, A. B. *J. Wound Care* **2002**, *11*, 125-130.

(72) Mijnendonckx, K.; Leys, N.; Mahillon, J.; Silver, S.; Van Houdt, R. *BioMetals* **2013**, *26*, 609-621.

(73) Balogh, L.; Swanson, D. R.; Tomalia, D. A.; Hagnauer, G. L.; McManus, A. T. *Nano Lett.* **2000**, *1*, 18-21.

(74) Sambhy, V.; MacBride, M. M.; Peterson, B. R.; Sen, A. *J. Am. Chem. Soc.* **2006**, *128*, 9798-9808.

(75) Aymonier, C.; Schlotterbeck, U.; Antonietti, L.; Zacharias, P.; Thomann, R.; Tiller, J. C.; Mecking, S. *Chem. Commun.* **2002**, 3018-3019.

(76) Cannon, C. L.; Hogue, L. A.; Vajravelu, R. K.; Capps, G. H.; Ibricevic, A.; Hindi, K. M.; Kascatan-Nebioglu, A.; Walter, M. J.; Brody, S. L.; Youngs, W. J. *Antimicrob. Agents Chemother.* **2009**, *53*, 3285-3293.

(77) Garrison, J. C.; Youngs, W. J. *Chem. Rev.* **2005**, *105*, 3978-4008.

(78) Hindi, K.; Siciliano, T.; Durmus, S.; Panzner, M.; Medvetz, D.; Reddy, D. V.; Hogue, L.; Hovis, C.; Hilliard, J.; Mallet, R.; Tessier, C.; Cannon, C.; Youngs, W. *J. Med. Chem.* **2008**, *51*, 1577-1583.

(79) Kascatan Nebioglu, A.; Melaiye, A.; Hindi, K.; Durmus, S.; Panzner, M.; Hogue, L.; Mallett, R.; Hovis, C.; Coughenour, M.; Crosby, S.; Milsted, A.; Ely, D.; Tessier, C.; Cannon, C.; Youngs, W. *J. Med. Chem.* **2006**, *49*, 6811-6818.

(80) Kascatan Nebioglu, A.; Panzner, M.; Tessier, C.; Cannon, C.; Youngs, W. *Coord. Chem. Rev.* **2007**, *251*, 884-895.

(81) Youngs, W. J.; Knapp, A. R.; Wagers, P. O.; Tessier, C. A. *Dalton Trans.* **2012**, *41*, 327-336.

(82) Leid, J. G.; Ditto, A. J.; Knapp, A.; Shah, P. N.; Wright, B. D.; Blust, R.; Christensen, L.; Clemons, C. B.; Wilber, J. P.; Young, G. W.; Kang, A. G.; Panzner, M. J.; Cannon, C. L.; Yun, Y. H.; Youngs, W. J.; Seckinger, N. M.; Cope, E. K. *J. Antimicrob. Chemother.* **2012**, *67*, 138-148.

(83) Hindi, K. M.; Panzner, M. J.; Tessier, C. A.; Cannon, C. L.; Youngs, W. J. *Chem. Rev.* **2009**, *109*, 3859-3884.

(84) Panzner, M. J.; Hindi, K. M.; Wright, B. D.; Taylor, J. B.; Han, D. S.; Youngs, W. J.; Cannon, C. L. *Dalton Trans.* **2009**, 7308-7313.

(85) Hindi, K. M.; Ditto, A. J.; Panzner, M. J.; Medvetz, D. A.; Han, D. S.; Hovis, C. E.; Hilliard, J. K.; Taylor, J. B.; Yun, Y. H.; Cannon, C. L.; Youngs, W. J. *Biomaterials* **2009**, *30*, 3771-3779.

(86) Li, Y.; Hindi, K.; Watts, K. M.; Taylor, J. B.; Zhang, K.; Li, Z.; Hunstad, D. A.; Cannon, C. L.; Youngs, W. J.; Wooley, K. L. *Chem. Commun.* **2010**, *46*, 121-123.

(87) Shah, P. N.; Lin, L. Y.; Smolen, J. A.; Tagaev, J. A.; Gunsten, S. P.; Han, D. S.; Heo, G. S.; Li, Y.; Zhang, F.; Zhang, S.; Wright, B. D.; Panzner, M. J.; Youngs, W. J.; Brody, S. L.; Wooley, K. L.; Cannon, C. L. *ACS Nano* **2013**, *7*, 4977-4987.

(88) Kumari, A.; Yadav, S. K.; Yadav, S. C. *Colloids Surf., B* **2010**, *75*, 1-18.

(89) Zhao, Z.; Wang, J.; Mao, H.-Q.; Leong, K. W. *Adv. Drug Deliv. Rev.* **2003**, *55*, 483-499.

(90) Tempelaar, S.; Mespouille, L.; Coulembier, O.; Dubois, P.; Dove, A. P. *Chem. Soc. Rev.* **2013**, *42*, 1312-1336.

(91) Pounder, R. J.; Dove, A. P. *Polym. Chem.* **2010**, *1*, 260-271.

(92) Hadjichristidis, N.; Iatrou, H.; Pitsikalis, M.; Sakellariou, G. *Chem. Rev.* **2009**, *109*, 5528-5578.

(93) Kricheldorf, H. R. *Angew. Chem., Int. Ed.* **2006**, *45*, 5752-5784.

(94) Lim, Y. H.; Heo, G. S.; Cho, S.; Wooley, K. L. *ACS Macro Lett.* **2013**, *2*, 785-789.

(95) Lim, Y. H.; Heo, G. S.; Rezenom, Y. H.; Pollack, S.; Raymond, J. E.; Elsabahy, M.; Wooley, K. L. *Macromolecules* **2014**, *47*, 4634-4644.

(96) Gustafson, T. P.; Lim, Y. H.; Flores, J. A.; Heo, G. S.; Zhang, F.; Zhang, S.; Samarajeewa, S.; Raymond, J. E.; Wooley, K. L. *Langmuir* **2014**, *30*, 631-641.

(97) Elsabahy, M.; Zhang, S.; Zhang, F.; Deng, Z. J.; Lim, Y. H.; Wang, H.; Parsamian, P.; Hammond, P. T.; Wooley, K. L. *Sci. Rep.* **2013**, *3*.

(98) Gustafson, T. P.; Lonnecker, A. T.; Heo, G. S.; Zhang, S.; Dove, A. P.; Wooley, K. L. *Biomacromolecules* **2013**, *14*, 3346-3353.

(99) Fan, J.; Li, R.; He, X.; Seetho, K.; Zhang, F.; Zou, J.; Wooley, K. L. *Polym. Chem.* **2014**, *5*, 3977-3981.

(100) Aweda, T. A. Z., S.; Mupanomunda, C.; Burkemper, J.; Heo, G. S.; Bandara, N.; Lin, M.; Cutler, C.; Cannon, C. L.; Youngs, W.; Wooley, K. L.; Lapi, S. E. *J. Pharm. Sci.*, Submitted for publication.

(101) Garlotta, D. *J. Polym. Environ.* **2001**, *9*, 63-84.

(102) Athanasiou, K. A.; Niederauer, G. G.; Agrawal, C. M. *Biomaterials* **1996**, *17*, 93-102.

(103) Wang, D.-A.; Williams, C. G.; Yang, F.; Cher, N.; Lee, H.; Elisseeff, J. H. *Tissue Eng.* **2005**, *11*, 201-213.

(104) Baran, J.; Penczek, S. *Macromolecules* **1995**, *28*, 5167-5176.

(105) Wang, X.; Xie, X.; Cai, C.; Rytting, E.; Steele, T.; Kissel, T. *Macromolecules* **2008**, *41*, 2791-2799.

(106) Iwasaki, Y.; Nakagawa, C.; Ohtomi, M.; Ishihara, K.; Akiyoshi, K. *Biomacromolecules* **2004**, *5*, 1110-1115.

(107) Samarajeewa, S.; Zentay, R. P.; Jhurry, N. D.; Li, A.; Seetho, K.; Zou, J.; Wooley, K. L. *Chem. Commun.* **2014**, *50*, 968-970.

(108) Panzner, M. J.; Deeraksa, A.; Smith, A.; Wright, B. D.; Hindi, K. M.; Kascatan-Nebioglu, A.; Torres, A. G.; Judy, B. M.; Hovis, C. E.; Hilliard, J. K.; Mallett, R.

J.; Cope, E.; Estes, D. M.; Cannon, C. L.; Leid, J. G.; Youngs, W. J. *Eur. J. Inorg. Chem.* **2009**, 1739-1745.

(109) Youngs, W. J.; Medvetz, D. A.; Hindi, K. M.; Panzner, M. J.; Ditto, A. J.; Yun, Y. H. *Met.-Based Drugs* **2008**, *2008*.

(110) Dominguez, A.; Fernandez, A.; Gonzalez, N.; Iglesias, E.; Montenegro, L. *J. Chem. Educ.* **1997**, *74*, 1227.

(111) Sanders, D. P.; Coady, D. J.; Yasumoto, M.; Fujiwara, M.; Sardon, H.; Hedrick, J. L. *Polym. Chem.* **2014**, *5*, 327-329.

(112) Sanders, D. P.; Fukushima, K.; Coady, D. J.; Nelson, A.; Fujiwara, M.; Yasumoto, M.; Hedrick, J. L. *J. Am. Chem. Soc.* **2010**, *132*, 14724-14726.

(113) Meldal, M.; Tornøe, C. W. *Chem. Rev.* **2008**, *108*, 2952-3015.

(114) Tasdelen, M. A. *Polym. Chem.* **2011**, *2*, 2133-2145.

(115) Lowe, A. B. *Polym. Chem.* **2010**, *1*, 17-36.

(116) Iha, R. K.; Wooley, K. L.; Nyström, A. M.; Burked, D. J.; Kade, M. J.; Hawker, C. J. *Chem. Rev.* **2009**, *109*, 5620-5686.

(117) Binder, W. H.; Sachsenhofer, R. *Macromol. Rapid Commun.* **2007**, *28*, 15-54.

(118) Fournier, D.; Hoogenboom, R.; Schubert, U. S. *Chem. Soc. Rev.* **2007**, *36*, 1369-1380.

(119) Kolb, H. C.; Finn, M. G.; Sharpless, K. B. *Angew. Chem., Int. Ed.* **2001**, *40*, 2004-2021.

(120) Thirumurugan, P.; Matosiuk, D.; Jozwiak, K. *Chem. Rev.* **2013**, *113*, 4905-4979.

(121) Gillies, E. R.; Jonsson, T. B.; Fréchet, J. M. J. *J. Am. Chem. Soc.* **2004**, *126*, 11936-11943.

(122) Gillies, E. R.; Frechet, J. M. J. *Chem. Commun.* **2003**, 1640-1641.

(123) Murthy, N.; Thng, Y. X.; Schuck, S.; Xu, M. C.; Fréchet, J. M. J. *J. Am. Chem. Soc.* **2002**, *124*, 12398-12399.

(124) Tang, R.; Ji, W.; Panus, D.; Palumbo, R. N.; Wang, C. *J. Controlled Release* **2011**, *151*, 18-27.

(125) Lin, S.; Du, F.; Wang, Y.; Ji, S.; Liang, D.; Yu, L.; Li, Z. *Biomacromolecules* **2007**, *9*, 109-115.

(126) Bae, Y.; Fukushima, S.; Harada, A.; Kataoka, K. *Angew. Chem., Int. Ed.* **2003**, *42*, 4640-4643.

(127) Filippov, S. K.; Franklin, J. M.; Konarev, P. V.; Chytil, P.; Etrych, T.; Bogomolova, A.; Dyakonova, M.; Papadakis, C. M.; Radulescu, A.; Ulbrich, K.; Stepanek, P.; Svergun, D. I. *Biomacromolecules* **2013**, *14*, 4061-4070.

(128) Delplace, V.; Couvreur, P.; Nicolas, J. *Polym. Chem.* **2014**, *5*, 1529-1544.

(129) Steen, K. H.; Steen, A. E.; Reeh, P. W. *J. Neurosci.* **1995**, *15*, 3982-3989.

(130) Tannock, I. F.; Rotin, D. *Cancer Res.* **1989**, *49*, 4373-4384.

(131) Helmlinger, G.; Sckell, A.; Dellian, M.; Forbes, N. S.; Jain, R. K. *Clin. Cancer Res.* **2002**, *8*, 1284-1291.

(132) Gillies, E. R.; Goodwin, A. P.; Fréchet, J. M. J. *Bioconjugate Chem.* **2004**, *15*, 1254-1263.

(133) Heffernan, M. J.; Murthy, N. *Bioconjugate Chem.* **2005**, *16*, 1340-1342.

(134) Bachelder, E. M.; Beaudette, T. T.; Broaders, K. E.; Dashe, J.; Fréchet, J. M. J. *J. Am. Chem. Soc.* **2008**, *130*, 10494-10495.

(135) Natalello, A.; Tonhauser, C.; Frey, H. *ACS Macro Lett.* **2013**, *2*, 409-413.

(136) Satoh, K.; Poelma, J. E.; Campos, L. M.; Stahl, B.; Hawker, C. J. *Polym. Chem.* **2012**, *3*, 1890-1898.

(137) Tonhauser, C.; Schüll, C.; Dingels, C.; Frey, H. *ACS Macro Lett.* **2012**, *1*, 1094-1097.

(138) Li, Y.; Du, W.; Sun, G.; Wooley, K. L. *Macromolecules* **2008**, *41*, 6605-6607.

(139) Mangold, C.; Dingels, C.; Obermeier, B.; Frey, H.; Wurm, F. *Macromolecules* **2011**, *44*, 6326-6334.

(140) Rickerby, J.; Prabhakar, R.; Ali, M.; Knowles, J.; Brocchini, S. *J. Mater. Chem.* **2005**, *15*, 1849-1856.

(141) Wang, H.; He, J.; Zhang, M.; Tao, Y.; Li, F.; Tam, K. C.; Ni, P. *J. Mater. Chem. B* **2013**, *1*, 6596-6607.

(142) Zhao, J.; Wang, H.; Liu, J.; Deng, L.; Liu, J.; Dong, A.; Zhang, J. *Biomacromolecules* **2013**, *14*, 3973-3984.

(143) Gu, Y.; Zhong, Y.; Meng, F.; Cheng, R.; Deng, C.; Zhong, Z. *Biomacromolecules* **2013**, *14*, 2772-2780.

(144) Shen, Y.; Zhang, S.; Zhang, F.; Loftis, A.; Pavía-Sanders, A.; Zou, J.; Fan, J.; Taylor, J.-S. A.; Wooley, K. L. *Adv. Mater.* **2013**, *25*, 5609-5614.

(145) Wang, Y.-C.; Tang, L.-Y.; Li, Y.; Wang, J. *Biomacromolecules* **2008**, *10*, 66-73.

(146) Wang, Y.-C.; Tang, L.-Y.; Sun, T.-M.; Li, C.-H.; Xiong, M.-H.; Wang, J. *Biomacromolecules* **2007**, *9*, 388-395.

(147) Du, J.-Z.; Chen, D.-P.; Wang, Y.-C.; Xiao, C.-S.; Lu, Y.-J.; Wang, J.; Zhang, G.-Z. *Biomacromolecules* **2006**, *7*, 1898-1903.